INVESTIGATION AND DESIGN OF DIFFERENT ANTENNAS IN SOLAR CELLS' ENVIRONMENTS WITH THEIR NEEDED TOOLS

Mohamed A. Moharram Hassan

A thesis
in
The Department
of
Electrical and Computer Engineering

Presented in Partial Fulfillment of the Requirements
For the Degree of Doctor of Philosophy
Concordia University
Montréal, Québec, Canada

September 2015

Concordia University
School of Graduate Studies

This is to certify that the thesis prepared

By: **Mr. Mohamed A. Moharram Hassan**

Entitled: **Investigation and Design of Different Antennas in Solar Cells' Environments with Their Needed Tools**

and submitted in partial fulfillment of the requirements for the degree of

Doctor of Philosophy (Electrical and Computer Engineering)

complies with the regulations of this University and meets the accepted standards with respect to originality and quality.

Signed by the final examining commitee:

Dr. Lotfollah Shafai _____ External Examiner

Dr. Abdel Razik Sebak _____ Examiner

Dr. Robert Paknys _____ Examiner

Dr. Amr Yousef _____ Examiner

Dr. Ahmed A. Kishk _____ Supervisor

Approved _____
Chair of Department or Graduate Program Director

_____ September, 11, 2015 _____
Christopher Trueman, Ph.D., ing., Interim Dean
Faculty of Engineering and Computer Science

Abstract

Investigation and Design of Different Antennas in Solar Cells' Environments with Their Needed Tools

Mohamed A. Moharram Hassan, Ph.D.

Concordia University, 2015

With the spread use of solar cells as a renewable energy source and the wide use of wireless communications, it is interesting to use the solar cell panels as an energy source for rural wireless communications for security and safety. For compactness, it is proposed to embed antennas in the solar cell panels. Therefore, it is proposed to investigate the antenna characteristics within this environment. As such, the characteristics of the solar cells in the radio frequency region should be studied for proper design of the antennas in such an environment. Therefore, a rigorous design approach for antennas in the solar cells' environment is proposed through this work. A practical model of the solar cells in the microwave frequency range is presented using anisotropic surface impedance boundaries. Two different surface impedance measurement setups are exploited to accurately model solar cells. Moreover, measurements of antennas' radiation efficiency are invoked in this work using the Wheeler cap concept in a contactless fashion to perform measurements within solar cells' environments. A novel measurement technique has been proposed extending conventional Wheeler cap capabilities to measure wide band antennas. The technique promotes a straightforward processing procedure and convenient measurement setup.

In addition, a simple, fast, and efficient numerical solution for the electromagnetic scattering arbitrary problems is proposed. Based on the uniqueness theorem and

the use of novel equivalent problems with Random Auxiliary Sources (RAS), more degrees of freedom are added resulting in significantly faster solutions. The proposed technique is expected to provide a significant reduction in the execution time and memory requirements compared to the surface equivalent based Method of Moments (MoM) as the inherent properties of this procedure are used. Various verification and result cases are presented to assess the introduced technique, which is incorporated into different analysis and design problems in this work. Moreover, the RAS method is extended to model antennas in their radiating and scattering modes, which, in turns, is adopted in the reflectarray antenna analysis and design procedures.

The introduced solar cells models along with the developed computations and measurement tools are used to develop a design procedure for antennas suited for the solar cells environment. An optically transparent reflectarray antenna integrated with solar cells is proposed as an application of interest that suits satellite communication purposes. Material choice, feed antenna tailored design and rigorous design procedures are presented to enhance the achievable performance of the antenna/solar cells integrated device.

بحَمدِهِ تَعَالَى

To my lovely daughter, Sundus.

Acknowledgments

I would like to express my deep gratitude to my supervisor, Dr. Ahmed A. Kishk for his guidance, patience and invaluable comments.

Thanks are also due to Dr. Lotfollah Shafai, Dr. Robert Paknys, Dr. Abdel Razik Sebak and Dr. Amr Yousef for their priceless comments and serving in my examining committee.

I would also like to thank Concordia University technical staff, Mr. Jeffery Landry, Mr. Vincent Mooney-Chopin, Mr. Michael Rembacz, William Chicoine and Mr. Dominc Ng for their assistance to build and measure the presented prototypes in this work.

Lastly, I offer my love, regards and blessings to my mother, my father, my brother and my wife for their limitless support during the compilation of this work.

Contents

List of Figures

List of Tables

List of Acronyms

EM	Electromagnetic
PEC	Perfect Electric Conductor
PIFA	Planar Inverted F-Antenna
GPS	Global Positioning System
RF	Radio Frequency
DC	Direct Current
UHF	Ultera High Frequency
DRA	Dielectric Resonator Antenna
AUT	Antenna Under Test
RAS	Random Auxiliary Sources
FMM	Fast Multipole Method
MLFMM	Multilevel Fast Multipole Method
MoM	Method of Moments
I-MoM	MoM with an Iterative solver
MMP	Method of multiple Mulipoles
GMP	Generalized Multipole Method
MAS	Method of Auxiliary Sources
PO	Physical Optics approximation
MR	Multiple Reflections
2D	Two Dimensional
3D	Three Dimensional

p-n	p-type and n-type
EBG	Electromagnetic Band Gap
Q-factor	Quality factor
PMC	Perfect Magnetic Conductor
AMC	Artificial Magnetic Conductor
IWC	Improved Wheeler Cap
MWC	Modified Wheeler Cap
HFSS	High Frequency Structure Simulator
CLSM	Complex Least Square Method
PMCHW	Poggio, Miller, Chang, Harrington and Wu
IFB	Iterative Field Bouncing
FDFD	Finite Difference Frequency Domain
FEM	Finite Elements Method
IBC	Impedance Boundary Condition
PSO	Particle Swarm Optimization
SPW	Sampling per wavelength
RCS	Radar cross section

List of Symbols

ε_r	Relative permittivity of dielectric
σ	Electric conductivity
Z_s	Surface Impedance
S	Siemens
Ω	Ohm
D	Antenna Directivity
G	Antenna Gain
P_r	Radiated power
P_a	Accepted power by the antenna port
η_r	Antenna radiation efficiency
η_t	Antenna total efficiency
λ	Wavelength
η_0	Intrinsic impedance of free-space
η_{vv}	Normalized surface impedance in the v direction
Γ_m	Uncalibrated measured reflection coefficient
S	S-parameter
Γ_L	Load reflection coefficient
$\tan\delta$	Loss tangent
j	$\sqrt{-1}$
ω	Angular frequency
s	Complex frequency
f_0	Resonance frequency of the unloaded resonator
Q_0	Unloaded quality factor
Q_a	Quality factor of the antenna
Q_w	Quality factor of the antenna inside the Wheeler cap
Γ_a	Reflection coefficient of the antenna in free-space

λ_0	Free-space wavelength
ω_0	Resonance angular frequency
$\mathbf{E}$	Electric field vector
$\mathbf{H}$	Magnetic field vector
$\overleftrightarrow{\boldsymbol{\eta}}$	Anisotropic surface impedance dyad
$\hat{\mathbf{n}}$	Normal unit vector to surface S
$O()$	Big O number to indicate the order of complexity
α^i	Polarization angle of the incident wave measured from the plane of incidence
θ^i	Elevation angle of the incident wave
φ^i	Azimuthal angle of the incident wave
N_I	Number of iterations
$N_{g,j}^{e(i)}$	Number of sources used in iteration j^{th} for the exterior (interior) equivalent problem(s).
M	Number of testing points
$a_{j,n}^{e(i),v}$	the unknown complex amplitude of the infinitesimal dipole n in the v polarization for the external (internal) problem
$\mathbf{E}^{I_v(M_v)}$	the electric field of a unit moment electric (magnetic) dipole in the v polarization
$\mathbf{H}^{I_v(M_v)}$	the magnetic field of a unit moment electric (magnetic) dipole in the v polarization
$\mathbf{r'}_n$	the nth random source position vector
ξ^q	Pre-specified error tolerance in the bouncing fields update in the IFB iteration q
ζ	Memeory efficiency ratio for the RAS method
$\mathcal{L}_{(\substack{\mathcal{E} \\ \mathcal{H}})}$	linear operators to evaluate the electric and magnetic fields due to infinitesimal sources
η_{ap}	Aperture efficiency
η_t	Field taper efficiency
η_s	Spillover efficiency
η_p	Polarization efficiency
F	Distance from the feed antenna phase center to the reflectarray aperture

Chapter 1

Introduction

Dual function devices are always a desired solution for different applications with limited resources. This concept has been employed in the area of electromagnetics for different applications. These applications include reducing the occupied area by the antenna and the other device(s) [1,2], adding more desired properties for the existing application [3, 4], or even making antennas more ergonomic and better accepted by the public [5,6]. The integration between antennas and solar cells has been a preferred choice for many research groups for mainly reducing the occupied area for different space and civilian applications [7–12]. Yet, careful and rigorous analysis is always desirable for designing antennas within the energy harvesting environment to maintain the desired overall system performance of the dual functional device.

Such an integration between devices with completely distinct operating principles and frequencies leads to the possibility of having both devices designed separately. On one hand, the antenna design procedure should involve the effect of the solar cell environment on adjacent electromagnetic (EM) waves. So, accurate modeling of the solar cell in the microwave wave frequency range (300 MHz - 300 GHz) is essential for better prediction for the antenna performance. On the other hand, solar cells require the largest possible exposure to sunlight for better performance. So, the used

antennas should maintain a minimal effect on the sun exposure of solar cells for better energy harvesting capability.

1.1 Solar Cells Structure and Potential Integration Possibilities

The solar cells are simply transducers that transform light energy into electric energy. The development of such a device has gone through different stages from 1838 till now [13]. Recently, research has been carried out to improve the efficiency and durability of products for future renewable energy generating devices [13]. Different generations of solar cells have been developed through history featuring different efficiency ranges and mechanical properties that suit different applications. Figs. 1.1 and 1.2 show two different solar cells types that are available commercially. The reported performance values of the solar cells are tabulated in Table 1.1 as presented in [14]. The efficiency term here represents the useful electrical energy generated by a solar cell (electrons) in comparison with the optical energy that excites it (photons) [13]. In general, solar cells mainly consist of p-n junction covered with conducting electrodes from both sides to collect the generated electrons as shown in Fig. 1.3 and illustrated in [13]. Trapped incident light in the solar cell structure recombines electron/hole pairs that move each to a different electrode terminal producing electric energy [13]. At least one side of the solar cell has a meshed electrode to allow light to penetrate to the junction. Also, an anti-reflective material is there to help trap light in the cell through their small refractive index and pyramidal shapes as shown in Fig. 1.3.

The integration of the solar cells technology with different applications is a trending interdisciplinary research that involves electrical, mechanical, chemical, and building engineering together for future application [15]. The smart net-zero energy building is currently a potential research topic in building engineering that integrates solar

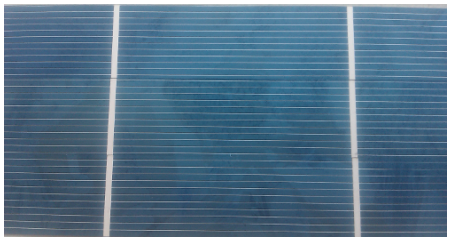

Figure 1.1: A single junction crystalline solar cell.

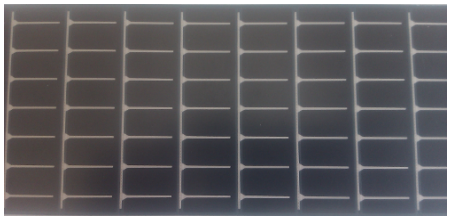

Figure 1.2: A single junction thin-film solar cell.

Table 1.1: The best reported efficiency of different solar cell types through literature [13].

Solar Cells Type	Efficiency (%)	Mechanical Consideration
Crystalline: Single Junction	21.8 - 24.7	Fragile
Crystalline: Multijunction	31	Fragile
Thin-Film: Single Junction	16.5 - 18.9	Flexible or Rigid
Thin-Film: Multijunction	13.5	Flexible or Rigid
Photoelectrochemical	11	Flexible or Rigid - Semi-Transparent

cells on the outside surface of buildings in cold areas [15]. Thus, that potential spread of solar cell environments orients research in antennas and microwave applications towards integration with the solar cells' environment.

1.2 Motivation

The expanding use of the solar cell technology in many applications ranging from space satellites to autonomous systems is growing every day. Typically, the high demand for electricity is a direct reflection of prosperity of a society. Thus, solar cells developers have the vision to incorporate their technology in different aspects in people's lives, including houses, vehicles, roads, or even smart phones for further cheap and environmentally safe electricity generation. Alternatively, the current trend for antenna designing is miniaturization for commercial and high performance products to save area for other important components regardless of all limitations in the antenna performance [16]. This trend limits the capabilities of an antenna engineer to use

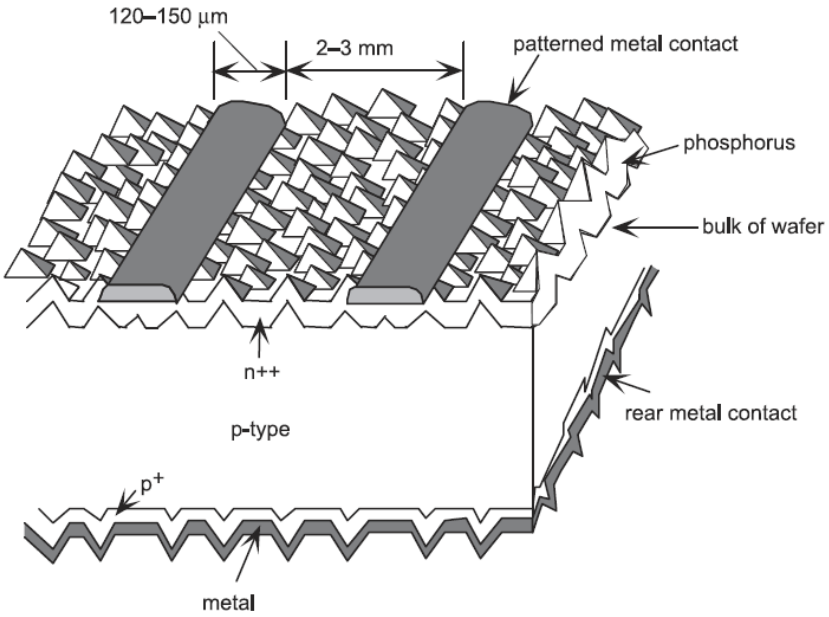

Figure 1.3: The micro-structure of a single junction crystalline solar cells as presented in [13].

design techniques that require large footprints. Therefore, attaching the antenna part, in any device that uses solar cells, with the large solar cells part adequately shifts the current design trend to another level with other design capabilities.

In addition, rigorous designs of antennas within the solar cell environment always involve challenging procedures; especially where high performance is expected from both the antenna and solar cells. The lack of accurate and realistic modeling of arbitrary solar cells in the microwave region is yet a missing key point for designing antennas in the solar cells' vicinity. The challenge in developing such a model is the process dependent materials and the use of different rough anti-reflective substances on top of the solar cell. These manufacturing recipes are not usually provided from manufacturers, so having an adaptive model or an accurate modeling scheme is of great use in the specified application. Alternatively, the performance consideration of the solar cells through the antenna design procedure is of major concern regarding the overall efficiency of the system. This reflects on the choice of materials and structures of the antennas not to block the solar cells from the sun.

Finally, the idea of using optically transparent material in designing the antenna/solar cells dual functional device is of great research potential. The reported difference in the dielectric properties of some of these materials, such as the Borosilicate Ceramic Glass (or Pyrex material) [5], with low dielectric constant in the optical range ($\sim$ 2.25) and high value in the microwave range (up to 8), is an interesting feature to exploit for such integration between solar cells and antennas. Therefore, various potential antenna designs with solar cells can be exploited using these materials.

1.3 Objectives

The focus in this thesis is based on three main aspects that help to adequately characterize and design antennas within the solar cell environment. These aspects are:

1. Having an accurate modeling scheme to the solar cell environment and studying its effect on the antenna performance.

2. Due to the unavailability of some needed tools, we have to design these necessary tools to reach our final goal. These tools help in the characterization and analysis of antennas in such environments, such as measurement devices and numerical tools.

3. Prototyping antennas to operate in the vicinity of solar cells for communication purposes incorporated the developed model.

Providing an accurate model for the solar cell environment is, of course, dependent on the solar cell type and the way materials are organized inside it. This work aims to provide a homogenized anisotropic surface impedance model to accommodate the complexity of all the different material layers, rough surfaces, and electrodes into consideration. Different uni-directional surface impedance measurement setups are

to be used for different frequency bands. Accordingly, the inverse problem will be performed to estimate the effective material properties of the employed solar cells.

In addition, characterizing the antenna radiation efficiency in the solar cells environment is a key factor that will be addressed through this work. This approach relies on the simple Wheeler cap concept. A non-invasive measurement setup will be presented to provide the required measurements by the Wheeler cap within the solar cells' environment via a means of contactless EM shielding structures. Furthermore, a fast, simple and efficient numerical tool will be necessary to analyze problems investigated in this work to speed up computations. This method will be able to accommodate problems with arbitrary anisotropic surface impedance boundaries as proposed through this work. Moreover, extending the proposed method to aid in the design of complicated antennas will be a significant advantage of the proposed method over the current commercial software packages.

The developed solar cells model in RF will be incorporated into the design process of antennas, leading to more prediction of antenna performance through the full-wave analysis. Consequently, an optically transparent reflectarray antenna will be designed with the required feed antenna as a potential integration mechanism between antennas and solar cells. A minimal effect over the solar cells energy harvesting capabilities will be highly considered through the design procedure to enhance the overall system performance. The design is projected to be a preferred solution for rural satellite ground stations. It is also possible to use this concept for satellites assuming the weight problem can be resolved. Such concept can also be applied to buildings and base stations.

1.4 Outline of the Thesis

This thesis is organized in seven chapters and additional four appendices. Chapter 2 discusses the published work about integrating antennas with solar cells focusing on the employed modeling techniques and antenna/solar cells integration trends. Then, the proposed experimental models for the solar cells effect over the RF is presented in Chapter 3. In addition, the antenna radiation efficiency measurement procedure and setups are presented in Chapter 4 targeting antennas mounted over large ground planes or solar cells. Details and verification results about the proposed Wheeler cap processing procedure is presented in Appendix A. Moreover, the proposed fast and efficient 3D EM scattering computation procedure is introduced in Chapter 5 based on the Random Auxiliary Sources (RAS) method. The presented RAS method is further extended to model antennas in their radiating and scattering modes with application to reflectarray antenna analysis in the same chapter. Other 3D EM scattering results and studies are presented in Appendix B. Nevertheless, the design and results of an optically transparent reflectarray antenna are presented in Chapter 6 incorporating the developed solar cells model with some detailed analysis presented in Appendix D. Chapter 6 also includes the developed synthesis and design feed antenna for the presented reflectarray with other feed antenna designs using the same concept presented in Appendix C. Finally, Chapter 7 presents the thesis conclusions, list of major contributions and expected future work.

Chapter 2

Literature Review

In this chapter, a review of different antenna designs integrated with solar cells for dual functional systems as antennas and energy harvesting in the same time is presented. Different configurations have been proposed through literature for arranging solar cells and antennas in a way not to disrupt the performance of either one. Some attempts were presented to have the solar cells as part of the radiating elements [12, 17]. Alternatively, solar cells have been used as a ground plane for antennas as in [5, 10]. This chapter discusses the published work in these two categories following the employed modeling schemes.

2.1 Solar Cells Modeling

An important phase of designing antennas in the vicinity of solar cells is to accurately consider the solar cells effect within the antenna operating frequency band in the design process. Different modeling techniques have been used to include the effect of solar cells into the design procedure of integrated solar cells/antenna devices. These methods are:

1. Far-field scattering measurements [18].

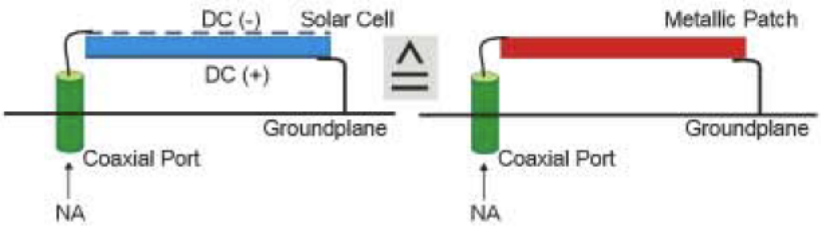

Figure 2.1: Measuring the input impedance of a shortened patch antenna to model the solar effect in the microwave range as in [9] ©2004 IEEE.

2. Comparison between the input impedance of a solar cell shortened patch and a similar sized metallic patch [9].

3. Exact structure modeling of the solar cell with the exact material parameters [10, 19, 20].

4. Rectangle waveguide setup [21].

A series of scattering measurements from large solar cells panels are compared to the same sized conductive mock-ups to evaluate the differences have been presented in [18]. The presented results showed that solar cells can be treated as PEC sheets as a 'first order approximation' for the S and Ku bands. However, the presented conclusive result of this method did not hold for applications with near-field interaction with solar cells as presented in [17, 22, 23], which are reported at lower frequency bands. Extrapolating these results yields to more interaction with antennas at high frequency bands resulting in much discrepancy between simulations and measurements.

Measuring the input impedance of a solar cell shortened patch antenna provides a similar result to a conducting patch with a similar size only at the low frequency band (below 2.5 GHz) [9]. The reported measurements show discrepancies between the two measurements at higher frequency bands. This is quite expected at low frequencies because in a patch antenna, radiation happens from edges [24], which are part of the solid metal electrodes of the solar cell as seen in Fig. 2.1.

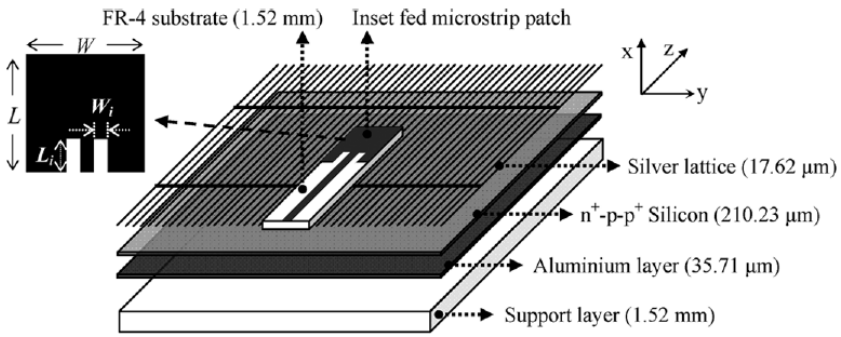

Figure 2.2: Exact structure modeling of the solar cell with the exact material parameters with a top mounted patch antenna as in [10] ©2009 IEEE.

The exact structure modeling of the solar cells uses a similar structure to Fig. 1.3 to model the different layers of a crystalline solar cell as shown in Fig. 2.2. The silicon material that forms the p-n junction has bulk permittivity $\varepsilon_r = 15.3$, dark conductivity $\sigma = 310$ S/m, and light exposed conductivity $\sigma = 254,383$ S/m measured at DC as presented in [25]. These model parameters have been used for various applications for the frequency band below 4 GHz [10]. It is important to illustrate that this model neglected the effect of anti-reflective material used in the solar cell structure, which may have a significant effect at high frequency bands as well as the silicon parameters. The reported measurement results using this model at the specified frequency band show very good agreement with the simulated results [26,27].

Recently, solar cells specific material modeling has been presented in [19, 20]. It is important to notice that these works have been developed in collaboration with members from the physics department. The provided models are only valid for the employed in-house manufactured solar cells, which may differ if commercial solar cells are required to be used. Typically, this detailed solar cell structure information is not necessary provided by the solar cells provider as it is, to some extent, confidential regarding the recipe of the product. Therefore, a more generic approach to model solar cells in the microwave range is indeed required to accurately design antennas in the vicinity of solar cells.

Furthermore, an x-band waveguide setup has been used to characterize the solar cells' behavior as an impedance surface [21]. The reported value of the used solar cell surface impedance is $Z_s = 0.1 + j1\,\Omega$/square, which is very close to PEC. However, the reported values of the solar cells effect has not been yet verified within an antenna prototype to fully trust the results. Also, it contradicts the reported findings of the previous method [26], where solar cells have been claimed to behave differently with the wave polarization (anisotropically).

2.2 Solar Cells as Part of the Radiating Element

The trend of using solar cells as the radiating elements besides energy harvesting is promoted by the work in [7, 28]. Different patch antennas configurations have been proposed for numerous applications, such as conventional patches [7, 9, 17, 22, 27–29], wide band stacked patches [30], and tri-band antenna [31]. An array configuration of patch antennas has been proposed in [32] for GPS applications with omni-directional right hand circularly polarized radiation. Also, planner Inverted F-Antenna (*PIFA*) are integrated with solar cells as introduced in [12, 33]. In most cases, the measured results match dummy PEC models for the low frequency bands as illustrated in Sec. 2.1. Upper band measured results do not match simulations as expected from the model limitations mentioned in Sec. 2.1. Moreover, the decoupling between the antenna RF signal and the solar cell DC signal is an issue that has to be treated similarly to [22]. Furthermore, the main challenge with this design trend is the need for a laser cutting tool or some delegate 'diamond tipped' tools to shape the solar cells into the desired patch antenna structures. Also, one may expect that this technique is not efficient for high frequency applications, where it requires smaller radiating elements. The mechanical and electrical effort required to shape and make use of small radiating elements shall not produce large amounts of electric energy that is

required to power up devices.

Recently, a conformal UHF antenna design was integrated with solar cells for flapping-wing robots in [20]. The design used the entire solar cells interconnects as part of the antenna, where the solar cells' conducting lattice carry both DC and RF signals. Therefore, the RF and DC were decoupled using RF choke. The performance of the antenna/solar cells showed minimal deterioration due to the integration as the solar cell model was accurately incorporated into the design process of the antenna. It is important to mention that the presented work was conducted in collaboration with members from the physics department, who indeed helped to characterize the employed solar cells and fabricate the prototype.

2.3 Solar Cells as a Ground Plane for Antennas

Another use of solar cells with antennas places the antenna over the solar cell. This integration concept detaches the required antenna performance from the required harvested energy from solar cells. The challenges in this integration trend are the excitation method as well as the low shadowing antenna designs that do not disrupt much of the solar cells function. The following presents some proposed solutions for this integration trend.

2.3.1 Single Element Solar Cells Antennas

The concept of using the solar cells as a ground plane for antennas allowed for different configurations of antennas with solar cells. Slot antennas made use of this technique by placing the feeding microstrip circuit underneath the solar cells and using slots within the solar cells as [34–38] for different applications. The measured results show very good agreement with their corresponding simulations because the radiating elements are mainly the slots with minimal interaction with the solar cell. However,

the slot cutting procedure still requires delicate machining, which adds a mechanical overhead for fabrication. Also, these cutaway parts of the solar cell reduce the amount of harvested energy of solar cells.

Another integration mechanism uses patch antennas with solar cells as their ground plane [10,27,39–43]. Using exact structure modeling for the solar cell, the simulated and measured performance of patch antennas over solar cells show anisotropic behavior with the orientation of the patch with respect to the solar cells metallic lattice [26]. In addition, the measured antenna gain and radiation efficiency of the patch antennas are slightly less than their corresponding metallic mock-ups because of the high interaction between the antenna RF and the lossy solar cell. Using the same concept, a PIFA antenna has been introduced in [44] with a top fed microstip line. The main concern with this design approach is the blockage resulting from both antenna elements and feeding lines, which significantly deteriorates the energy harvesting capability of the solar cell besides wasting some amount of the RF energy in the lossy solar cell structure. A solution to the latter problem was proposed in [45] by using transparent conductors over a glass substrate. The presented design exploited a taper slot line antenna design that was meant for ultra wide band applications with a quasi-omnidirectional radiation pattern, which may be required in some applications.

An interesting approach for integrating antennas with solar cells is the use of a high dielectric constant transparent material, such as Borosilicate glass (Pyrex), to have a dielectric resonator antenna (DRA) [5]. The used material is the high heat resistant glass ceramic material with a reported dielectric constant around 7 in [5] with a very low loss tangent. The main benefit of this material is the difference of its dielectric constant from the microwave frequency range (up to 8) to the optical frequency range (~ 2.25), which is more suitable for the application. In the work presented in [5], the proposed simple DRAs are used as light lenses for solar cells to harvest more energy, which adds to the use of the material with solar cells. However,

the presented work used a probe station to measure the performance of the antenna, so incorporating the proposed idea in an array environment is yet a challenge to investigate. Also, a major advantage of the idea of using DRA with solar cells is the concentration of the energy within the DRA body, which results in less influence by the lossy ground planes of the solar cells [46]. This is the reason that made the measured performance of the transparent DRAs is similar to the simulated results in [5].

2.3.2 Solar Cells Antenna Arrays

The flexibility of the presented integration technique of using solar cells as ground planes for antennas allowed for creating antenna arrays. An intuitive solution was to have the feeding network on the back side of the solar cells. Circularly polarized linear slot antenna array was presented in [8] making use of this technique. Again, the main challenge in this design is the mechanical overhead to create the required slots.

Recently, a low shadowing antenna array design was presented in [47] exploiting the solar cells' conducting lattice as spots to mount antennas as shown in Fig. 2.3. The presented experimental results show minor shadowing effects on the solar cells. The shadowing percentage increased as the angle of incidence of the light source θ, as shown in Fig. 2.3, is increased. This design approach provided an adequate integration method between antennas and solar cells avoiding significant shadowing over the solar cells performance. However, the antenna spacing is limited by the presence of the solar cells conducting lattice, which may not be favorable for high frequency application as grating lobes may be visible [48].

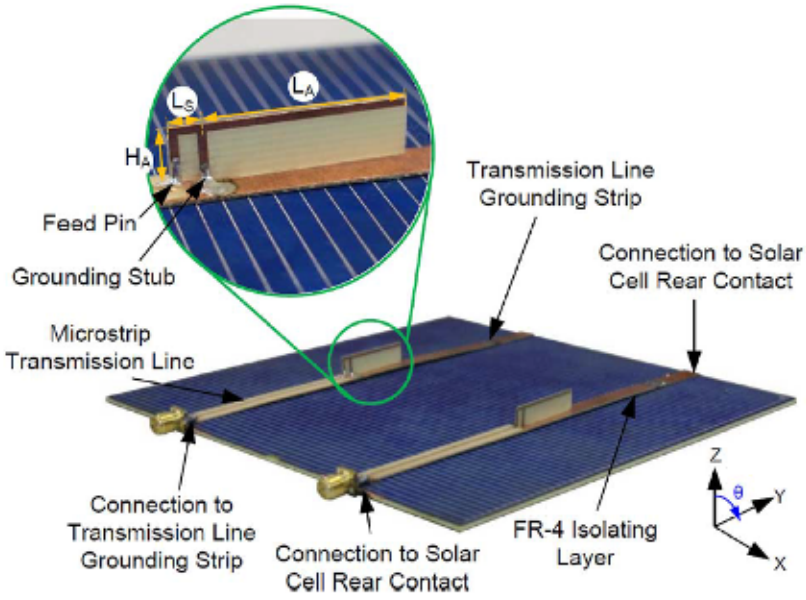

Figure 2.3: A low shadowing dual PIFA antenna array design in [47] ©2015 IEEE.

2.3.3 Reflectarray Solar Cell

One solution to the excitation problem mentioned before and faced with antenna arrays in general is the use of the reflectarray concept. Reflectarrays are the flat version of the parabolic reflector antennas proposed in [49, 50]. The use of reflectarray with solar cells was first proposed in [23, 51] using thin metallic dipoles and crossed dipoles over glass for the unit cells. Since the properties of the ground plane solar cells were not exactly known for sure by that time, designs at adjacent frequencies were fabricated to account for the neglected solar cells effect in the design process [51]. The main concern with this design is the blockage resulting from the dense metallic dipoles that may cause reduction in the solar cell efficiency. Recently, another resemblance for the crossed dipoles reflectarray has been introduced in [19, 52]. Modeling the solar cells as conductive sheets, adequate analysis of reflectarray unit cells has been performed. However, the design deteriorated the performance of solar cells by 17.5%, which opens the door to other designs that provide less blockage of solar energy.

A fully transparent design approach is presented in [21, 53] using a transparent

conductive thin-film [54] patches deposited on a glass substrate as a unit cell. The presented work introduced only the unit cell design without implementing the full reflectarray. So, the overall efficiency of the solar cell and the reflectarray are still questionable.

Chapter 3

Solar Cells Material Modeling

3.1 Introduction

The different types of solar cells are traditionally expected to behave similarly to PEC in the microwave range due to the presence of the metallic electrodes on both sides of the electric DC power connection as seen through literature. However, the exposed side to the sun has a lattice of metal to allow light to reach the p-n junction. This is mainly the reason behind the slight deviation from the PEC behavior. So, a reasonable model for these substances is anisotropic surface impedance due to the asymmetric distribution of the electrode lattice on top of solar cells. Another reason to use a surface impedance model is the possibility to have a thin glass or a plastic protection cover over solar cells for reinforcement or even protection, which an antenna engineer may not be aware of as a given information from the manufacturer. So, a surface impedance model can best suit the objective in this case. Here, two methods are suggested to measure the solar cells surface impedance. The first technique is to use a scattering type measurement similar to [18], but in the Ku-band. Second, a novel method is proposed to measure the anisotropic surface impedance of solar cells in the C and X bands using contactless waveguide flanges. These measurements

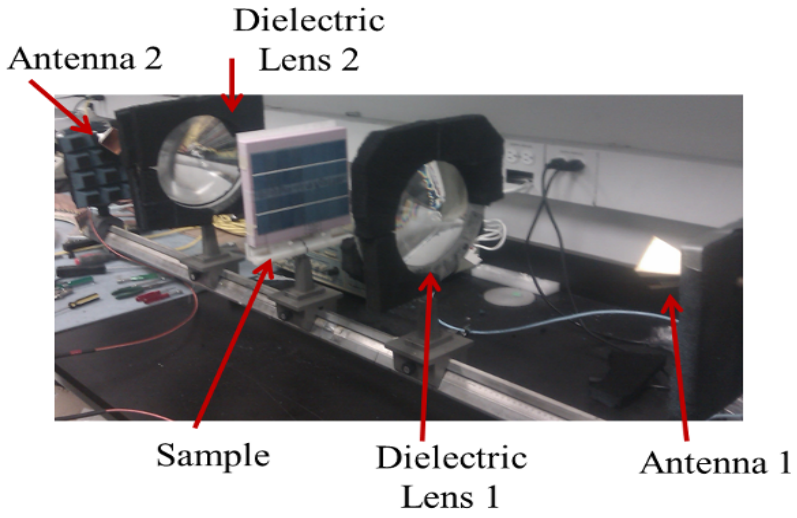

Figure 3.1: The used scattering measurement setup.

are further exploited in an inverse problem to estimate the material properties of a crystalline solar cell, which is more suitable to be used in commercial EM simulators.

3.2 Scattering Measurement Setup

The scattering setup uses the approach presented in [55]. Fig. 3.1 shows the used setup with a solar cell sample. In order to trust the results coming from the setup, confidence checks are made to assess the accuracy of the measurement as presented in the following.

3.2.1 Confidence Checks

A confidence check for the used setup is made using two known parameters dielectric slabs backed by a conductor. The inverse nonlinear problem has been carried out directly to obtain the dielectric constants of the materials. The first slab has a thickness of 1.45 mm and $\varepsilon_r = 2.94$. Also, the second slab has a thickness of 3.1 mm and $\varepsilon_r = 10.8$. Dielectric constant plots are shown in Fig. 3.2 for both cases. The measured results are quite close to the known values. It is important to observe the high

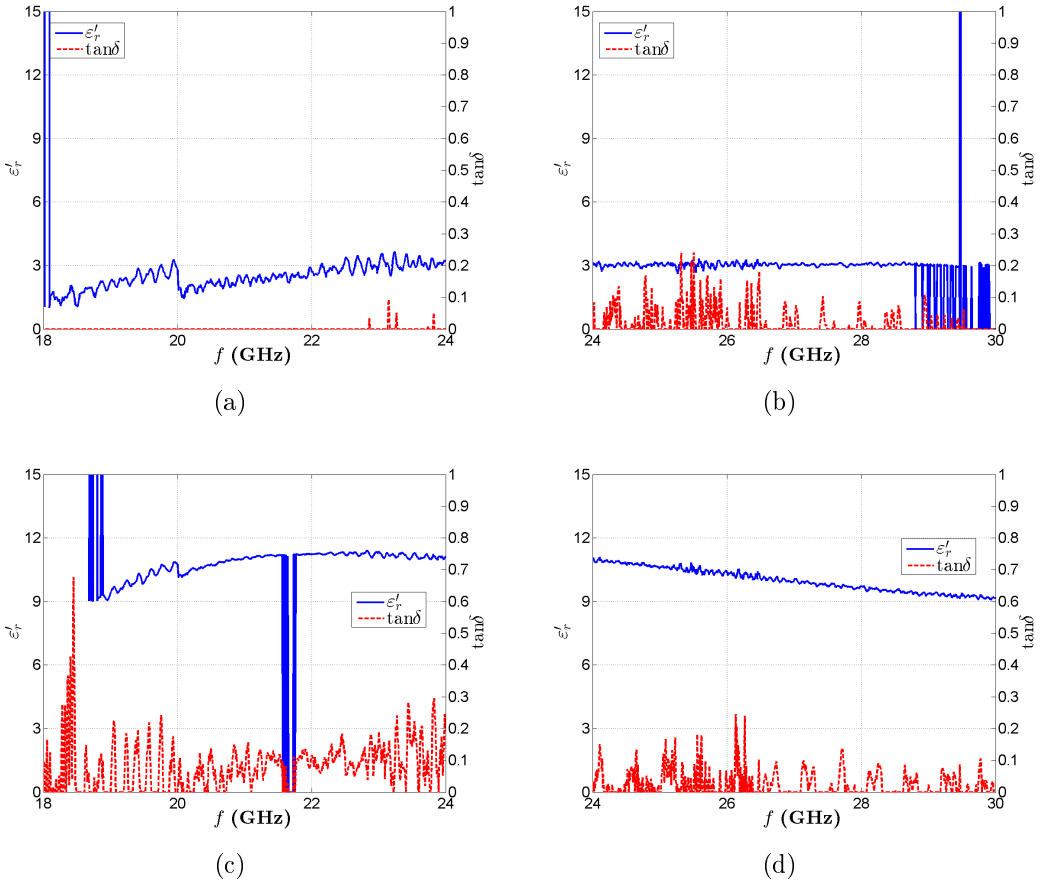

Figure 3.2: Confidence checks for the scattering setup with two different materials. (a) and (b) are for the $\varepsilon_r = 2.94$ material. (c) and (d) are for the $\varepsilon_r = 10.8$ material.

susceptibility of the measured results to noise. This noise is one of the reasons the results are not accurate. Also, the position and orientation adjustment of the samples in the setup is prone to human error due to lack of orientations precision scales (tolerance is ± 1 mm). It is also noticed that both cases have problems with measurements below 20 GHz, measurements should be considered for frequencies above 20 GHz. Furthermore, the measurements using this technique fail where ambiguity in the results happens. In these cases, ambiguity happens where the dielectric thickness is around multiples of $\lambda/2$ inside the dielectric.

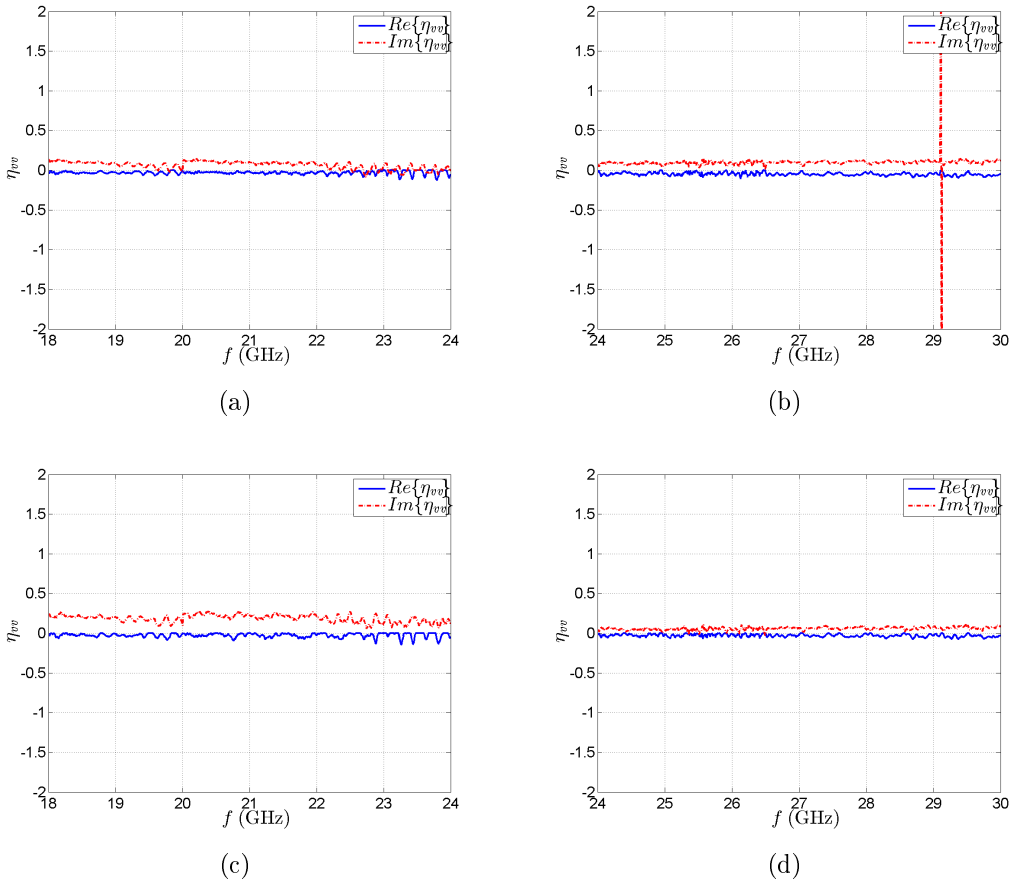

Figure 3.3: Measured anisotropic surface impedance of crystalline solar cells using the scattering measurement setup. (a) and (b) are with electric field perpendicular to the conducting lattice. (c) and (d) are with electric field parallel to the conducting lattice.

3.2.2 Solar Cells Anisotropic Surface Impedance Measurements

The measured normalized surface impedance, which is defined in [56] as

$$\eta_{vv} = Z_s/\eta_0 \tag{3.1}$$

where η_0 is the intrinsic impedance of free-space, Z_s is the un-normalized surface impedance value, and η_{vv} is the normalized surface impedance value in the direction of v. The measured results for the crystalline solar cells in both directions are shown in Fig. 3.3. Also, the measured results for the thin film solar cells in both directions

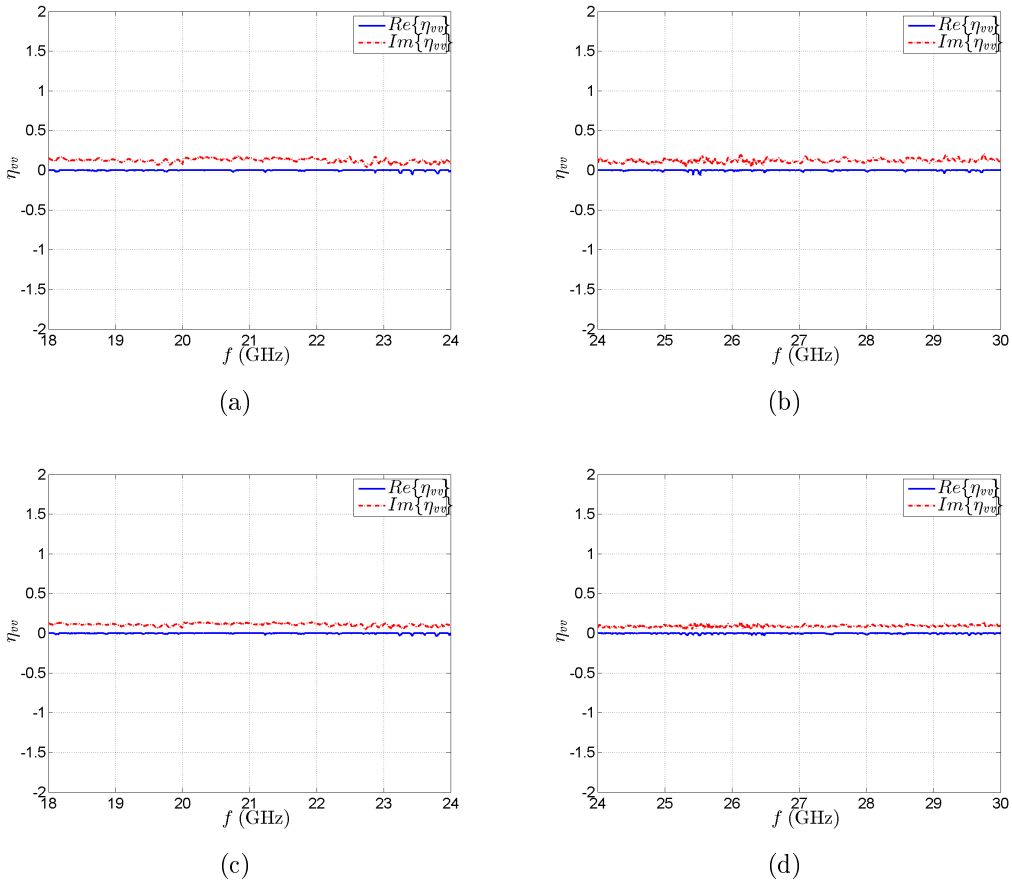

Figure 3.4: Measured anisotropic surface impedance of thin-film solar cells using the scattering measurement setup. (a) and (b) are with electric field perpendicular to the conducting lattice. (c) and (d) are with electric field parallel to the conducting lattice.

are shown in Fig. 3.4. The results illustrate that having the electric field parallel to the conducting lattice results in slightly smaller imaginary part of the surface impedance, which means it is closer to the PEC case. As explained in the confidence check subsections, the results are prone to human error and noise, which can make it quite inaccurate. Therefore, another measurement method should be used to be prove more accurate results.

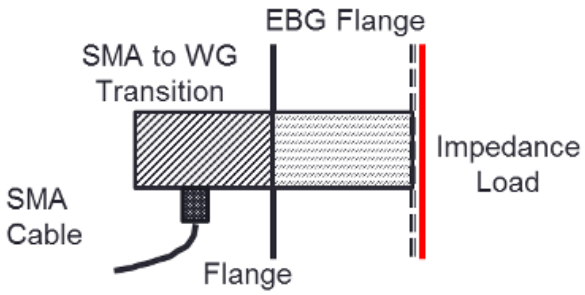

Figure 3.5: An illustration to the proposed surface impedance measurement setup.

3.3 Contactless Waveguide Measurements

A contactless waveguide measurement setup is proposed to measure the effect of solar cells as a homogenized surface impedance as illustrated in Fig. 3.5. Conceptually, leakage between the waveguide flange and the impedance surface load, which should be close to PEC is prevented through using an evanescent wave structure. Ideally, electromagnetic waves are not allowed to propagate between PEC and Perfect Magnetic Conductor (PMC) surfaces when the separation gap between them is less than $\lambda_0/4$. Thus, realizing this PMC surface is possible through the artificial magnetic conductor (AMC) concept, where the Electromagnetic Band Gap (EBG) structures can be used for such purpose. Moreover, further details and results about the contactless EM shielding are discussed in Chapter 4.

Consequently, three calibration measurements are required to have the reference plane exactly over the measured sample, namely: short circuit, offset short circuit and matched load as used in [55]. The fabricated prototype of the contactless setup and the employed equipments are shown in Fig. 3.6. Moreover, the designed EBG flange is chosen to be of mushroom-shaped type [57] with band gap exactly fitting the X-band range. The structure details of the employed mushroom-like EBG unit cell is presented in Fig. 3.7 (a) with a band stop that covers the entire X band as shown in the dispersion diagram in Fig. 3.7 (b) following the guidelines in [58].

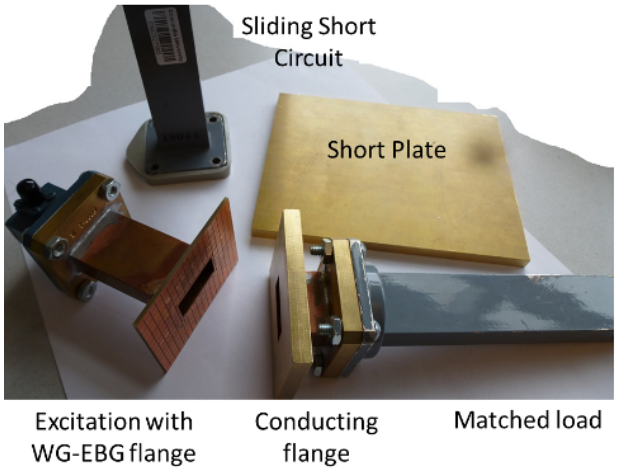

Figure 3.6: The employed X-band contactless surface impedance measurement setup.

3.3.1 Measurement Results and Inverse Problem

Full-wave simulation results of the contactless setup over a conducting copper plate with an air gap of 0.1mm shows that electric field exists over the waveguide perimeter that is surrounded by EBG unit cells as shown in Fig. 3.8. However, this electric field is terminated over the EBG surface, which can be approximated as a termination in the computational domain in a truncated inverse problem approach to determine the solar cells material parameters. This simplified inverse problem full-wave model is shown in Fig. 3.9 (a) terminating the air gap between the sample under test and the waveguide wall perimeter right at the outside dimensions of the standard waveguide. This homogenized anisotropic surface impedance model is used to identify the unknown parameters of the solar cells illustrated in Fig. 3.9 (b). By measuring the thickness of the solar cell (0.24mm), individual thickness parameters (t_1, t_2, t_3 and t_4) can be determined within the overall constraint. Also, the material types can be determined by the permutations provided for the commercial solar cells in [13]. Several manual iterations are performed to obtain similar surface impedance to the measured cases as shown in Fig. 3.10. The process started with the case of perpendicular electric field to the conducting lattice and then a confidence check is conducted

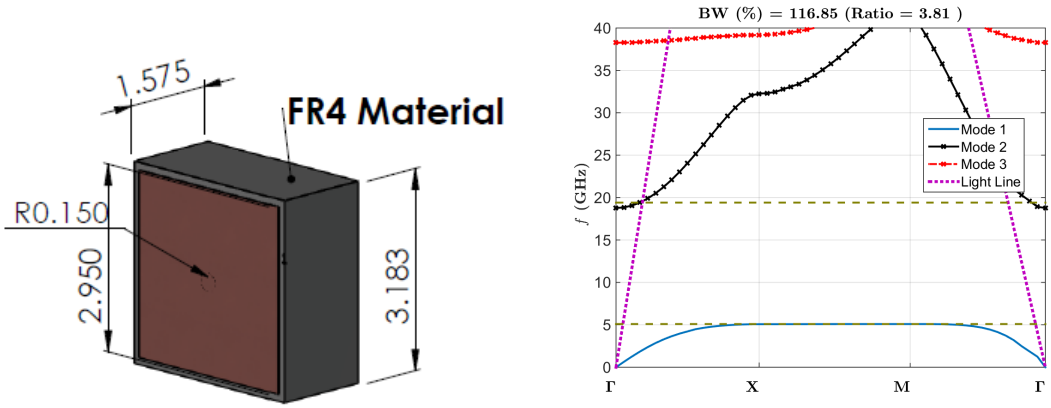

(a) (b)

Figure 3.7: The employed EBG unit cell structure and dispersion diagram. (a) EBG unit cell layout and dimensions in millimeter. (b) The associated dispersion diagram of the infinitely periodic unit cell in (a).

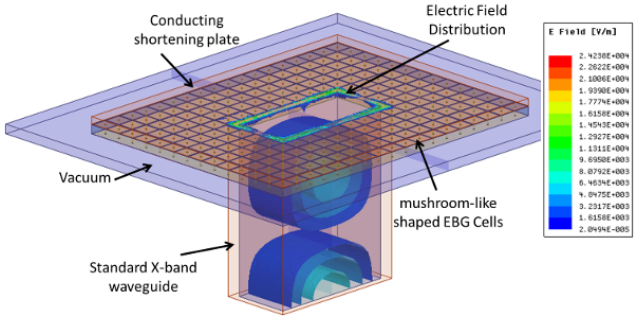

Figure 3.8: The electric field distribution of the contactless setup terminated by a copper shorting plate separated by a 0.1mm air gap from the EBG surface.

with the other polarization following the guideline of commonly used materials in the crystalline solar cells industry [13]. The employed semiconductor p-n junction [13] is found to be doped silicon material with relative permittivity (ε_r) of 12.9 and bulk conductivity (σ) of 850 S/m. Also, the antireflective material is found to be silicon dioxide with ε_r of 3.9 and loss tangent ($\tan\delta$) of 0.015 with details shown in Fig. 3.11. This material model can be used in the full-wave analysis to predict the overall reflectarray performance including the effect of solar cells.

It is important to know that the effect of changing the air gap in the simplified setup affects the slope of the curves shown in Fig. 3.10. Thus, the air gap (ranged from

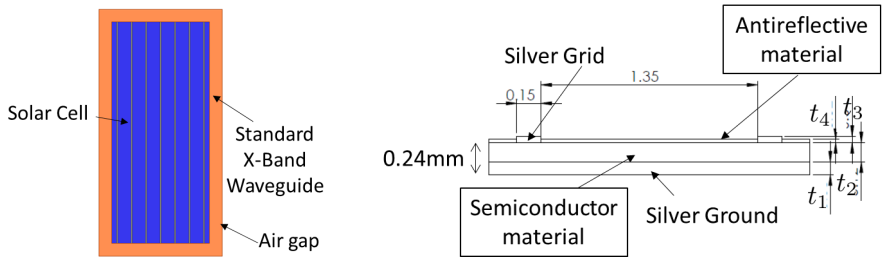

(a) (b)

Figure 3.9: The truncated inverse problem full-wave model and unknown parameters. (a) The simplified full-wave analysis model. (b) The unknown solar cells parameters.

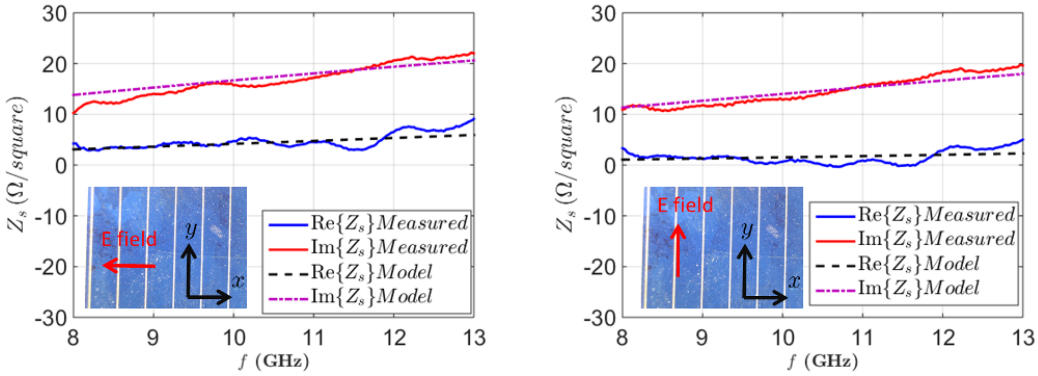

(a) (b)

Figure 3.10: The measured and modeled anisotropic surface impedance at the X band of the employed solar cell using the contactless setup shown in Fig. 3.6: (a) is with electric field perpendicular to the conducting lattice and (b) is with electric field parallel to the conducting lattice.

0.05mm to 0.3mm) is also a parameter to be considered through the inverse problem that may vary between different measurements. Moreover, another confidence check is performed using a similar measurement setup in the C-band. The results are shown in Fig. 3.12 confirms the validity of the obtained solar cells model beyond the X-band. However, the measurement results near 4 GHz exhibits unexpected behavior due to leakage from the setup (i.e. fields are not terminated correctly at the outer waveguide perimeter). Furthermore, the provided model asymptotically lines up with models that has been developed for designs at lower frequency bands [9], where a PEC model for solar cells is incorporated (i.e. $Z_s = 0$ Ω/square) as seen through the surface

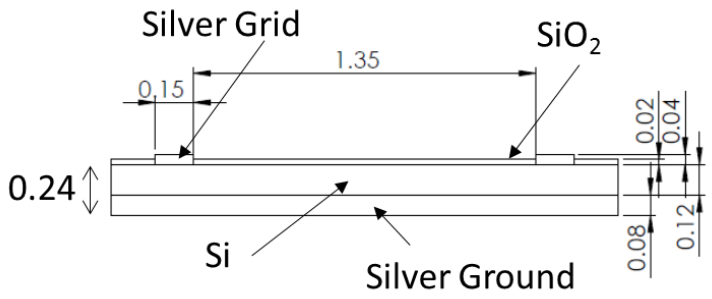

Figure 3.11: The structure cross section with material information (all dimensions are in millimeter).

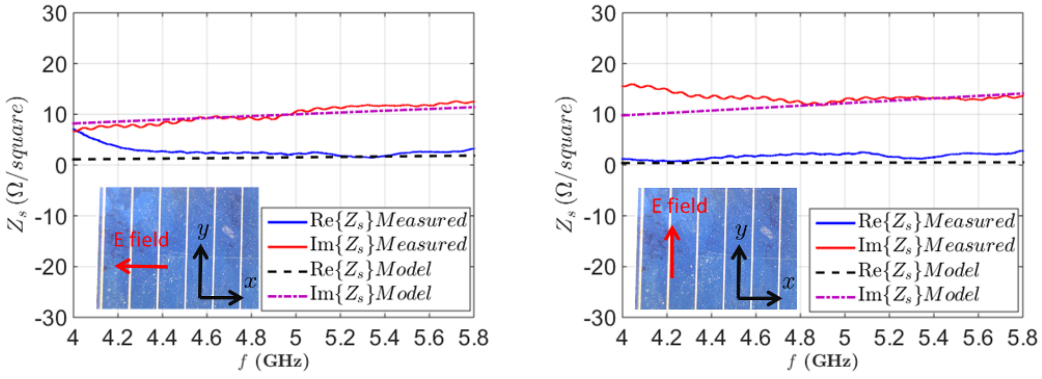

(a) (b)

Figure 3.12: A verification measurements for the modeled anisotropic surface impedance at the C band compared to measurements: (a) is with electric field perpendicular to the conducting lattice and (b) is with electric field parallel to the conducting lattice.

impedance trend with frequency.

3.4 Summary

According to the observed geometry of the solar cells, an anisotropic behavior of solar cells over RF was expected due to the anisotropic distribution of the conducting lattice on the top side. Hence, a homogenized anisotropic surface impedance boundary was proposed to include the effect of solar cells in the RF. Consequently, two methods were proposed to characterize the effect of solar cells in RF based on

measuring reflections. The first method exploited a plane wave reflection setup that was able to distinguish the anisotropy in the surface impedance boundary according to the solar cell orientation. However, the accuracy of this setup was questionable at this frequency range. Thus, the second measurement setup used a contactless waveguide flange setup that was calibrated to have the reference plane at the sample boundary. The anisotropic surface impedance in the X and C bands were measured. Furthermore, an inverse problem was conducted to predict the structure and material parameters of a crystalline solar cell following the permutations available in the solar cell industry. This developed model for solar cells can be easily incorporated in full-wave analysis with arbitrary antennas.

Chapter 4

Antenna Radiation Efficiency Prediction

4.1 Introduction

The prediction of the radiation efficiency of arbitrary antennas through measurements is considered a difficult task [59, 60]. Yet, it is an important performance figure of merit for antennas that designers care about for various applications. Depending on the available measurement facilities, different prediction procedures have been proposed through literature with different limitations and accuracy levels [59, 60]. In general, the antenna radiation efficiency (η_r) represents the Ohmic losses inside the antenna structure in comparison to the radiated power [48] as

$$\eta_r = \frac{P_r}{P_a} = \frac{G}{D} \tag{4.1}$$

where P_r and P_a are the radiated and accepted power by the antenna ports, respectively, D and G are the antenna directivity and gain, respectively. Many measurement techniques have been presented to measure this quantity, which vary in terms of the required equipment and anticipated accuracy as presented in [59, 60].

4.1.1 Previously Introduced Measurement Techniques

According to the availability of various antenna/microwave measurement equipment, different procedures have been proposed to predict the antenna efficiency, namely: *the pattern integration method* [59], *the radiometric method* [61], *the directivity/gain method* [60], *the reverberation chamber method* [62], and *the Wheeler cap method* [63]. Each method requires a distinct setup and instrumentation that varies in frequency range of operation, the required space, and cost.

The pattern integration method is considered a direct implementation of Eq. (4.1) by simply integrating the radiation pattern of the antenna over a complete sphere in the far field to evaluate the radiated power. The accuracy of calculating the above equation depends directly on the number of points taken on a sphere to evaluate the integration. Also, the resolution to distinguish between antennas with close efficiency values is highly affected by the accuracy of the measuring devices. The only concern about this method is the need for a large anechoic chamber to evaluate the efficiency of antennas operating at low frequency [59]. The difficulty to obtain far field radiation patterns makes this method only suitable for antennas which measurements of radiation patterns in two planes are sufficient to represent the 3D antenna radiation pattern. Moreover, near to far field type measurements can be of use for this frequency range, but this requires a different setup though. Other similar approaches to this method have been introduced in [64, 65] that also require measurements inside the anechoic chamber with sorts of integration of the measured data.

The radiometric method is based on measuring the noise temperature produced by an antenna as a means to measure the antenna efficiency. The method is based on the idea that the losses inside an antenna contributes much to the produced noise temperature in the ambient temperature [61, 66]. This procedure setup requires a noise figure meter to measure the noise temperature of the antenna. The main inconvenience about this method is that it requires the antenna to be pointed towards

the sky or at least have an electrically transparent view of the sky for the cold measurement [66]. This requires an antenna measurement to be done outdoors or at least through a transparent roof with a reflector. Therefore, this method is suitable for directive antennas.

The directivity/gain method is also a direct evaluation of Eq. (4.1) by obtaining both values of the gain and directivity of an antenna [60]. The gain value can be obtained from a standard horn antenna setup experimentally. The directivity value can be obtained by either numerical analysis or by using the approximated formulas that relate the beam width to directivity [48]. Since measuring both quantities are completely not related, a lot of error sources are present (human error and fabrication tolerance). However, this method can be used to quickly obtain the efficiency value. Moreover, this method is also very reliable to get the radiation efficiency of directive antenna.

The reverberation chamber method is used to measure the antenna efficiency in multipath environment [62,67]. It is used to measure the antenna efficiency in a closer to reality approach. This is achieved by involving moving objects and changing the AUT position inside the metallic reverberation chamber. The results of this technique are pretty much comparable to the Wheeler cap method [68], which is the core of the proposed work without the need for a reverberation chamber setup.

4.1.2 The Wheeler Cap Method

Wheeler cap method, proposed in [63], is considered among the simple and cost effective methods to measure the radiation efficiency of small size antennas compared to the other procedures [60]. Originally as proposed by Wheeler in [63], the method was developed for electrically small antennas. It assumed simple resonator circuit(s) to model the antenna operation, where the power dissipation is due to radiation and Ohmic losses. The main advantage of this technique is the need for only reflection

coefficient measurements at the antenna port rather than three dimensional far-field measurements. Furthermore, the Wheeler cap method is advantageous for low frequency antennas as anechoic chambers that can operate in that frequency band are not easily available [59]. In addition, several enhancements to the Wheeler cap measurement procedure have been presented to enable the method to be used beyond small antenna. Higher order circuit models for higher order modes have been exploited for antennas that cannot be modeled by simple resonator circuits or for wide band responses as presented in [69, 70] and further improved in [71]. The presented results of these equivalent circuit based Wheeler cap methods show significant accuracy and flexibility to accommodate different antennas. However, the employed higher order circuit models add numerical overhead to the development process.

In addition, circuit model independent procedures have been introduced in [72–76], which alleviated the effort required to develop antennas' circuit models. These methods also provide reasonable approximations for radiation efficiency even in the presence of several cavity modes besides the antenna mode(s) inside the Wheeler cap. The Improved Wheeler Cap method (IWC), proposed in [72] provided results for single mode and narrow band antennas even in the presence of 'few' cavity modes by using different sized Wheeler caps. The procedure was modified in [73, 74] to incorporate the antenna frequency response instead of using different Wheeler caps. Moreover, further refinements to the IWC method have been proposed in [75, 77]. Furthermore, another Modified Wheeler Cap method (MWC) was proposed in [76] and further corrected in [78] to predict the radiation efficiency of ultrawide band antennas using spherical Wheeler caps and multiport network analysis. Results comparison between the available circuit model independent procedures and the proposed procedure in this work are presented at the end of work for completeness of the study.

The concept of using quality factors with Wheeler caps to approximately predict radiation efficiency is used in [59, 79, 80]. These references predicted radiation

efficiency for small or narrow band antennas based on approximate expressions, as presented in [81]. Recently, a circuit model independent Wheeler cap method was proposed based on computing quality factors for various types of antennas and responses [82, 83]. The method provides better approximations for radiation efficiency for different antenna types ranging from small antennas, dual band antennas and wide band antennas. However, the provided expressions have not yet been proven suitable for the different responses related to Wheeler cap measurements. In addition, reproduction of results and the stability of the procedure have not been discussed in details. Thus, several studies are required to be presented to evaluate the potential of using the Quality factor ($Q\text{-}factor$) method, which is the focus of this work.

In this work, the design procedure is introduced for the contactless Wheeler cap. Different wide band electromagnetic shielding techniques are accommodated through the proposed designs. The shielding concept is simple, it is based on surrounding the cap with a flange of Perfect Magnetic Conductor (PMC) surface that is when parallel with a metallic conductor prevents leakage in between where the separation is less than a quarter wavelength. As such, it acts as a high pass filter between the cap edge and the outer edge of the flange. The magnetic conductor surface is artificially realized using periodic electromagnetic band gap (EBG) that is acting as an artificial magnetic conducting (AMC) surface. Once it is artificially realized it acts as a band stop filter. To use the Wheeler cap for wideband application, the bandwidth of such filter is increased to cover an extremely wide band. Furthermore, two different designs are presented to cover the frequency bands from 1.5 GHz to nearly 40 GHz accommodating the usual antenna design environment into the design of the shielding flanges, such as large ground planes, dielectric substrates and solar cells. The designed Wheeler caps shielding quality are tested through measuring quality factors of cavity modes, which indicate the quality of measurements at frequencies close to these cavity modes. The results of the proposed designs are verified with

measurements for different antenna types and frequency bands in different antennas' environments.

4.2 Efficiency Prediction Procedure

The process begins with fitting the antenna response in free-space and inside the shielded Wheeler cap into a rational function $\Gamma(s)$ as a function of the complex frequency $s = \sigma + j\omega$, similar to [84] viz

$$\Gamma(s) = \frac{a_n s^n + a_{n-1} s^{n-1} + \cdots + a_1 s + a_0}{b_n s^n + b_{n-1} s^{n-1} + \cdots + b_1 s + 1} \tag{4.2}$$

where a_n and b_n are constants evaluated by the complex least square fitting method [85]. The maximum order of the polynomials is determined adaptively through the process to insure the satisfaction of a pre-specified error tolerance between the measured and fitted curves. A maximum allowed polynomial order value can be set to 15 $\sim$ 20 to avoid numerical errors through the process related to the machine saturation or round up. Also, the frequency range of the measured reflection coefficient can be divided into separate frequency segments if the error is not satisfactory using the maximum allowed order. An adaptive approach can be programmed for this process to ensure continuity of the response(s) and their derivative. Once the reflection coefficient is effectively represented by the rational function(s), the quality factor can be easily evaluated using the invariant formula in [86] without assuming a circuit model for the antenna as

$$Q = \frac{\omega_0 \left| d\Gamma(s)/d\omega \right|}{1 - \left|\Gamma\right|^2} \tag{4.3}$$

where ω_0 is, by definition, the resonance angular frequency of the unloaded resonator and Q is the loaded quality factor including the effects of the coupling network. Typically, the slight difference between the loaded and unloaded resonance frequencies

should not affect the results of the proposed procedure as shown in [86,87].

Respecting the radiansphere of the Antenna Under Test (AUT) by the Wheeler cap, the cap is assumed not to add losses to the measurement setup. Thus, the evaluated quality factor of the antenna inside the Wheeler cap is considered to represent the losses of the antenna only. Consequently, the antenna efficiency can be computed knowing the quality factor values for the antenna in free-space Q_a and inside the Wheeler cap Q_w using a simple expression that can be easily derived [59, 79] as

$$\eta_r \simeq 1 - \frac{Q_a}{Q_w}. \tag{4.4}$$

Also, the total efficiency of the antenna can be calculated by introducing the return loss into the total losses in the system as $\eta_t = \left(1 - |\Gamma_a|^2\right) \eta_r$, where Γ_a is the reflection coefficient of the antenna in free-space.

It is essential to elaborate that the main benefit of going through the described procedure is the accuracy in accommodating the measured responses. The proposed method is a good candidate to deal with under-sampled measurements, where it can reliably predict the response and its derivative in between the measured samples. This feature is directly inherited in the quality factor evaluation when it is evaluated analytically from the reflection coefficient in Eq. (4.4).

Another important property of the fitted expression, which is already implemented in most of nowadays full-wave solvers, is the ability to accurately determine the resonances of the measured structure. In case of measuring the antenna response in free-space, the resultant poles and zeros are for the antenna resonance frequency(ies) within measurement frequency band along with other numerical artifact resonances outside the measurement band. The distance between the pole/zero and the $j\omega$ axis in the s complex plane is inversely proportional to the radiating mode bandwidth (i.e. the distance is proportional with the losses in the system). Alternatively, the

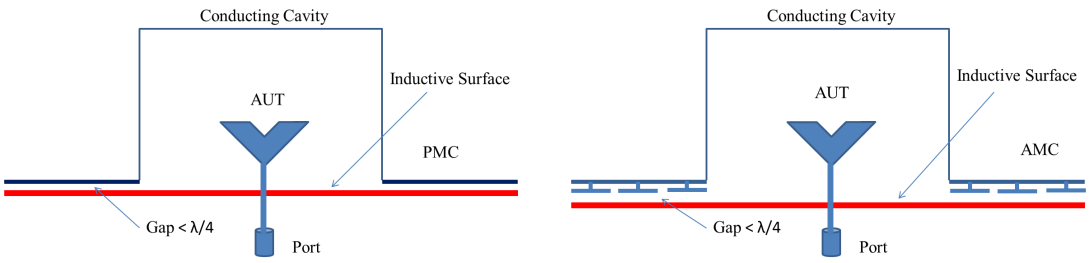

Figure 4.1: An illustration to the proposed contactless Wheeler cap concept. (a) The ideal model using a PMC flange that acts as high pass filter. (b) The realization of the shielding flange using an AMC flange that acts as a band stop filter.

response of the antenna inside the Wheeler cap has pairs of poles and zeros related to the antenna resonance(s) (slightly shifted) and cavity modes condensed near the $j\omega$ axis. The antenna modes can be identified within the pool of the cavity modes in a large Wheeler cap measurement setups by observing the distance between the pole and zero in the s plane. Cavity modes correspondent poles and zeros are always very close to each other compared to antenna modes correspondent poles and zeros. This can be used to even develop circuit models for antennas based on the type of resonator depicted from the zeros and poles interpretation to be used even with the original Wheeler cap concept. This can be used to automatically identify cavity modes that interact with the antenna, as approximations, that could give us an indication of how good the efficiency prediction is at these frequencies as elaborated in Appendix A.2.2.

4.3 The Contactless Wheeler Cap

Many possible scenarios cannot be properly shielded based on the conventional Wheeler cap. The proposed contactless Wheeler cap provides the electromagnetic shielding for such scenarios by using an evanescent wave structure. Such structure consists of two parallel plates of Perfect Electric Conductor (PEC) and Perfect Magnetic Conductor (PMC) separated by a distance of less than $\lambda/4$ [88] (PMC top and PEC bottom,

PMC/PEC) as shown in Fig. 4.1 (a). This insures no propagation between these two plates to provide the required shielding. This is acting also as a high pass filter. Some of these scenarios involve having antennas above inductive surfaces, such as dielectric substrates. Here, we design a square cross section Wheeler cap with an EBG flange to provide Artificial Magnetic Conductor (AMC) as shown in Fig. 4.1 (b). An arbitrary wide band performance of the shielding flange can be obtained by invoking bandwidth enhancement techniques such as stacking [89] and cascading [90] for unit cells. Consequently, the metallic shield is designed also to accommodate a moderate-sized antenna that occupies ($\lambda_0/2 \times \lambda_0/2 \times \lambda_0/4$) at the lowest frequency in the desired band. In addition, the metallic shield is required to achieve the radiansphere distance to the antenna as presented in [63]. This makes the minimum required Wheeler cap size of ($0.66\lambda_0 \times 0.66\lambda_0 \times 0.41\lambda_0$) at the lowest design frequency. The following subsections discuss in detail the proposed design and its advantages. Also, two different Wheeler cap designs are proposed to cover the frequency bands from 1.5 GHz to nearly 40 GHz using the proposed concept.

4.3.1 The Employed EBG Unit Cell

The use of conventional mushroom-shaped structures, proposed in [57], for low frequency applications requires using large structure dimensions. This usually leads to a large size for the Wheeler cap shielding flange; especially if a multi-cell cascaded approach is implemented to obtain large bandwidths. It is well known that the bandwidth of the mushroom EBG type is proportional to the substrate thickness and inversely proportional to the dielectric constant [58]. However, using too thick materials is non-preferred from a mechanical point of view because this limits the ability to use fine drills to create the necessary vias. This is because each fabrication process is limited to certain minimum aspect ratio between the via diameter and substrate thickness, which varies from one process to another. Also, increasing the

dielectric constant to decrease the overall structure size has a negative impact on the bandwidth [58]. In order to reduce the cell size and enhance the bandwidth, a new cell is proposed to increase the overall thickness by cascading separate non-touching layers. The new cell takes into consideration some electrical and mechanical scenarios that might exist in the final product such as poor electrical contacts and fabrication minimum drilling aspect ratio in making vias. The structure consists of two stacked mushrooms shaped with an extended capacitive gap between the layers to accommodate any air gap or poor contact between layers as shown in the cross section view in Fig. 4.2 (a) with the equivalent circuit model shown in Fig. 4.2 (b). In the circuit model, it is clear that the inductance L and capacitance C_1 are the same as the circuit model of the conventional mushroom-shaped structure [89], but the capacitance C_2 is mainly the effect of the extended capacitive gap introduced between layers separated by the distance ($G = 0.1$ mm) in Fig. 4.2 (a). The resonance frequency of such structure can be manipulated to be

$$\omega_0 = \frac{1}{\sqrt{L\left(\frac{1}{C_1} + \frac{1}{C_2}\right)^{-1}}} \tag{4.5}$$

which means that the larger the value of C_2 compared to C_1, the more the performance becomes closer to a conventional thick mushroom-shaped structure. Fig. 4.3 shows the electrical advantage using this structure in terms of achievable band gap compared to the single layer design with the same unit cell outline with thick and thin substrates. The used stacked unit cell dimensions are $D_1 = D_2 = D_t = 1.575$ mm, $H = 0.1$ mm, $P = 14.5$ mm, $W_2 = 14.3$ mm, and via diameter of 0.5 mm. Also, the single layer mushroom-shaped structures has the width of the patch $W = 14.3$ mm and period size $P = 14.5$ mm to be compliant with the stacked version with substrate thickness of 1.575 mm for the thin unit cell and 3.15 mm for the thick unit cell. It is important to mention that all the unit cells are designed using Rogers material 5880 with $\varepsilon_r = 2.2$.

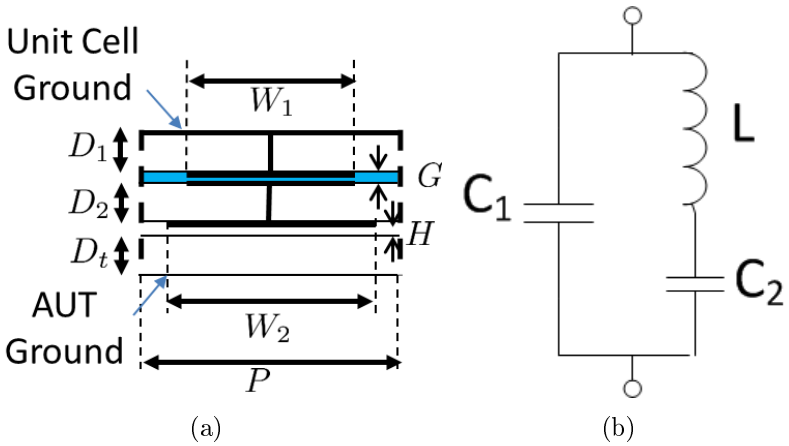

Figure 4.2: The proposed EBG unit cell. (a) A cross section of the square unit cell. (b) Equivalent circuit model.

The main benefit of the employed unit cell is its compactness when compared to the original mushroom-shaped structure, which reaches around 15% of the side dimension to have the same starting frequency of the band gap. Also, the exploited unit cell features a larger bandwidth ratio, that reaches around 2.15 compared to 1.66 for the thin substrate design. Moreover, the design accounts for the possibility of having an unavoidable air gap between layers ($G = 0.1$ mm). Of course, the smaller the air gap, the better the performance of the unit cell. However, the design considers the aging effect, which may result in having an oxide layer on top of the copper that reduced the contact quality.

Another important advantage of the proposed unit cell is the tolerance to slight misalignment that could happen through the assembling process. Fig. 4.4 (a) shows the misalignment representation in one plane cut by the value δ, where in practice this misalignment can happen in both planes (δ_x and δ_y). The original dispersion diagram for the first 3 modes of the optimum unit cell with the same outline dimensions as introduced above with $W_1 = 12$ mm is shown in Fig. 4.4 (b). Figs. 4.4 (c) and 4.4 (d) show the dispersion diagrams for the misaligned structure, which shows a slight variation in the unit cell performance. This advantage can be of great use if this unit

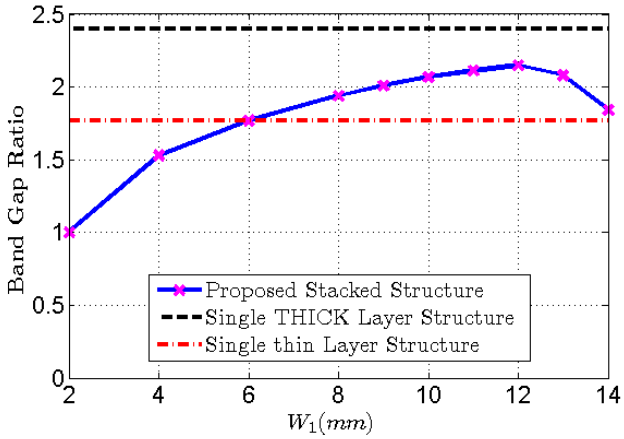

Figure 4.3: The intermediate square patches width W_1 effect on the proposed unit cell band gap performance in comparison with its compliant thin and thick single layer unit cells' band gaps.

cell is used for mass production. It is also worth stating that this arrangement does not require using an adhesive material to join the two substances. Nevertheless, the indicated values on the horizontal axes in the dispersion diagrams are specific points with transverse wavelength (k_x and k_y) as

$$\Gamma: \ k_x = 0, \ k_y = 0, \tag{4.6}$$

$$X: \ k_x = \frac{2\pi}{P}, \ k_y = 0, \tag{4.7}$$

$$M: \ k_x = \frac{2\pi}{P}, \ k_y = \frac{2\pi}{P}, \tag{4.8}$$

following the same procedure indicated in [58].

4.3.2 Design 1: 1.5 - 4 GHz

The first Wheeler cap design is made to cover the frequency range from 1.5 to 4 GHz. As the employed procedure exploits the cascading concept to enlarge the Wheeler cap bandwidth, the bandwidth ratio is arbitrarily chosen here to be 2.67 to have a reasonable size structure. The Wheeler cap metallic shield size is chosen to be (165 mm $\times$ 165 mm $\times$ 82 mm). This design considers the worst case AUT environment

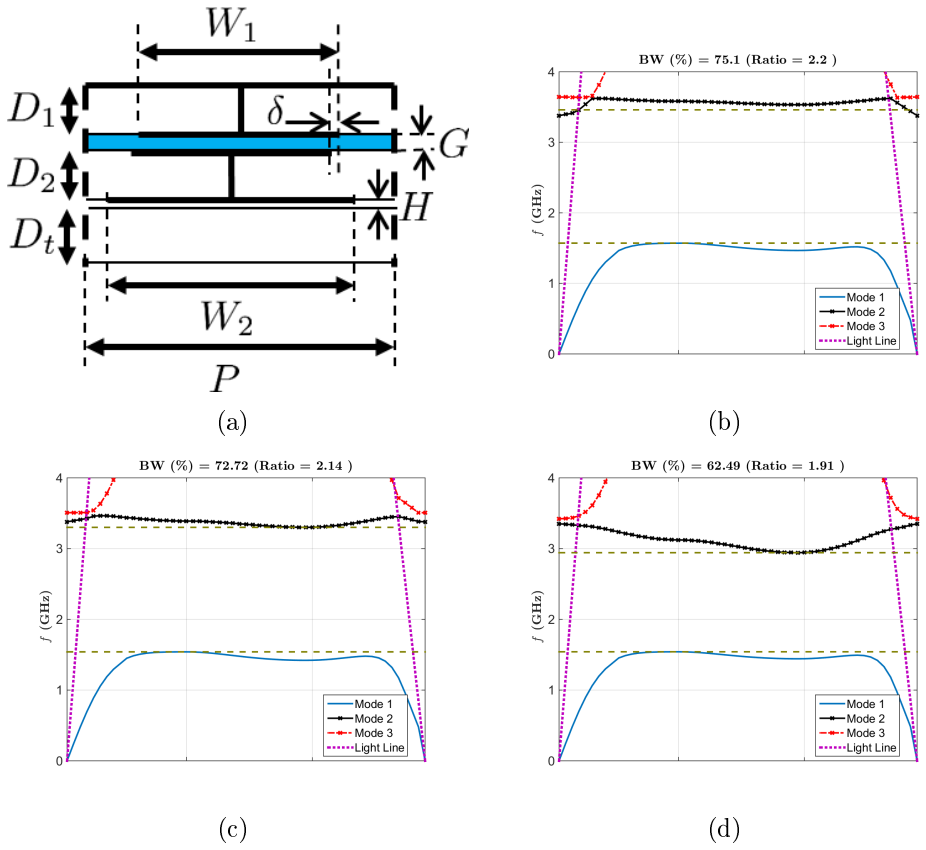

Figure 4.4: Misalignment effect on the proposed EBG unit cell. (a) Plane cut illustration. (b) Dispersion diagram of the aligned unit cell ($\delta_x = \delta_y = 0$). (c) Dispersion diagram of the misaligned unit cell ($\delta_x = \delta_y = 1$ mm). (d) Dispersion diagram of the misaligned unit cell ($\delta_x = \delta_y = 2$ mm).

scenario to be an antenna printed above or in the presence of large dielectric substrate of Rogers material 5880 with $\varepsilon_r = 2.2$ and thickness 1.575 mm. That means the Wheeler cap edge cannot be electrically connected to the ground plane of this substrate and the contaclless Wheeler cap flange will be separated from the substrate ground plane by such a thickness. The EBG flange consists of two different cascaded unit cells to achieve the required bandwidth as shown in the layout in Fig. 4.5, where the dimensions are presented in Table 4.1. Generally, the unit cell periods' dimensions are chosen to have a small least common multiplier value. For fabrication cost and design rigidity, the substrate material has been chosen to be FR4 ($\varepsilon_r = 4.3$) with thickness 1.575 mm, which is more rigid than the Teflon based material with $\varepsilon_r = 2.2$

Figure 4.5: The layout of Design 1 shielding flange.

Table 4.1: Design 1 cells' dimensions, band gaps, and chosen number of rows as presented in the layout shown in Fig. 4.5.

Cell Set #	P mm	W_2 mm	W_1 mm	r_{via} mm	Band Gap GHz	N_{rows}
1	8	7.85	6.1	0.15	2.34 - 4.53	3
2	12	11.85	10	0.15	1.5 - 2.78	4

with the same thickness. Of course, this choice reduces the achievable band gap from a unit cell, but it has many manufacturing and mechanical properties that make it a better choice for the application.

Using a simplified parallel plate setup to measure the isolation of a limited number of rows of each cell as shown in Fig. 4.6, the overall isolation of the cascaded structure can be depicted from the overall envelope of individual cells' isolation as shown in Fig. 4.7 (a). This simulation model is expected to be more accurate than the one presented in [90] due to the more precise placement for the symmetry planes that matches the expected field distribution. The design is expected to perform better in terms of band gap performance for thinner antenna environment substrates or even an air gap. Having only a small air gap between the EBG flange and the ground plane ($\sim$ 0.1 mm), the isolation performance of the proposed shielding flange is enhanced in terms of level and bandwidth as shown in Fig. 4.7 (b). Results show that having the design operating in the stated dielectric environment with a specific electric gap height includes the operation of the same design with smaller electric gap heights.

Fig. 4.8 shows views of the fabricated model of the designed contactless Wheeler

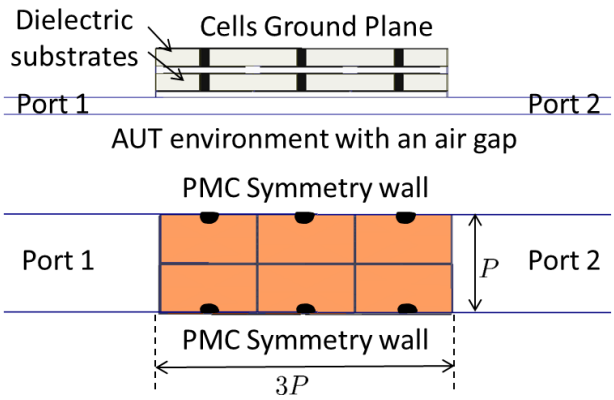

Figure 4.6: Simplified simulation model to measure the isolation of a limited number of rows of unit cells. The top figure is the side view of the setup and the bottom figure is the top view.

cap. The metallic shield is made with brass sheets with thickness 0.254 mm soldered to the ground plane of the EBG isolation flange. The double layer EBG structure is fixed with 8 brass screws aligned with vias not to disrupt the periodicity of unit cells. The overall side dimension of this square Wheeler cap design is 309 mm.

It is interesting to investigate the implication of using the proposed unit cell on the overall size of the shielding flange. As elaborated before about the compactness factor enhancement introduced by the proposed unit cell, which is around 15% of the side dimensions to have the same band gap starting frequency. The achievable bandwidth ratio is another factor to consider. This means that to cover the desired bandwidth of the presented contactless Wheeler design, 3 different cell sets have to be used. The largest cell should have a side dimension of at least 13.8 mm. The second and third cell sets should have side dimensions of 9.2 mm and 6.9 mm, respectively, to perfectly fit in the overall layout. Considering a minimum number of rows for each cell set to be 3, this results in having the overall side dimension of the square Wheeler cap to be 344.4 mm (24% increase of area compared to the presented design). However, the required shielding through the whole operating frequency band has to be studied extensively to determine the optimum number of rows for each cell set, which should be equal or larger than 3. Therefore, the overall increase of the design surface area

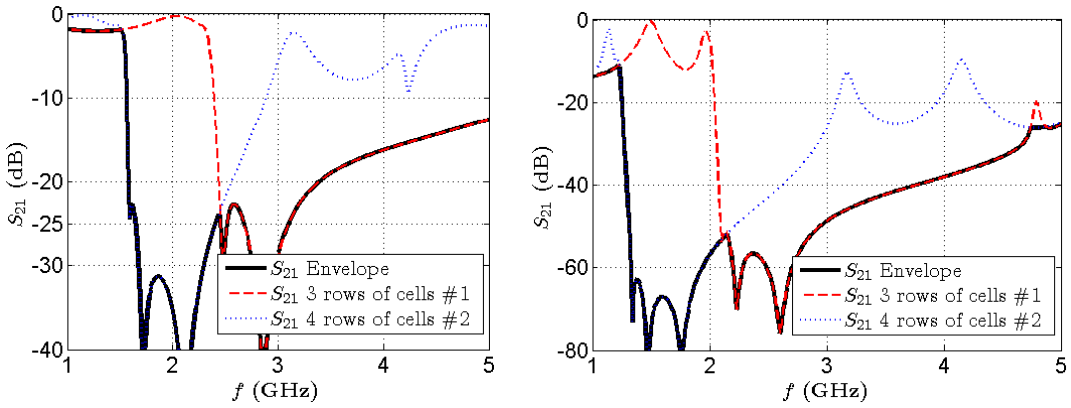

(a) (b)

Figure 4.7: The overall isolation performance of the proposed cascaded structure depicted from the performance of individual cells [90]. (a) with AUT environment of 1.575 mm and $\varepsilon_r = 2.2$. (b) with 0.1 mm air gap as the AUT environment.

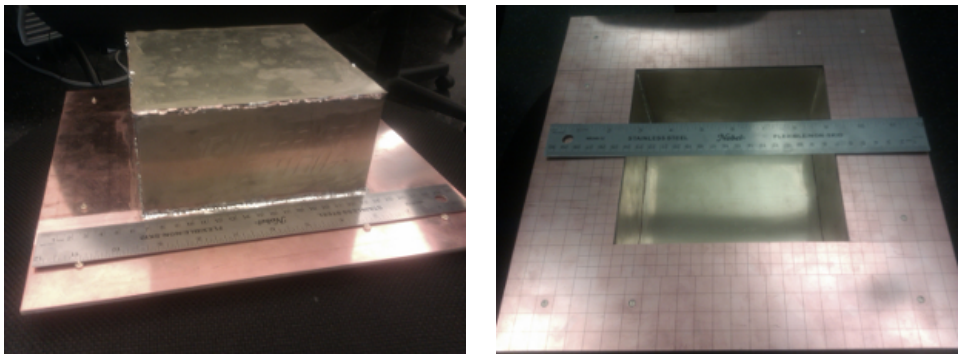

(a) (b)

Figure 4.8: The fabricated model for Design 1.

can be even larger.

4.3.3 Design 2: 3.5 - 40 GHz

Extending the same design concept presented in the previous design, another Wheeler cap can be designed for an upper band. The bandwidth ratio is chosen to be large in this case to the maximum achievable reasonable ratio as the resultant structure is small. This is mainly to cover a wide range of antenna applications and bands. First, the Wheeler cap dimensions are chosen to satisfy the necessary conditions to

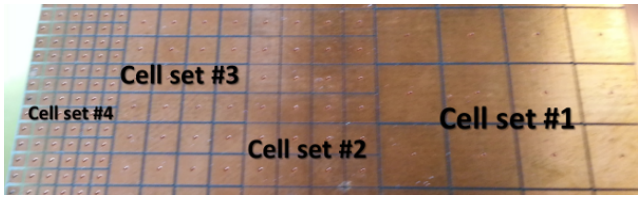

Figure 4.9: The layout of Design 2 shielding flange.

be (63.8 mm × 63.8 mm × 31 mm). Then, the isolation EBG flange is designed to cover the required frequency band. Following the same design considerations and procedure as shown before, the layout of the shielding flange is shown in Fig. 4.9. The dimensions of the different cascaded cell sets are presented in Table 4.2. It is noticed that the band gap ratio of the proposed unit cell deteriorates as the unit cell size decreases. Therefore, single thin layer designs are incorporated through this design to allow the device to operate at high frequencies as illustrated in Table 4.2 for cell sets #3 and #4. These unit cells are characterized only by the period P, the square patch width W_2, and via radius r_{via} dimensions. The transition between different unit cell configurations is designed and studied extensively to insure there is no leakage when the waves travel from one type to the other. The proposed solution for this transition is shown in Fig. 4.10 featuring duplication of single layer design in the stacked environment. This prevents leakage between the layers using the fact that the band gaps of the bottom cells with the small air gap includes the band gap of the top cells with larger gap. The overall performance of the isolation with a dielectric material with $\varepsilon_r = 2.2$ and thickness 1.575 mm using cascaded sections of two adjacent cell types is shown in Fig. 4.11 (a), which is below -25 dB from 3.5 to 18 GHz.

Alternatively, it is usually expected to use much relieved conditions for the AUT environment at frequency bands around the 20 GHz. Therefore, the isolation performance of the designed shielding EBG flange improves in such conditions. Fig. 4.11 (b) shows the overall isolation performance of the proposed cascaded structure

Table 4.2: Design 2 cells' dimensions, band gaps, and chosen number of rows as presented in the layout shown in Fig. 4.9.

Cell Set #	P mm	W_2 mm	W_1 mm	r_{via} mm	Band Gap GHz	N_{rows}
1	5.8	5.6	4	0.15	3.44 - 5.99	4
2	2.9	2.8	2.25	0.15	6.59 - 8.44	4
3	2.9	2.7	NA	0.15	6.87 - 12.98	4
4	1.45	1.25	NA	0.15	12.02 - 18.55	6

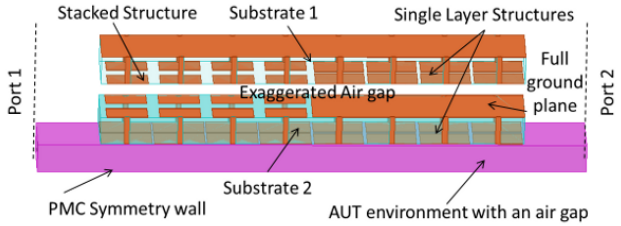

Figure 4.10: The transition between stacked cells to single thin layer EBG cells (between cells' sets #2 and #3 in 'Design 2' structure).

in pairs for the AUT environment of $\varepsilon_r = 2.2$ and thickness 0.508 mm . The results show that the isolation bandwidth covers the frequency range from 3.2 to 25 GHz. Also, the isolation performance of the proposed Wheeler cap covers up to 40 GHz if used directly on top of a ground plane with a typically predicted air gap of 0.1 mm.

The fabricated model is shown in Figs. 4.12 (a) and 4.12 (b). The layout order of the different cell sets that is intentionally started with the higher frequency band from the inside to the lower frequency band on the outside for different electrical and mechanical advantages. From an electromagnetic prospective, waves travel small electric distances before they are blocked by the correspondent EBG structure, which reduces the amount of losses in the FR4 substrate. The opposite layout leads the high frequency components to travel a longer electrical distance before getting blocked by their corresponding EBG cells. The mechanical advantage in the current layout is the need for less number of patches and in turn less number of vias, which is considered a challenge for fabrication.

Another important issue concerning holding the two layers together is to use

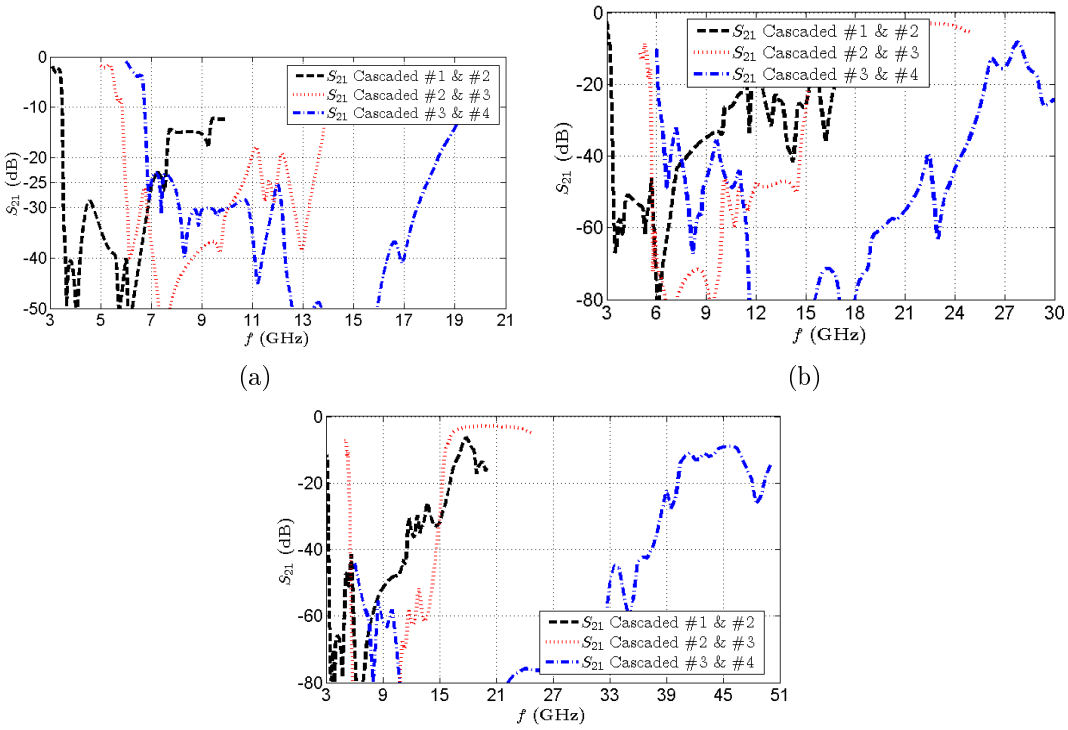

Figure 4.11: The overall isolation performance of the proposed cascaded structure depicted from the performance of individual cells [90]. (a) (a) with AUT environment of 1.575 mm and $\varepsilon_r = 2.2$. (b) with AUT environment of 0.508 mm and $\varepsilon_r = 2.2$. (c) with 0.1 mm air gap as the AUT environment.

'metallic' (2-56) screws and nuts as shown in the Figs. 4.12 (a) and 4.12 (b). The original idea was to use just plastic screws of the same size to minimize perturbation of the structure, but leakage was observed in the frequency band of the altered EBG cells. So, the solution was to use metallic screws and nuts instead. The heads of the screws are counter-bored in the PCB surface to prevent any unwanted presence of air gap. Of course, gluing the two substrates together would give better results only when the used glue has a very small thickness. However, this process requires pressure and heating, which need special setups that are avoided in this work.

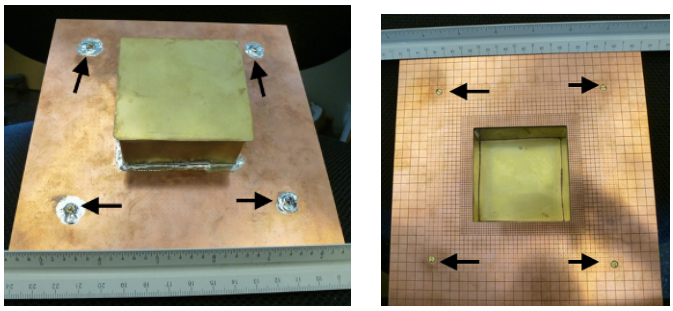

(a) (b)

Figure 4.12: The fabricated model for Design 2. The arrows point to the screws and nuts positions.

4.4 Measured Quality Factors

Measuring the quality factors of the employed Wheeler cap helps to predict the quality of the measured radiation efficiencies upon interacting with arbitrary cavity modes as explained in Appendix A.2. Using a short probe inserted inside the shielded Wheeler cap cavity, the cavity modes' quality factors can be predicted through the procedure presented in Eqs. (4.2) and (4.3). Typically, analytical analysis of rectangular cavities made of brass results in quality factor values in the order of 20000 [91]. However, these values may be reduced due to using lead solder and also lossy substrates for the EBG shielding flanges. Therefore, for the 'Design 1' contactless Wheeler cap, the predicted quality factors using a copper ground plane with a typical air gap distance to the EBG surface or around $0.1 \sim 0.2$mm are presented in Fig. 4.13. The presented quality factor values are mostly around few thousands. However, by the end of the designed frequency band (~ 4 GHz), the quality factors drop due to leakage from the Wheeler cap. Thus, this Wheeler cap is suitable for our measurements within the design frequency band.

Furthermore, the same procedure has been conducted for 'Design 2' contactless Wheeler cap for different scenarios. Initially, the stacked EBG structure is fixed together using four screws as shown in Fig. 4.12. Thus, the measured quality factors

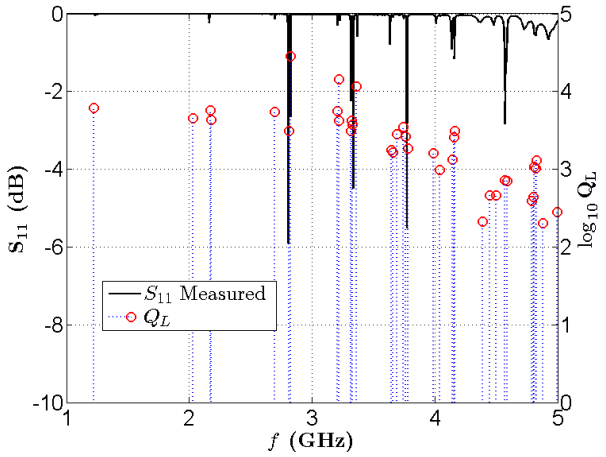

Figure 4.13: The predicted cavity modes' quality factors of 'Design 1' contactless Wheeler cap obtained through measurements.

over an aluminum ground plane are shown in Fig. 4.14 for the frequency range from 3 GHz to 26 GHz, which is the end of the employed high quality SMA connector. The measured quality factors show and increasing behavior as frequency increases till 10 GHz is reached. Then, the quality factors within the frequency band of the mushroom shaped EBG set #4 are almost around 10000, which is favorable for the proposed purpose. However, low quality factor values are observed at lower frequency bands, which can be either due to undesired leakage as a result of using screws or due to losses due to propagation though lossy parallel plate structure as noticed in Figs. 4.7 and 4.11 below the bandgap frequency range. To clarify the reason for these low quality factors, another contactless Wheeler cap measurement setup is built without using screws as shown in Fig. 4.15. The measured quality factors using this setup are shown in Fig. 4.16 indicating similar losses trend as presented in the previous case in Fig. 4.14, which indicate that the reason behind the low quality factor values is propagation through a lossy parallel plate guide. The consequence of this observation is to expect errors around the coupled cavity mode to the antenna mode with the impact governed by Eq. (A.5). Nevertheless, the same procedure is applied to measure the quality factors of the contactless Wheeler cap cavity having a

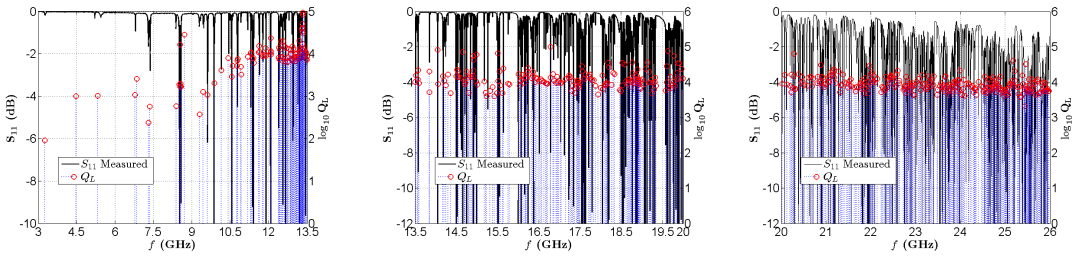

(a) (b) (c)

Figure 4.14: The predicted cavity modes' quality factos of 'Design 2' contactless Wheeler cap obtained through measurements.

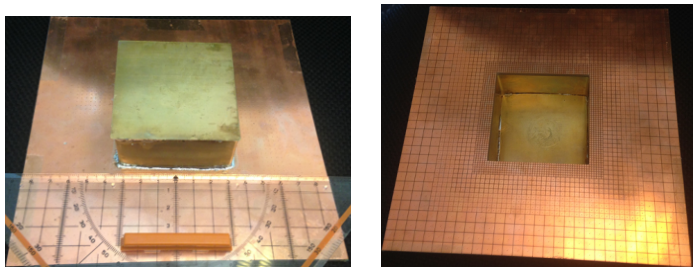

(a) (b)

Figure 4.15: The fabricated model for Design 2 without using screws.

solar cell as a ground plane, which should behave closely to ground planes as depicted from Chapter 3. The measured quality factors are shown in Fig. 4.17 indicated lower values due to power consumption in the solar cells lossy structure. This consequently adds uncertainty to the measurement as explained in Appendix A.2.2 around the coupled cavity modes. However, the envelope of the predicted radiation efficiency curve still contains the necessary information about the performance of an antenna within this lossy environment as employed for other Wheeler cap post-processing procedures [78, 92].

4.5 Measurement Results

In this section, verification measurements using the proposed setup are conducted to test its potential. Then, measurements of the radiation efficiency of integrated

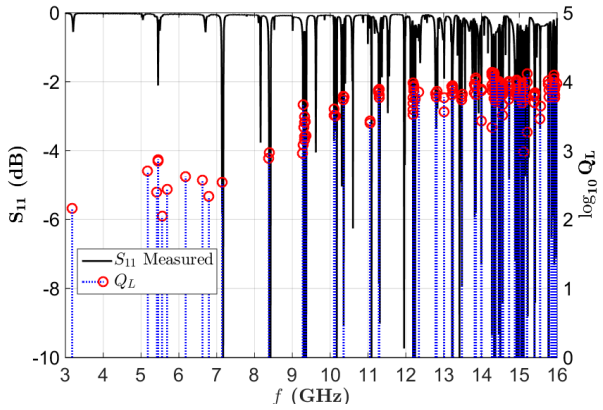

Figure 4.16: The predicted cavity modes' quality factors of 'Design 2' contactless Wheeler setup shown in Fig. 4.15.

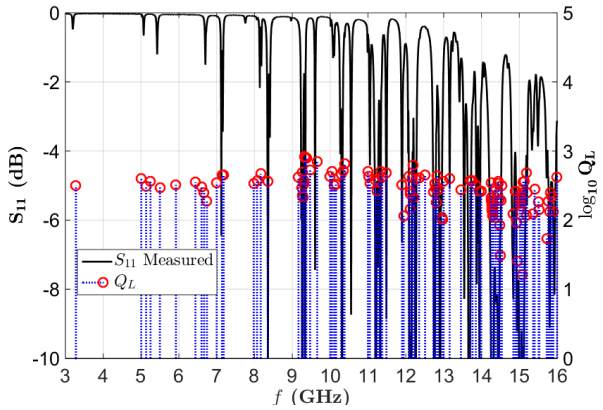

Figure 4.17: The predicted cavity modes' quality factors of 'Design 2' contactless Wheeler setup using solar cells as a ground plane.

antennas with solar cells are presented.

4.5.1 Verification Cases

The first case is the A-Shaped DRA antenna [93]. The antenna geometry is shown in Fig. 4.18 (a) with dimensions $W = 14$ mm, $W_w = 6$ mm, $W_{L1} = W_{L2} = 6.7$ mm, $L_{D1} = L_{D2} = 9.15$ mm, $F_{L1} = 5.4$ mm, and $F_{L2} = 13$ mm. Using Design 2 of the proposed contactless Wheeler cap setup, the measured antenna efficiency is presented in Fig. 4.18 (b). As expected, the employed DRA has a high radiation efficiency ($97\% \sim 99\%$)as reported in the literature [93] and shown in Fig. 4.18 (c).

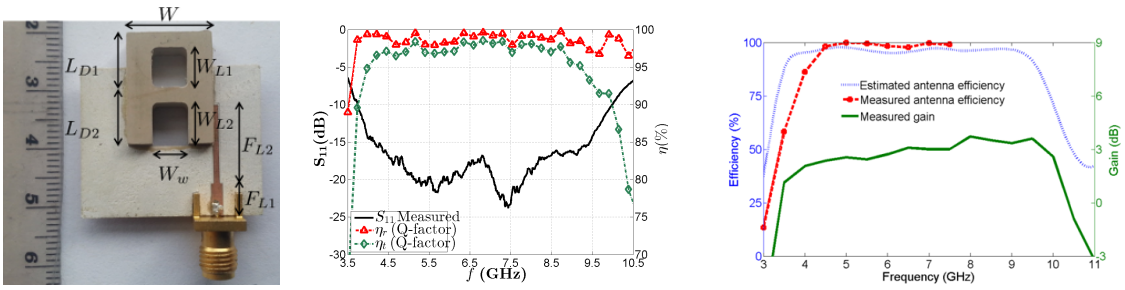

(a) (b) (c)

Figure 4.18: The employed model for the A-Shaped DRA [93] with the measurement results. (a) Fabricated model with geometry parameters. (b) Measured antenna efficiency and reflection coefficient. (c) The reported antenna efficiency in [93] ©2010 IEEE.

The reported results are for the total radiation efficiency, which includes the return loss into consideration for the antenna efficiency. It is important to notice that since the original antenna has a vertical ground plane, the antenna has to be contained inside the Wheeler cap and a horizontal large ground plane.

The second verification case is for a circular patch antenna operating at 10 GHz fabricated on a Rogers 5880 material ($\varepsilon_r = 2.2$) with a height of 1.575 mm. The radius of the patch is $r_{patch} = 5.05$ mm. Also, the dielectric substrate is intentionally made oversize to test the shielding capability of the fabricated model of the contactless Wheeler cap using the same design environment as in Sec. 4.3.3. The fabricated patch antenna and results are shown in Fig. 4.19 presenting very close prediction for the radiation efficiency of the patch antenna (within 2% percentage points). Also, the effects of the coupled cavity modes are shown to minimally affect the measured values due to the low losses inside the dielectric substrate material of the patch antenna. It is important to illustrate that this method answers the missing part in [94] by proposing a technique to measure the antenna efficiency of conventional patch antennas.

Another measurement case exploits the linearly polarized wide band antenna that is based on Huygene's principle presented in [95]. The antenna structure is presented in Fig. 4.20 with dimensions $W = 60.1$ mm, $L = 30.2$ mm, $H = 30.5$ mm, $b = 22.9$

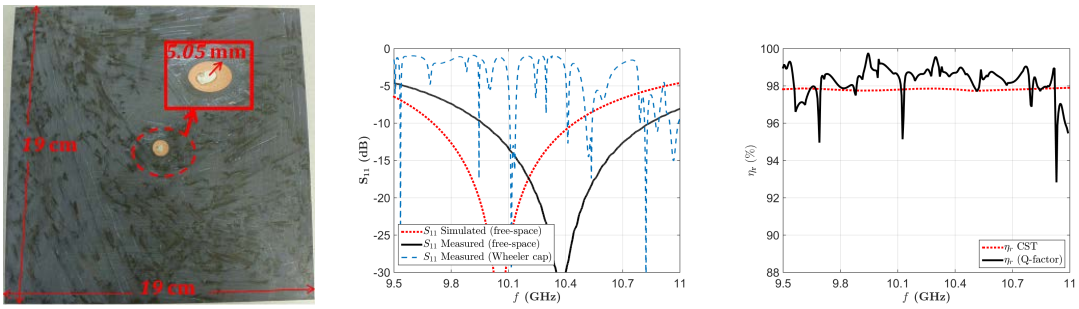

(a) (b) (c)

Figure 4.19: The structure and measured results for a circular patch antenna. (a) Antenna structure. (b) Computed and measured reflection coefficient. (c) Computed and predicted radiation efficiency.

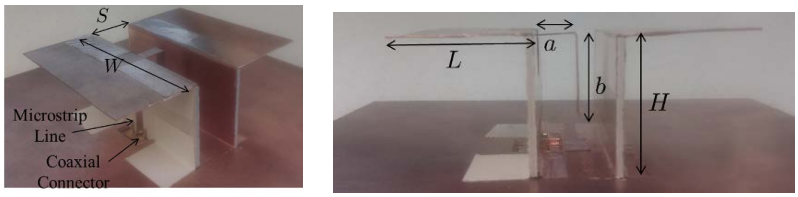

(a) (b)

Figure 4.20: The linearly polarized wide band antenna [95]. (a) Prospective view. (b) Side view.

mm, $a = 10.4$ mm, and $S = 17$ mm. The processed radiation efficiency results by the Q-factor method, the IWC and MWC are shown in Fig. 4.21 using the 'Design 1' contacltess Wheeler cap. The presented results show expected high radiation efficiency as predicted using the Q-factor method, which has the radiating elements made from copper. It is interesting to notice that the IWC method fails to accurately predict the antenna efficiency performance because it is highly susceptible to the dense presence of cavity modes, which is a typical case in the used Wheeler cap as predicted in Appendix A.

4.5.2 Antennas with Solar Cells

To test the proposed setup with antennas mounted over solar cells, three antenna structures are tested. The first antenna is a monopole of 11 mm length as shown in

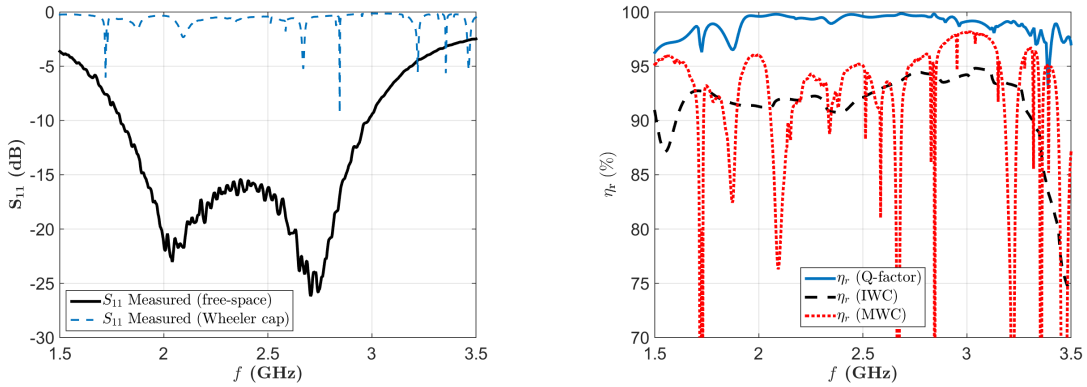

(a) (b)

Figure 4.21: The measured and processed results for linearly polarized wide band antenna. (a) Measured reflection coefficients. (b) Predicted radiation efficiency compared with other post-processing techniques.

Fig. 4.22 (a). The computed and measured reflection coefficients in free-space are shown Fig. 4.22 (b) indicating insignificant changes due to the presence of solar cells compared to the case with the aluminum ground plane. However, the predicted radiation efficiency shows less than 3% deterioration of the radiation efficiency compared to the case with the aluminum ground plane as presented in Fig. 4.22 (c). This lines up with the findings in Chapter 3, which indicates low loss level in terms of surface impedance inside the solar cells structure.

The second test case exploits the U-shaped DRA as shown in Fig. 4.23 (a) with the same details and dimensions employed in Appendix A.3. The measured reflection coefficient indicates a slight difference according to the ground plane type as presented in Fig. 4.23 (b). Moreover, the measured radiation efficiency in Fig. 4.23 (c) shows minor changes that can be considered within the proposed procedure tolerance level ($\sim 2\%$). However, it is important to notice that the measurement results do not show any polarization dependent performance according to the orientation of the antenna E-plane with the solar cells conducting lattice (parallel $\parallel$ and perpendicular $\perp$) as shown in Figs. 4.23 (b) and 4.23 (c).

Furthermore, the wideband circular stacked DRA is used as a test case for the

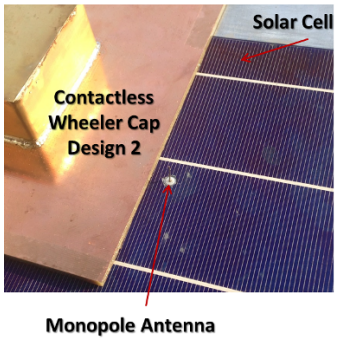

(a)

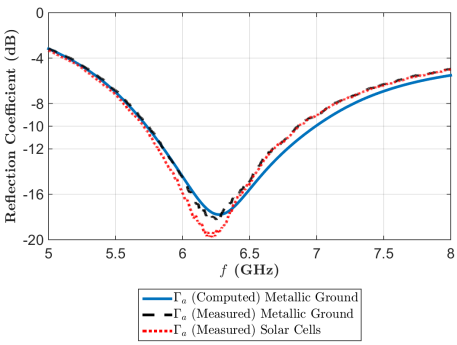

(b)

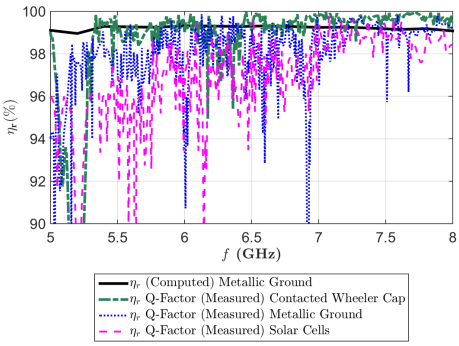

(c)

Figure 4.22: The structure and measured results for a monopole antenna mounted over solar cells. (a) Antenna structure. (b) The computed and measured reflection coefficients in free-space. (c) Computed and predicted radiation efficiency for different scenarios.

proposed study as shown in Fig. 4.24 (a). The dimensions of the employed antenna are the same as the presented antenna in Appendix A.4. The measured reflection coefficients indicate differences according to the ground plane type as shown in Fig. 4.24 (b) in a similar way as the previous case. Also, the predicted radiation efficiency shows minor deterioration ($\sim 2\%$) within the dielectric resonator broadside radiation frequency band as introduced in Fig. 4.24 (c). However, at the end of the measured frequency band ($\sim$ 15 GHz), a monopole-like radiation type mode is present, which suffers from around 4% percentage points deterioration in the measured radiation efficiency.

The presented test cases indicate that DRAs integrated with solar cells are less

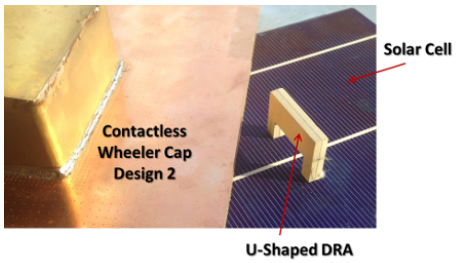

(a)

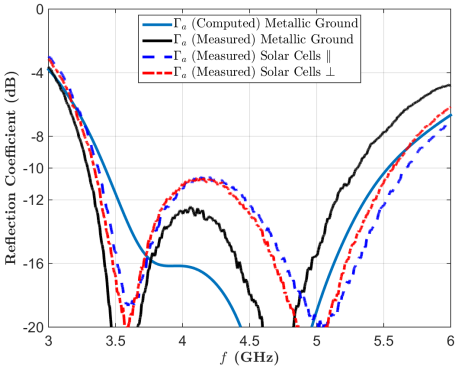

(b)

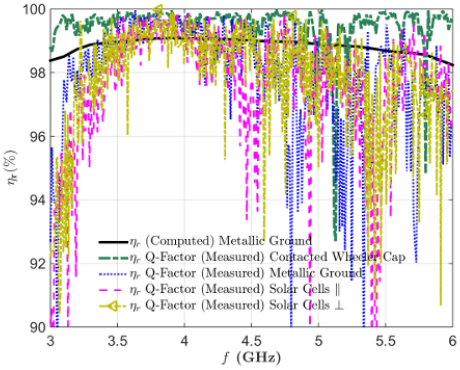

(c)

Figure 4.23: The structure and measured results for a U-shaped DRA mounted over solar cells. (a) Antenna structure. (b) The computed and measured reflection coefficients in free-space. (c) Computed and predicted radiation efficiency for different scenarios.

affected by the solar cells in their broadside radiation modes. This results line up with the findings in [96], which indicate that dielectric resonator antennas are not affected much by the triple junctions of the solar cells. Also, monopole type radiation antennas are subjected to more interaction with the solar cells structure, which results in consumption of the radiated power in the solar cell body. Therefore, one may think of DRAs as one of the best alternatives for integration with solar cells as their associated broadside radiation modes do not interact with the solar cells ground plane. One can also predict that using DRA with smaller footprint on the solar cell shall not cause too much blockage of light.

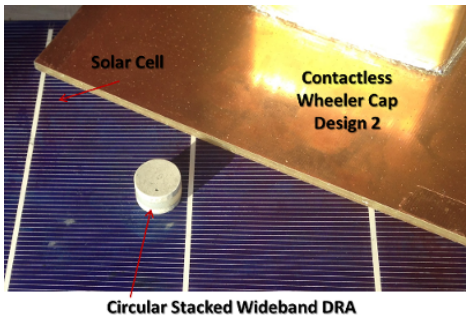

(a)

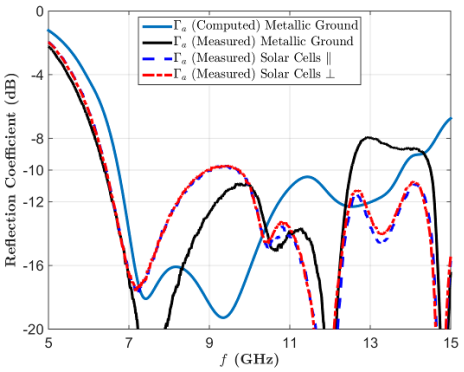

(b)

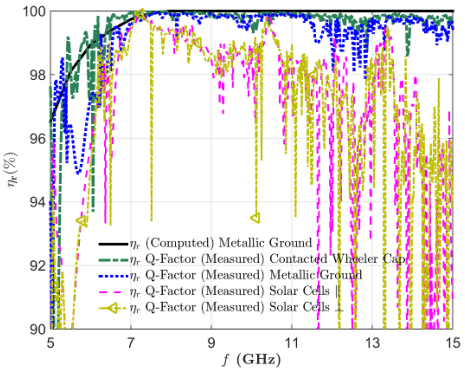

(c)

Figure 4.24: The structure and measured results for the wideband circular stacked DRA mounted over solar cells. (a) Antenna structure. (b) The computed and measured reflection coefficients in free-space. (c) Computed and predicted radiation efficiency for different scenarios.

4.6 Summary

A new design implementing the Wheeler cap concept was proposed to measure arbitrary moderate sized antenna radiation efficiency in a contactless fashion. This design concept has been proposed for the purpose of predicting the antenna radiation efficiency incorporating the antenna's large ground plane environment into the Wheeler cap's shielding structure, such as antennas over large substrates, oxidized metals and solar cells. The introduced design made use of evanescent wave guiding structures to provide the required EM shielding without requiring electric contacts between ground planes and the Wheeler cap. This was implemented using cascaded

and stacked mushroom-shaped EBG structures for wide band performance. A novel EBG unit cell has been presented through this work for compact design for the required shielding flanges. Two different contactless Wheeler caps were designed to cover the frequency band from 1.5 GHz to 40 GHz. Anticipation for the quality of measurements was conducted through measuring the quality factors of the cavity modes inside the presented contactless Wheeler cap designs. These measured quality factors exhibited relatively high values in most of the designed bandwidths indicating acceptable performance according to an error estimation criterion. The same principle was tested for solar cells ground planes showing a significant reduction in the quality factor values, which reduced the quality of measurements in this environment. Verification and measurement cases have been presented to validate the proposed designs and characterize different antennas mounted over solar cells.

Chapter 5

The Random Auxiliary Sources Method

5.1 Introduction

Upon developing a numerical solver for serving as a design tool for the presented work, a novel approach, inspired by the Method of Multiple Multipole (*MMP*)or the Generalized Mulipole Method (*GMP*) [97], is introduced to allow for easier adaptation to the studied problems. This technique, through its projected fast, simple, and flexible formulation and implementation, can be used for solving antennas and scattering problems with anisotropic surface impedance boundaries. This type of problems has very limited coverage by the commercially available software. Also, it can be used to model radiating antennas in both the near and far field regions, which can be used for the reflectarray design procedure.

The GMP method was introduced in the eighties by Hafner [97] with promises to be a faster technique than MoM. It has been proved that equivalent problems with sources away from the surface of the objects can be used to accurately solve EM scattering problems [98]. Several independent groups contributed to this method [99]

providing suggested positions for point matching and source placement for optimal accuracy of the solution. The suggested optimal placement of the sources is uniform and away from the surface of the object. Moreover, the method features simple solutions to problems avoiding singularity extraction. In addition, the solution stability of the problem of using the GMP has been studied in [100]. Inaccuracy in the provided solutions using the MMP method for complicated problems has been treated using the singular value decomposition. This eliminates the unnecessary testing points along with redundant sources. However, this adds more overhead to solve the problem.

In the various implementations of the GMP procedure, the 2D problem has been studied extensively starting with [101]. An optimization for the sources' positions in the solution domain has been performed in [102] with adaptation to structures with wedges. This is done by placing sources very close to edges to simulate the singular behavior of the fields at the edges. The performance of this technique has been studied in [103] for the required number of unknowns and contour choice. The study concluded that this method is efficient for small objects and not reliable for large objects. Also, in [104], it has been concluded that the optimum choice of the sources' contour for best accuracy in boundary conditions satisfaction is not necessarily the most economical choice for the number of unknowns and consequently execution time in comparison to MoM.

Inspired by the latter approach, modeling antennas using a small numbers of dipoles through matching near fields has succeeded with a very good accuracy via a means of binary genetic algorithm optimization [105]. This is because the dipoles' position, orientation, and moment amplitude are treated as degrees of freedom, which in turn allows the dipoles to represent the antenna's characteristic modes. Other optimization procedures were used for the same purpose namely: particle swarm optimization [106] and quantum particle swarm optimization [107]. However, all of these methods are very time consuming due to the need for numerical optimization,

which requires many iterations. Nevertheless, these optimizations proved that solutions for EM open problems can accurately exist without following the "optimum" source placement procedure proposed in the GMP procedure.

In this chapter, the concept of random equivalent problems is presented using a small number of randomly distributed infinitesimal dipoles to solve arbitrary 3D EM scattering problems. The unknowns involve the complex amplitude and polarization of the dipoles, while the positions are presumed to be randomly distributed in a controlled pre-specified domain for the equivalent problem(s). The use of a wider range of degrees of freedom has an implication on the required number of unknowns (i.e. A smaller number of unknowns are required to solve problems when compared to other surface equivalent based codes). Since the proposed RAS method features randomly positioned dipoles, the solution parameters are selected based on statistical analysis to guarantee acceptable solutions in terms of accuracy and speed. Also, the solution stability due to the possibility of having redundant dipoles is addressed to keep a qualitative measure of possible sources of numerical noise due to linear dependency of equations. Then, a novel and general purpose edge correction technique based on the same approach is investigated to enable the proposed technique to cover a wide range of applications involving edges. It should be stated that the proposed method is inspired by the GMP method, thus a performance comparison between the two methods is performed to indicate the merit of the proposed technique over its predecessor. In addition, the complexity of the proposed method is qualitatively discussed to classify it within the spectrum of numerical solvers. The proposed technique is verified and compared to analytical solutions for canonical problems along with the commercially available integral equation solver of CST [108] for different shapes and combinations as presented in Appendix B.

In addition to scattering problems, the proposed RAS method is extended to model arbitrary antennas by matching their near fields resulting from any full-wave

analysis package. Although this problem has been studied in [105–107], the proposed procedure is expected to develop models faster. Furthermore, the proposed method is applied to reflectarray design procedure by modeling feed antennas. The capabilities of the proposed method is enhanced by introducing the multiple reflections concept to accurately predict reflectarrays' radiation patterns including the forward scattering of the feed antenna [109, 110].

5.2 Problem Formulation

The electromagnetic scattering problem from an arbitrarily shaped object is demonstrated in Fig. 5.1 (a). A homogeneous scatterer is illuminated by a uniform plane wave that exhibits oblique incidence with respect to the coordinate system with angles α^i, θ^i, and ϕ^i. The angle α^i is the polarization angle of the incident electric field with the plane of incident (to incorporate all the possible wave polarization), θ^i and φ^i are the spherical coordinates of the elevation and the azimuthal angle of the incident plane wave, respectively [56]. Alternatively, point sources can be simply involved in the formulation using the expressions in [111].

The proposed external equivalent problem exploits a set of randomly distributed infinitesimal dipoles of arbitrary orientation, where the unknowns are their complex amplitudes, as shown in Fig. 5.1 (b). These dipoles are generated, in a three dimensional pre-controlled space, with a uniform distribution within the scatterer's bound. Moreover, each dipole type (electric or magnetic) is selected randomly for further liberation of all possible degrees of freedom making the solution procedure independent of problem geometry and/or excitation types. However, problems with unknown internal fields require an internal equivalent problem that is used along with the external problem to obtain the solution. There, random sources with the same features of the external problem are used, but they are placed randomly outside the scatterer

and within a controlled large boundary as shown in Fig. 5.1 (c) with A arbitrarily chosen to be larger than triple of the maximum dimension of the scatterer.

Based on the uniqueness theorem [111], the unique solution of the EM problem is obtained by satisfying the original problem's boundary conditions. In a general sense, the boundary conditions between any two media can be written in the form

$$\begin{pmatrix} \mathbf{E}(\mathbf{r}) \\ \mathbf{H}(\mathbf{r}) \end{pmatrix}_t^i + \begin{pmatrix} \mathbf{E}(\mathbf{r}) \\ \mathbf{H}(\mathbf{r}) \end{pmatrix}_t^s = \begin{pmatrix} \mathbf{E}(\mathbf{r}) \\ \mathbf{H}(\mathbf{r}) \end{pmatrix}_t^d ; \; on\, S \tag{5.1}$$

where $\mathbf{E}(\mathbf{r})$ and $\mathbf{H}(\mathbf{r})$ denote electric and magnetic field, respectively, $\mathbf{r}$ is any point in space in the equivalent problem's validity region [111], the subscript t denotes the tangential components to the surfaces S, and the superscripts i, s, and d are abbreviations for incident, scattered, and diffracted, respectively. Consequently, an iterative approach is invoked to evaluate the unknowns of the problems with the contributions expressed as

$$\begin{pmatrix} \mathbf{E}(\mathbf{r}) \\ \mathbf{H}(\mathbf{r}) \end{pmatrix}^{s(d)} = \sum_{j=1}^{N_I} \sum_{n=1}^{N_{g,j}^{e(i)}} \begin{pmatrix} a_{j,n}^{e(i),x} \begin{pmatrix} \mathbf{E}(\mathbf{r'}_n,\mathbf{r}) \\ \mathbf{H}(\mathbf{r'}_n,\mathbf{r}) \end{pmatrix}^{I_x(M_x)} + \\ a_{j,n}^{e(i),y} \begin{pmatrix} \mathbf{E}(\mathbf{r'}_n,\mathbf{r}) \\ \mathbf{H}(\mathbf{r'}_n,\mathbf{r}) \end{pmatrix}^{I_y(M_y)} + \\ a_{j,n}^{e(i),z} \begin{pmatrix} \mathbf{E}(\mathbf{r'}_n,\mathbf{r}) \\ \mathbf{H}(\mathbf{r'}_n,\mathbf{r}) \end{pmatrix}^{I_z(M_z)} \end{pmatrix} \tag{5.2}$$

where N_I is the number of iterations, $N_{g,j}^{e(i)}$ is the number of sources ($N_g^{e(i)}$) at iteration j for the external (internal) equivalent problem, $a_{j,n}^{e(i),v}$ is the unknown complex amplitude of the infinitesimal dipole n in the v polarization for the external (internal) problem, $\mathbf{E}^{I_v(M_v)}$ and $\mathbf{H}^{I_v(M_v)}$ are the electric and magnetic fields of a unit moment electric (magnetic) dipole in the v polarization, respectively, and $\mathbf{r'}_n$ is the nth source position vector. An over-determined system of equations is then formulated for the problem as $N_{g,j}^{e(i)} \ll M$, where M is the number of testing points that are chosen uniformly or non-uniformly over S to test boundary condition(s) satisfaction. The

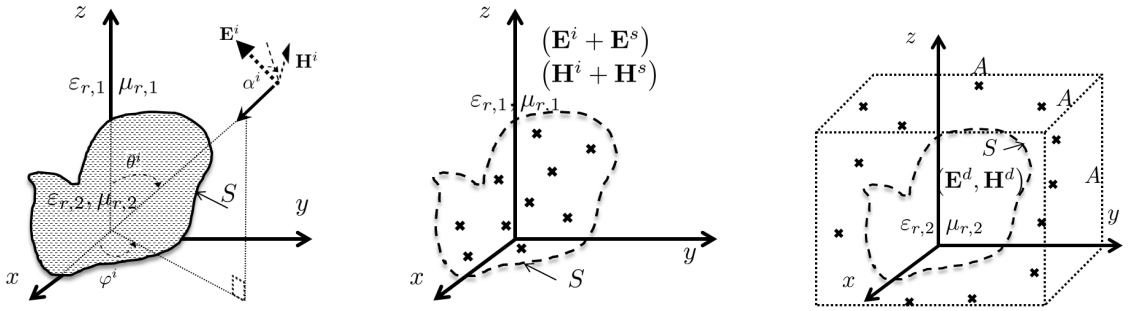

Figure 5.1: The electromagnetic scattering problem illustration [112] ©2015 IEEE. (a) Original problem. (b) External equivalent problem proposing random sources within the scatterers' region. (c) Internal equivalent problem featuring random sources in a controlled domain outside the scatterers' region.

following describes the employed solution procedures for single and multiple scattering objects and the exploited acceleration techniques.

5.2.1 RAS Solution Procedure

The solution procedure of the proposed techniques follows the previously introduced approach for 2D problems for the different boundary conditions [113–115] with a pre-specified error tolerance criterion. The main difference between the 2D version and the current 3D version is the positioning scheme for infinitesimal dipole sources in a volume compared to an area in the 2D version. The sources may be of electric type, or magnetic type, or their combinations, even if the scatterer is conducting type or dielectric type. The main procedure for the proposed RAS method used for all boundary conditions can be used exactly as the 2D solution procedure presented in the flow chart shown in Fig. 5.2.

For each iteration, the unknowns in Eq.(5.2) are obtained through enforcing the boundary condition in Eq.(5.1) on the surface S. An over-determined matrix equation is formulated using a number of sources significantly less than the observation points

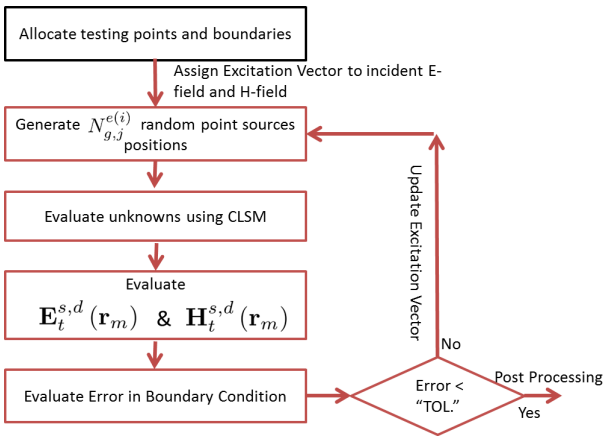

Figure 5.2: The proposed RAS method solution procedure for a 3D EM scattering problem [115] ©2015 IEEE.

M on the surface as

$$\begin{bmatrix} \mathbf{E}_t^s(\mathbf{r}_m) - \mathbf{E}_t^d(\mathbf{r}_m) \\ \eta\left(\mathbf{H}_t^s(\mathbf{r}_m) - \mathbf{H}_t^d(\mathbf{r}_m)\right) \end{bmatrix} = \underline{\mathbf{Z}}^j \left[\dots a_{j,n}^{e(i),x} \dots a_{j,n}^{e(i),y} \dots a_{j,n}^{e(i),z} \dots \right]^T = - \begin{bmatrix} \mathbf{E}_t^j(\mathbf{r}_m) \\ \eta\mathbf{H}_t^j(\mathbf{r}_m) \end{bmatrix}; \quad \begin{matrix} m = 1, 2, \cdots, M \\ n = 1, 2, \cdots, (N_{g,j}^e + N_{g,j}^i) \end{matrix} \tag{5.3}$$

where $\mathbf{E}^j$ and $\mathbf{H}^j$ are the parts of the excitation vector to the problem at iteration j (they are the incident fields in the first iteration only), η is the intrinsic impedance of the external equivalent problem medium, The superscript T denotes vector transposition, $\underline{\mathbf{Z}}^j$ is the problem matrix at the jth iteration, and $\mathbf{r}_m$ is the mth testing point position vector. The unknowns of this equation are computed via the use of the CLSM for a minimum square error in the boundary conditions as

$$Error(\%) = 100 \times \frac{\left\| (\mathbf{E},\mathbf{H})_t^i + (\mathbf{E},\mathbf{H})_t^s - (\mathbf{E},\mathbf{H})_t^d \right\|_2^2}{\left\| (\mathbf{E},\mathbf{H})_t^i \right\|_2^2} \tag{5.4}$$

according to the problem type with $\|\|_2$ denotes the norm-2 value of a vector.

The iterative solver is developed to make use of all obtained solutions, even if

they are not satisfactory w.r.t. the required tolerance in the boundary condition. As shown in flowchart in Fig. 5.2 , the excitation vector in Eq. (5.3) is updated after each iteration to incorporate previous solutions in the current solution to go viz

$$\begin{bmatrix} \mathbf{E}_t^j \\ \mathbf{H}_t^j \end{bmatrix} = \begin{bmatrix} \mathbf{E}_t^i + \mathbf{E}_t^s|_{1,\cdots,j-1} - \mathbf{E}_t^d|_{1,\cdots,j-1} \\ \mathbf{H}_t^i + \mathbf{H}_t^s|_{1,\cdots,j-1} - \mathbf{H}_t^d|_{1,\cdots,j-1} \end{bmatrix} \tag{5.5}$$

until the desired accuracy is reached.

It is essential to elaborate on the different usages of the right hand side in Eq. (5.3). As mentioned before for the first iteration, this vector represents the excitation vector. Other RAS iterations are required only to correct whatever missed in the boundary condition satisfaction in the first iteration, thus the already computed scattered and diffracted fields from previous iteration(s) are moved to the right side making it represent the error exist from the previous iteration(s). Iterations here are required to improve solutions gradually, not to search for the single shot solution. That means we are adding extra sources, which in turn increase the overhead of calculating the scattered fields as the number of sources increases.

An important practical issue regarding using the proposed method for large problems or even with nonuniform sampling of the testing points is to weight the fields evaluated in Eq. (5.3) by an area. This is considered as using an approximated pulse by the middle point testing function instead of pure testing points. The reason behind this is to avoid any inconsistency between points in terms of the forced error tolerance. Therefore, a more practical way is to use $\mathbf{E}_t(\mathbf{r}_m)\cdot\mathbf{A_m}$ instead of just $\mathbf{E}_t(\mathbf{r}_m)$ in Eq. (5.3).

5.2.2 Method Acceleration

In the proposed method, the bottleneck in the employed computations is the RAS matrix filling. Therefore, a step to accelerate the proposed technique is to avoid

re-evaluating the matrix as used in the iteration method. A proposed solution is to reuse allocated infinitesimal sources in previous iterations to re-tune their moments to further reduce the error. In other words, accelerated iterations, where the procedure uses pre-determined sources sets to re-tune their dipole moments. Here, the procedure does not need to evaluate RAS matrices; it only evaluates the varying right hand side vector as presented in Eq. (5.5). This type of iteration does not add an overhead to post-processing and it is faster to process. Of course, to use accelerated iterations, several normal iterations may have to be processed.

In order to further explain the proposed technique, we can consider an example of a PEC scatterer, where the boundary condition is $\mathbf{E}_t^s(\mathbf{r}) + \mathbf{E}_t^i(\mathbf{r}) = \mathbf{0}$ on the outer surface of the scatterer. The RAS solver can be set to use only 3 normal iterations and the rest should be accelerated iterations, if necessary, till the boundary condition is satisfied within the specified tolerance. Of course, any other number of normal iterations can be set into the procedure (not just three as indicated in the following example). It only has to be more than one iteration. The procedure can be described as follows:

1. In the first iteration, a new set of sources' positions and types are introduced by the random number generator function and mapped to fit the problem requirement. These sources are incorporated into the RAS procedure presented in [115] solving the boundary condition $\mathbf{E}_t^{s,1}(\mathbf{r}) = -\mathbf{E}_t^i(\mathbf{r})$, where $\mathbf{E}_t^{s,1}(\mathbf{r})$ is the scattered tangential electric field due to sources proposed in iteration 1.

2. If the boundary condition error does not satisfy the specified tolerance, a second iteration is performed by introducing another random set of sources. This new set is required to improve the boundary condition satisfaction by producing a scattered field to cancel the error found in iteration 1 as $\mathbf{E}_t^{s,2}(\mathbf{r}) = -\mathbf{E}_t^i(\mathbf{r}) - \mathbf{E}_t^{s,1}(\mathbf{r})$.

3. The process continues, if necessary, through normal iteration 3.

4. The accelerated iteration starts from 4 as pre-specified. The procedure here uses the same sources positions introduced in iteration 1. Therefore, the RAS matrix evaluation and decomposition is not required. Only the excitation vector is required to be evaluated as $\mathbf{E}_t^{s,4}(\mathbf{r}) = -\mathbf{E}_t^i(\mathbf{r}) - \mathbf{E}_t^{s,1}(\mathbf{r}) - \mathbf{E}_t^{s,2}(\mathbf{r}) - \mathbf{E}_t^{s,3}(\mathbf{r})$.

5. The process continues till the specified error tolerance in the boundary condition is met (using the predefined sources sets in normal iterations 2, 3, 1 ... etc.).

Typically, using only one iteration with this method is not recommended as the presumed sources' positions are not subjected to any change. For one set of sources with positions determined randomly through the procedure, the least square error solution is obtained through the CLSM procedure. There is no better solution for this sources' positions as all the remaining unknowns have linear dependency. Adding other set(s) with the solutions to the problem alters the pre-conditions of first set. Therefore, re-tuning the first set, and other set(s) consequently results in non-trivial solutions.

5.2.3 Iterative Field Bouncing Approach

Given the simplicity of formulation of the proposed RAS method, the 3D solution procedure can be extended to incorporate the EM scattering from multi-object problems in a similar approach to the 2D version presented in [115, 116] using the IFB concept.

The problem statement is illustrated in Fig. 5.3 (a) for two scatterers just for simplicity. The external equivalent problems for each scatterer can be shown in Fig. 5.3 (b) assigning two different random sources groups for each scatterer (P_1 and P_2). The boundary condition of this problem can be rewritten as Eq. (5.1) for each

scatterer 'l' in the form

$$\begin{pmatrix} \mathbf{E}_t^i(\mathbf{r}) \\ \mathbf{H}_t^i(\mathbf{r}) \end{pmatrix} + \begin{pmatrix} \mathbf{E}_t^s(\mathbf{r}; P_l) \\ \mathbf{H}_t^s(\mathbf{r}; P_l) \end{pmatrix} + \begin{pmatrix} \mathbf{E}_t^b(\mathbf{r}) \\ \mathbf{H}_t^b(\mathbf{r}) \end{pmatrix} = \begin{pmatrix} \mathbf{E}_t^d(\mathbf{r}) \\ \mathbf{H}_t^d(\mathbf{r}) \end{pmatrix}; \; on \, S_l \tag{5.6}$$

splitting the scattered fields on each scatterer 'O_l' into two parts: one part related to the assigned sources group P_l and the other is related to other sources groups. That part is called the bouncing fields that is evaluated as

$$\begin{pmatrix} \mathbf{E}_t^b(\mathbf{r}) \\ \mathbf{H}_t^b(\mathbf{r}) \end{pmatrix} = \sum_{\substack{j=1 \\ j \neq l}}^{N_o} \begin{pmatrix} \mathbf{E}_t^s(\mathbf{r}; P_j) \\ \mathbf{H}_t^s(\mathbf{r}; P_j) \end{pmatrix}; \; on \, S_l \tag{5.7}$$

with N_o is the number of objects. An iterative solution is invoked to solve the above problem minimizing the computational cost following the flowchart shown in Fig. 5.4. The iterations terminate upon reaching a pre-specified error tolerance in the bouncing fields update (ξ^q) at IFB iteration 'q'. It is required to reach a negligible contribution of the bouncing fields as

$$\xi_l^q(\%) = 100 \times \frac{\left\| (\mathbf{E}, \mathbf{H})_t^{b,q} \right\|_2^2}{\left\| (\mathbf{E}, \mathbf{H})_t^i + (\mathbf{E}, \mathbf{H})_t^s + \sum_{u=1}^{q-1} (\mathbf{E}, \mathbf{H})_t^{b,u} - (\mathbf{E}, \mathbf{H})_t^d \right\|_2^2}; \; on \, S_l \tag{5.8}$$

for all the objects, where $(\mathbf{E}, \mathbf{H})_t^{b,u}$ is the bouncing tangential electric and magnetic fields at the IFB iteration 'u'.

A key acceleration technique that can be used with this procedure is to tune the already allocated infinitesimal dipole source from the RAS solutions. By using the stored decomposed matrices, an overhead of evaluating the excitation vector is only required to perform the IFB iterations in a similar way to the procedure followed in Sec. 5.2.2.

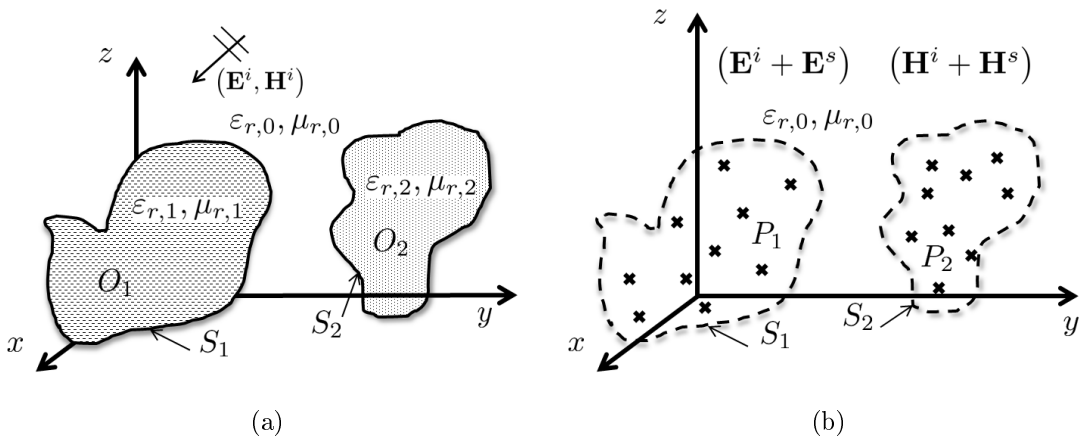

Figure 5.3: The EM scattering from multi-object problem illustration [112] ©2015 IEEE. (a) Original problem. (b) External equivalent problem featuring sources groups P_1 for object O_1 and P_2 for object O_2.

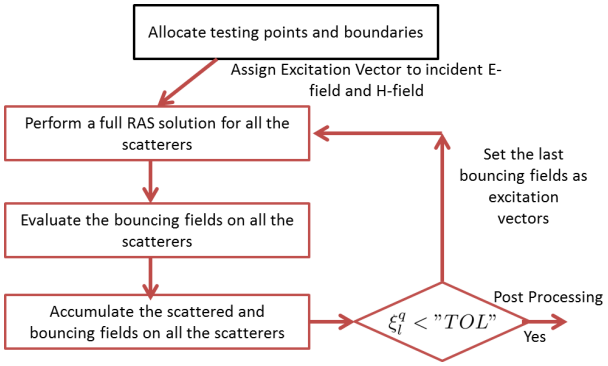

Figure 5.4: The proposed IFB solution procedure for a 3D EM scattering from multi-object problem [112] ©2015 IEEE.

5.3 Verification

A fundamental approach to verify the solution of the proposed RAS procedure is to observe the satisfaction of the boundary condition along the interface(s) between different regions. Alternatively, comparing the equivalent currents on the surface of a spherical PEC scatterer with Mie's series [111] gives a fair indication about the quality of the solution in the near field region, where it is more sensitive to small errors, see Fig. 5.5 (a). Moreover, in terms of comparing far fields, the scattering from a dielectric sphere is compared to the results of the commercially available integral solver software package CST. It is worth mentioning that the RAS procedure uses 25

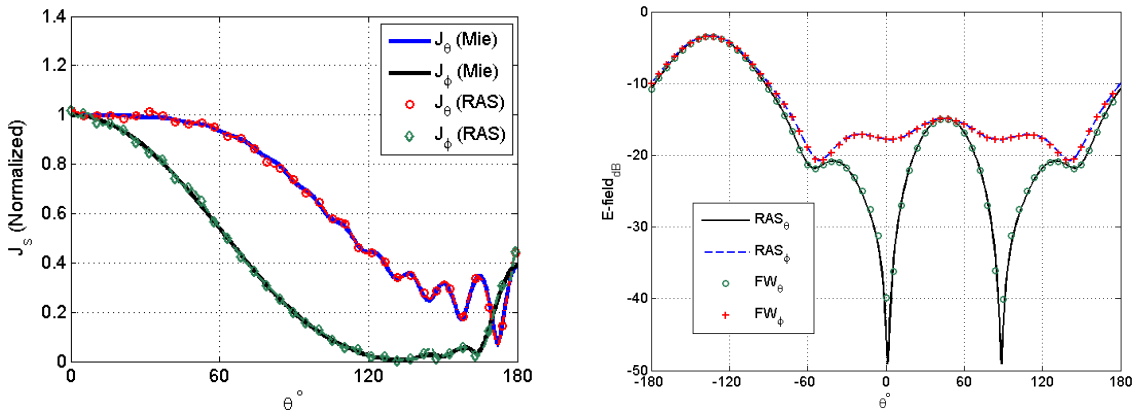

(a) (b)

Figure 5.5: Three dimensional electromagnetic scattering problems verification cases [112] ©2015 IEEE. (a) A comparison between the equivalent currents evaluated via Mie' series [111] and computed by the RAS method on a PEC sphere with radius $2.0\lambda_0$. (b) is the scattered far field from a sphere with radius $0.5\lambda_0$ and material with $\varepsilon_r = 20.0 - j1.0$ and $\mu_r = 1$. The sphere in (b) is illuminated by a uniform plane wave with angles α^i, θ^i, and ϕ^i are 45°,45°, and 0°.

testing points per square wavelength in the previous two examples, which is a very low rate for point matching technique in comparison to MoM [117]. Nevertheless, more verification and test results are presented in Appendix B including comparisons to the integral equations solver of CST.

5.4 Why Random?

One of the important steps in any numerical solution is the discretization of the object and the choice of the unknowns to determine their values. Here the distribution of source dipoles throughout the domain and observation points on the scatterer's surface are very important. It should be clear that any problem (original problem) has several possible equivalent problems. All of them will lead to a solution that can be considered a unique solution since they satisfy the boundary conditions of the original problem. If we understand physically each problem and the modes contributing to it, one can create a solution based on several sets of dipoles with each set representing

certain modes of the structure. Therefore, for a generalized problem with unknown modes contributions, it is not possible to a-priori define a distribution of dipoles that correspond to the contributing modes. Thus, arbitrarily oriented and randomly distributed sources must be used.

A study is presented here using a global optimization method to determine the dipoles positions within a PEC spherical scatterer with arbitrary excitation. The optimization is required to satisfy the boundary condition within a pre-specified error. It is important to differentiate between two types of variables in the study. The two variables are linear type and nonlinear type. Nonlinear variables are the dipole positions, which enter the problem through the expression for the field they produce. The other type is with linear dependencies, such as dipole moments and orientations. So, the goal of the optimization procedure is to determine the nonlinear variables, where the linear variables are evaluated accordingly using the Complex Least Square Method ($CLSM$) [85]. Fig. 5.6 shows a typical optimization case, where the scatterer is a PEC sphere with $ka = 2\pi$ excited by a uniform plane wave. Particle Swarm Optimization (PSO) [118] is used to determine the positions of the sources with the same kernel evaluations of the proposed RAS method. The cost function is the error in the boundary conditions, which is set to a maximum of 1.0E-3.

The results in Fig. 5.6 show that possible solutions to the problem can exist with a relatively small number of sources (~ 55 for this problem), but with multiple PSO iterations. It should be clear that each iteration is a new solution with the same number of sources, but with different position distributions and dipole moments. By increasing the number of sources (i.e. Increasing the degrees of freedom) the PSO converges with fewer iterations. When the number of sources is increased to more than one hundred, the PSO converges in ONE iteration, which means that no optimization has been performed to solve the problem. The initial random distribution of sources determined by the PSO manages to satisfy the required boundary condition tolerance.

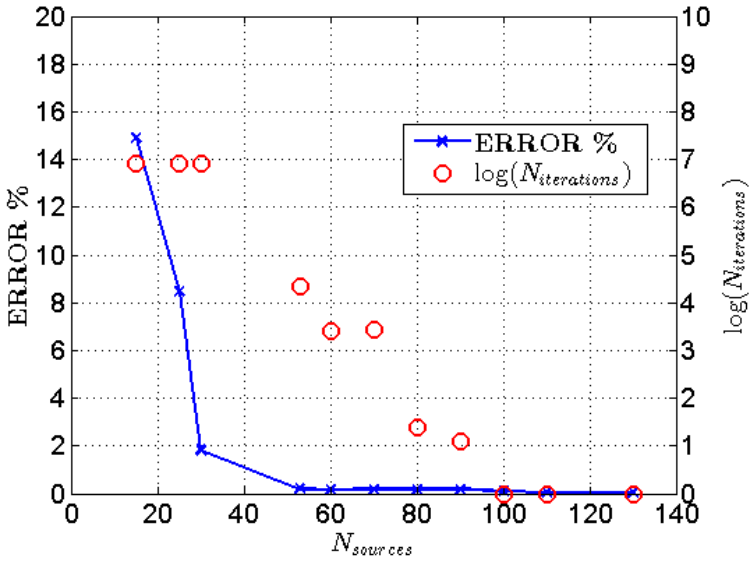

Figure 5.6: Particle swarm optimization best achieved error tolerance in the boundary condition and number of iterations results solving the scattering results from a PEC sphere [112] ©2015 IEEE.

This example clearly justifies the effectiveness of using the random distribution of sources to solve scattering problems.

It is important to demonstrate the difference between a PSO iteration and a RAS iteration. In PSO, an iteration involves several evaluations of the cost function with different randomly chosen sources' positions by the optimizer to serve as agent/particle for the PSO [118]. Updates to the sources' positions are then introduced by the optimizer according to the better direction(s) that satisfies the optimization goal. In contrast, the RAS procedure operates with a number of sources of the same order where PSO does not require optimization. Sources' positions are presumed randomly and boundary conditions are satisfied with a very high probability. The following section provides an empirical formula to determine the required number of arbitrary source for fast convergence of the RAS procedure.

5.5 Solution Stability and Limitations

Since the equivalent problem(s) of any general problem using the RAS procedure is proposed to be random, the stability and repeatability of solutions may be of concern. The following subsections provide an assessment for the proposed method.

5.5.1 Convergence of Solutions

A statistical analysis of the proposed technique is made for PEC conducting spheres to determine the optimum choice of the required parameters, in a similar approach as in [113, 114]. The choice of optimum number of sources per RAS iteration is based on optimizing the average execution time and required RAS iterations to satisfy the specified error tolerance. This comes up with an empirical formula to use directly for optimum performance in terms of speed and accuracy as

$$N_{g,j}^{e(i)} \sim \chi \frac{M}{\mathrm{SPW}^2} \tag{5.9}$$

where SPW is the specified linear sampling per wavelength for equally spaced testing points. The variable χ has an optimum value of 7.14 for smooth objects. The value can be increased to 9 for structures with sharp edges to allow more degrees of freedom to capture the fast variations in the boundary conditions. The presented results in Table 5.1 show that the average required number of RAS iterations (N_I) increases as the number of sources $N_{g,j}^{e}$ decreases. The execution time exhibits a convex behavior with the number of used sources indicating the optimum value presented in Eq. (5.9). Moreover, the main advantage of the provided formula is the independence of sampling density on the required degrees of freedom to solve the problem. It can be depicted that the required number of sources for the external and internal equivalent problems are only related to the surface area of the scatterer and the medium type. It is important to illustrate that the provided optimum number of sources by Eq.

Table 5.1: The effect of varying the number of introduced sources every RAS iteration on the solution performance for a PEC sphere of radius $1\lambda_0$. The used error tolerance for this problem is $< 0.1\%$. The results are considered for a sample space of 1000 runs for each case [112] ©2015 IEEE.

SPW	M	N_g^e	AVG. N_I	AVG. Time (s)
10	1299	162	1.2874	1.9694
		129	1.2275	1.254
		108	1.3174	0.992
		92	1.4611	0.8366
		81	1.5928	0.7488
		72	2.8144	1.0892
		64	5.1677	1.6756
5	332	162	1.1317	0.5958
		129	1.1557	0.3934
		108	1.1856	0.2731
		92	1.2036	0.2075
		80	1.6228	0.219
		72	2.5689	0.2865
		64	4.5808	0.4284

(5.9) complies with the region where the optimization method does not require many iterations to converge to the desired accuracy as seen in Sec. 5.4.

5.5.2 Linear Independence of Equations

Although the solution is based on using the least square method, the quality of the obtained solutions is affected by the independence of the used equations, similar to the GMP method in [100]. An intuitive idea is to investigate the effect of using random sources on the independence of the system of equations as a qualitative measure of the solution quality. The orthogonality of the contributions of the random sources is measured to distinguish the linear dependency of the equations. This can be determined by evaluating the generalized angle ψ between vectors (columns of the $\underline{\mathbf{Z}}$ matrix) in the n-dimensional space [100] viz

$$\psi = \cos^{-1} \frac{\langle \mathbf{u}_i, \mathbf{u}_j \rangle}{\|\mathbf{u}_i\|_2 \|\mathbf{u}_j\|_2} \tag{5.10}$$

Table 5.2: A comparison between different geometries and boundary conditions for the angles between different equations in each equation system [112] ©2015 IEEE.

Geometry	Material	$N_g^{e(i)}$	Probability of angles ψ		
			0°-50°	50°-70°	70°-90°
Sphere	PEC	92	0.0138	0.0538	0.9323
Sphere	Dielectric	183	0.0045	0.016	0.9794
Cylinder	PEC	71	0.0067	0.0287	0.9646
Cylinder	Dielectric	126	0.0059	0.0196	0.9744
Box	PEC	120	0.0025	0.0134	0.9841
Box	Dielectric	128	0.003	0.0123	0.9847

with $\mathbf{u}_{i,j}$ are different column vector in the $\mathbf{Z}$ matrix, $i \neq j$, $\langle\rangle$ denotes inner product of two vectors, and $\|\|_2$ is the norm-2 of a vector. The resulting angle is an indication of the dependency of these equations. Of course, a larger angle represents highly independent vectors (close to 90°) or that both sources contribute to the solution significantly. Also, a lower angle means that one of the sources does not contribute much to the solution; it might be a source of numerical noise in this case.

Typical results of the RAS technique are shown in Table 5.2. In the provided examples, the sphere has a radius of $1\lambda_0$, the cylinder has a radius of $0.5\lambda_0$ and a height of $1\lambda_0$, and the box has three equal dimensions of $1\lambda_0$. Through the results, it is of a very high probability to have angles between the vectors larger than 50° (i.e. The random sources contributions are mostly independent). However, it is worth mentioning that the provided results for angles between vectors in the RAS method are of the same order as the GMP technique when used to solve the same structures.

5.5.3 Edge Correction

Problems that involve scatterers with edges exhibit a slow convergence rate compared to smoothly curved structures unless special bases functions or special treatments are used. These solutions tend to saturate at certain high error values due to the lack of degrees of freedom necessary to solve the problem. The proposed solution is to introduce few random sources in the proximity of the edges to compensate for the fast

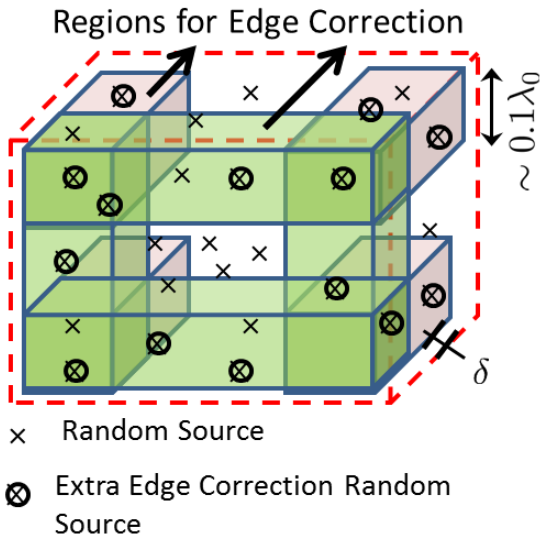

Figure 5.7: Regions to place extra random sources for edge correction [112] ©2015 IEEE.

variations in the boundary conditions as shown in Fig. 5.7 with $\delta \sim 0.01\lambda$ in a per wavelength basis ($D/\lambda \sim 8$) with D is the number of introduced near to edge sources. This process is suggested to start from the 2^{nd} or 3^{rd} iteration. This correction method is important for conducting bodies as well as high dielectric constant materials. An example that shows the impact of using this correction scheme is shown in Fig. 5.8. Accurate capturing of low scattering levels and features are improved by using this technique. Also, the implications of using the proposed technique on the solution performance are presented in Table 5.3. These results show the importance of using a suitable number of edge correction sources $D/\lambda \sim 8$ to compromise between accuracy and execution time. The evolution of the boundary condition error for the cases presented in Table 5.3 through iterations is presented in Fig. 5.9 clarifying the fact that the more edge correction sources are introduced, the faster the convergence.

The novelty of this edge correction procedure is in keeping the randomness concept effective. This ensures the convenience of the proposed solution method to any problem with similar features or with different excitation. Moreover, using any deterministic sources, in terms of position, as proposed in the 2D version of the MAS

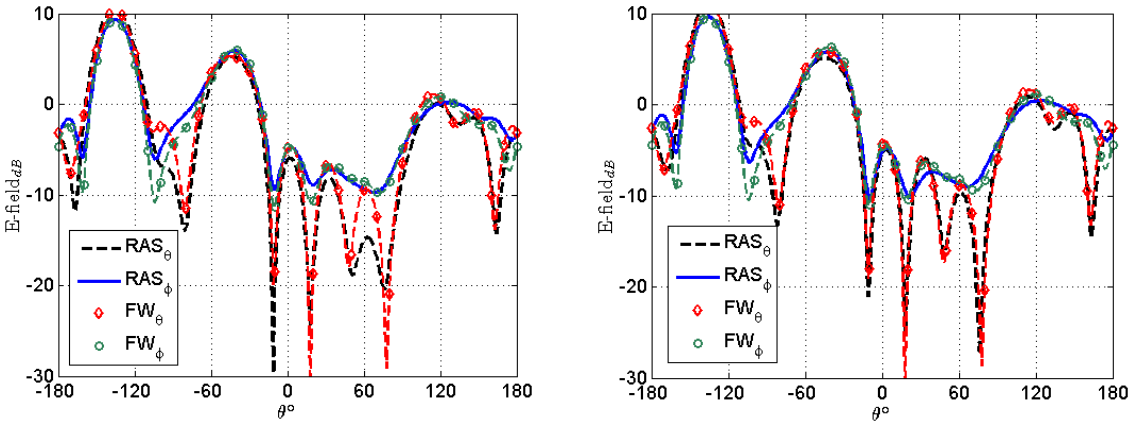

(a) (b)

Figure 5.8: The impact of using edge correction in the electromagnetic scattering problem on the scattered far electric field from a PEC hexahedron with dimensions $2\lambda_0 \times 2\lambda_0 \times 1\lambda_0$. It is illuminated by a uniform plane wave with angles α^i, θ^i, and ϕ^i are 45°,45°, and 0°. The observation plane is the plane $\phi = 0°$. The proposed *RAS* method results are compared to the full wave analysis (*FW*) of CST [112] ©2015 IEEE. (a) is the results without edge correction. (b) is the results with edge correction. The solution here used 8 unknown sets per wavelength.

technique [102, 119] does not provide a general purpose solution for the addressed problem. Placing sources very closely to the edges deteriorates the solution quality because the singularity level of the dipole fields is more severe than the 2D line sources. So, it is more adequate to provide freedom to the dipoles positions to keep good performance of the proposed RAS method.

5.5.4 Complexity Order of Operations

An important assessment figure of all numerical methods is the order of complexity of operations performed in the method. The proposed RAS method with the current simple implementation requires $O((N_g^{e(i)})^2 M/2)$ to assemble half the CLSM Hermitian matrix [115]. It also requires $O((N_g^{e(i)})^3/3)$ operations to obtain the solution using Cholesky decomposition technique [120] compared to $O((N_g^{e(i)})^3)$ if conventional LU decomposition is used [121]. It is important to notice that filling the matrix does not include integrals, which reduces the cost of each operation used in the matrix

Table 5.3: The performance of the proposed RAS method with the edge correction method. The structure under test has the same dimensions and excitation as the one used in Fig. 5.8. The chosen sampling per wavelength criterion SPW = 10 ($M = 2344$) [112] ©2015 IEEE.

χ	N_g^e	D/λ	Performance		
			#Itr.	time (s)	Error (%)
7.14	167	0	121	83.5	6.66
		2	121	104.8	3.11
		4	121	127.2	1.13
		6	47	90.9	0.9
		8	21	91.16	0.9
		10	15	109.9	0.9
9	213	0	121	107.2	6.62
		2	121	127.7	3.95
		4	121	149.5	1.8
		6	121	176.8	1
		8	28	106.7	0.9
		10	18	119.19	0.9

assembly compared to the MoM. Although the complexity figures are quite similar to that of conventional MoM, the reduction in required unknowns presented in this work pushes the crossover between the RAS method and the recent fast method, such as MLFMM, further from the MoM.

Accelerating the computations offered by the proposed RAS method requires tackling the most computationally expensive processes in the algorithm, which are the matrix filling and inversion. The basic idea is to reduce the number of executions of these processes. Reusing previously assigned random sources for other iterations to re-tune the evaluated dipole amplitudes accommodating the effect of other sources groups into calculations as presented in Sec. 5.2.2. This acceleration procedure is of high effect on the overall problem complexity for problems that requires a large number of iterations. Since, there is no need to re-evaluate RAS matrices, only the excitation vector is required to be evaluated with the order of $O(N_g^{e(i)}M)$. The unknowns can be evaluated using the stored decomposed matrix with the order of $O(N_g^{e(i)})$. However, the early iterations, where this technique is not in effect, suffer

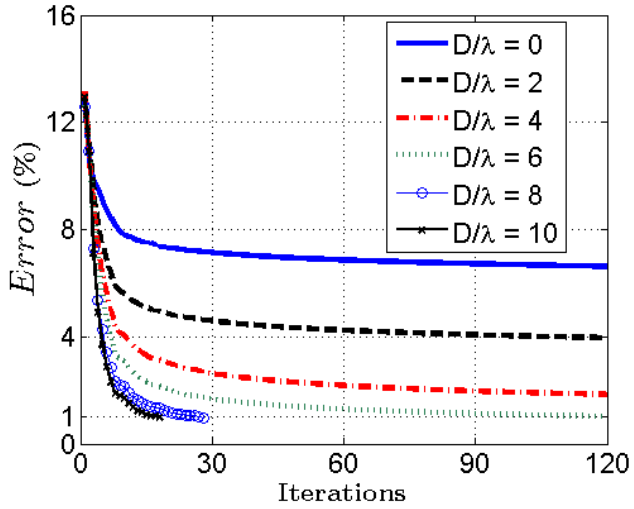

Figure 5.9: The error in the boundary condition satisfaction evolution through the proposed RAS iterations for the scattering from the box presented in Table 5.3 with $\chi = 9$ [112] ©2015 IEEE.

from an excessively large order of complexity.

Indeed, the current implementation of the procedure is comparable to MoM, However, there is a potential of using faster approaches for matrices assembling. One approach can be introduced by testing functions instead of testing points. This can reduce the required system of equations M, which reflects directly on the assembling time. Also, using approximation in filling the matrices can be of great help in reducing the computational cost of evaluating matrix elements similarly to MLFMM in a leveled approximation fashion. Furthermore, accelerating the matrix solution is an essential consideration for the asymptotic performance of the proposed procedure.

5.5.5 Memory Efficiency

For a problem with M testing points, RAS requires $N_g^{e(i)}$ number of arbitrarily oriented dipoles (according to Eq. (5.9)) that form a Hermitian matrix for the CLSM method that need $\sim 4.5(N_g^{e(i)})^2$ memory locations to store only half of the matrix for a general purpose problem. This is compared to $4M^2$ locations required by MoM. The same amount of memory is required to store the decomposed matrices, if required,

by both methods. The memory reduction ratio (ζ) of the overall RAS procedure to MoM can be expressed as

$$\zeta \sim N_I \frac{0.9\chi^2}{\mathrm{SPW}^4} \tag{5.11}$$

which is a small fraction following the bounds in Eq. (5.9) for χ and a relatively large number of N_I.

Alternatively, the obtained solutions in the MoM require $2M$ memory locations for a general purpose problem while RAS requires $3(N_I \times N_g^{e(i)})$. The ratio between the required memory for solutions may be comparable for a large value of N_I. However, N_I can be limited to have the total number of unknowns matches that of the MoM. Tuning the already obtained solutions for better accuracy is then invoked to reach the desired accuracy as with the acceleration advantages presented in the previous subsection.

5.5.6 Method Limitations

The RAS method is proposed to be a general purpose solver with the capability to solve piece wise homogeneous scattering problems. The method is formulated upon a similar concept to the surface equivalence principle, so it cannot be used to efficiently solve problems with high inhomogeneity. Moreover, the method is unsuitable to solve problems with zero thickness objects without some modifications by adding a phantom volume to the thin object to be part of the boundary. This is due to the need to have a volume by the scatterer to place the random sources within for the external equivalent problem without the need for singularity treatments.

5.6 Extension to Antenna Modeling Problems

Some antennas that their sources are located away from the surface can be treated as a scattering problem due to a spherical type of source with known fields. As such, the

plane wave fields are replaced with the source field and the procedure follows the same as introduced previously. Alternatively, for cases with sources attached to the antenna surface, a special treatment should be performed, which could be considered for future work. However, due to the availability of the commercial software, we are taking another direction in order to have an antenna replaced with a set of dipoles in a similar procedure to [105–107]. The RAS procedure can be used to model arbitrary antennas by matching the radiated near fields of antennas using available solutions obtained from commercial solvers. The developed models can be used for post-processing that is significantly fast compared to fully depending on commercial software packages. Instead of applying the boundary conditions to solve scattering problems as shown in Sec. 5.2, the radiated electric and magnetic fields on the surface of a box surrounding the antennas can be used as the excitation vector of the RAS procedure as shown in the equivalent problems in Fig. 5.10. This can be represented as

$$\sum_{j=1}^{L}\sum_{n=1}^{N}\mathcal{L}_{\binom{\mathcal{E}}{\mathcal{H}}}(\mathbf{I}_n^{j,J(M)}) = \begin{pmatrix} \mathbf{E}_t^r \\ \mathbf{H}_t^r \end{pmatrix} \; on\, S \tag{5.12}$$

where N is the number of the employed infinitesimal sources, L is the required number of iterations, j is the iteration number, $\mathcal{L}_{\mathcal{E}}$ and $\mathcal{L}_{\mathcal{H}}$ are linear operators to evaluate the electric and magnetic fields due to the proposed infinitesimal source $\mathbf{I}_n^{J(M)}$, respectively, and $\mathbf{E}_t^r$ and $\mathbf{H}_t^r$ are the tangential components of the radiated electric and magnetic fields vectors on the surrounding surface S. L iterations are used to solve the specified problem to a specific error tolerance in matching the near fields. The used infinitesimal sources ($\mathbf{I}_n^{J(M)}$) are allowed to arbitrarily contribute to all directions as

$$\mathbf{I}_n^{J(M)} = \hat{\mathbf{x}}\, a_n^x \delta(\mathbf{r}-\mathbf{r}') + \hat{\mathbf{y}}\, a_n^y \delta(\mathbf{r}-\mathbf{r}') + \hat{\mathbf{z}}\, a_n^z \delta(\mathbf{r}-\mathbf{r}') \tag{5.13}$$

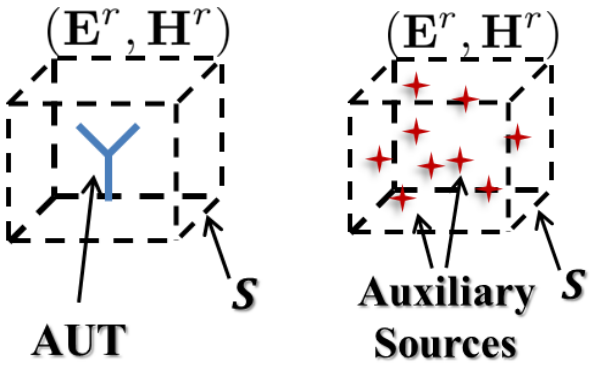

(a) (b)

Figure 5.10: Illustration of the modeling problem. (a) Original Problem. (b) Equivalent random problem.

where $I_n^{J(M)}$ is the nth infinitesimal source of electric(magnetic) type, a_n^v is the unknown complex amplitude in the v-direction, δ is the Delta Dirac function, and $\mathbf{r}'$ is source position, which is determined randomly with uniform distribution within the equivalent problem validity region.

The allowed degrees of freedom in this problem formulation are only the positions of the dipoles, which are presumed to be random according to RAS procedure philosophy. A valid solution domain can be the entire fields matching box, but restricting the solution domain to exactly the radiator dimensions solves the problem in less number of iterations. This can be due to the original radiating modes of antennas, which are originated from within the radiating element. Dipoles, which are located outside the radiating elements, negatively contribute in the projection procedure for the radiating modes; resulting in slower convergence for the procedure. They require other dipoles to cancel their negative contribution. This process requires several iterations to satisfy the pre-specified error tolerance.

An example to the antenna modeling by the RAS method can be presented for a conical horn antenna with geometry and dimensions shown in Fig. 5.11. The antenna near field ($\lambda_0/4$) away from the structure is matched with 100 RAS dipoles

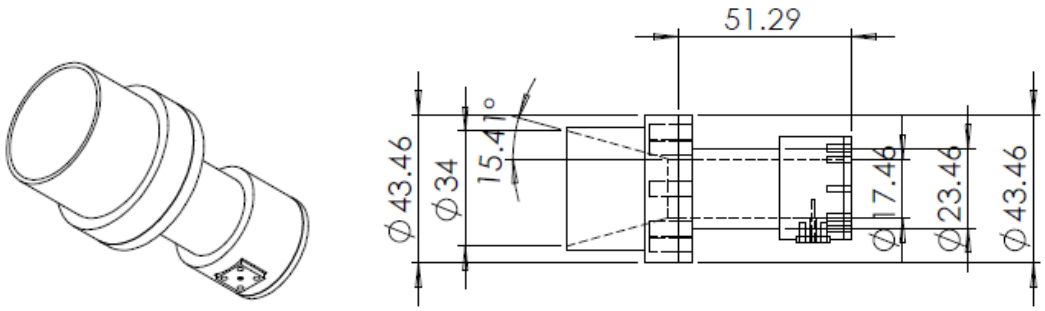

(a) (b)

Figure 5.11: A conical horn structure with all dimensions in millimeters. (a) Prospective view. (b) Side view.

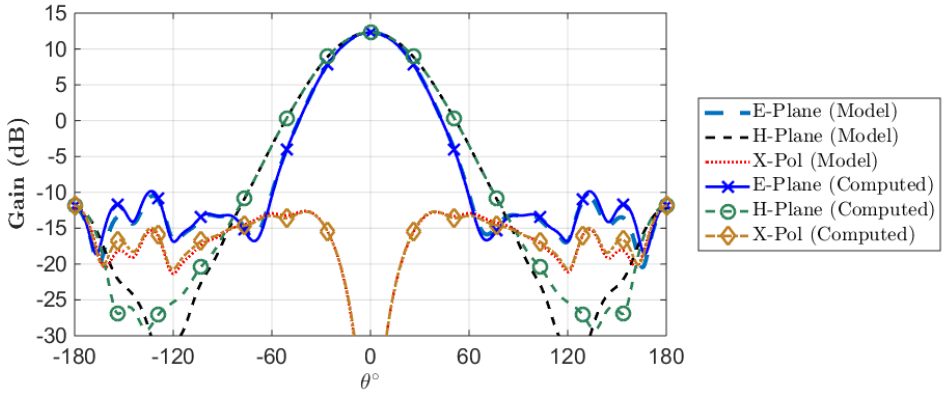

Figure 5.12: The antenna gain pattern comparison computed from the developed RAS model and the original CST model of the conical horn antenna shown in Fig. 5.11.

as explained in the procedure. The results are obtained in only one iteration satisfying the required error tolerance of 1%. The far field gain pattern comparison to CST is shown in Fig. 5.12 at 11.7 GHz for the standard E and H planes and the maximum cross polarization (X-pol) in the 45° plane cut using Ludwig III definition for cross polarization [122]. The radiation pattern results show very good agreement with the full-wave computations of CST.

In addition, the procedure can be used to model the scattering effect by any arbitrary antenna by matching the total fields on S. A modified version of Eq. (5.12)

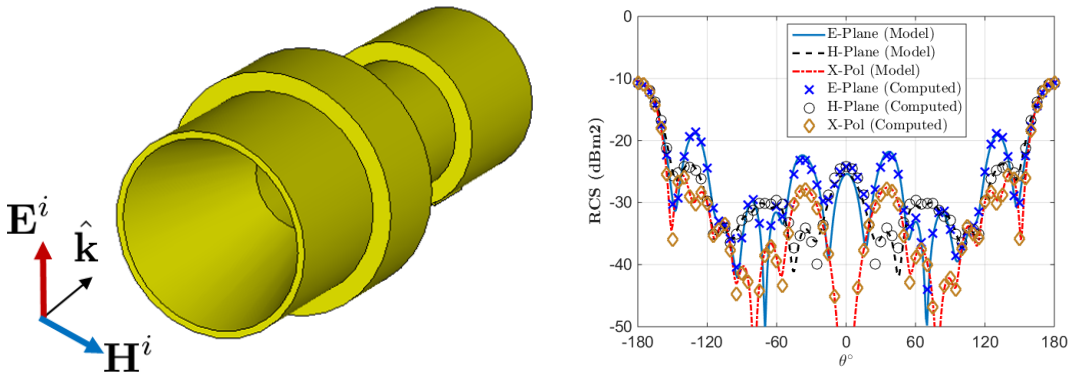

(a) (b)

Figure 5.13: The uniform plane wave scattering results of the conical horn shown in Fig. 5.11. (a) Conical horn structure showing the direction and polarization of the incident plane wave. (b) The scattering RCS.

can be written in the form

$$\sum_{j=1}^{L}\sum_{n=1}^{N}\mathcal{L}_{\left(\substack{\mathcal{E}\\\mathcal{H}}\right)}(\mathbf{I}_n^{j,J(M)}) + \begin{pmatrix}\mathbf{E}_t^i\\ \mathbf{H}_t^i\end{pmatrix} = \begin{pmatrix}\mathbf{E}_t^{tot}\\ \mathbf{H}_t^{tot}\end{pmatrix} \; on\, S \tag{5.14}$$

where the superscripts i and tot indicate incident and total, respectively. The results shown in Fig. 5.13 are for the Radar Cross Section (RCS) of the conical horn, shown in Fig. 5.11, when its port is matched. The plane wave polarization is chosen to be of the same polarization as the conical horn as shown in Fig. 5.13 (a). The RCS results show good agreement with the computed results from CST for the standard E and H planes and the cross polarization with minor differences around the back scattering direction.

5.7 Application to Reflectarray Design

The developed antenna models are used to approximately analyze reflectarrays. By using the antenna models of the feed antenna, fast and reasonably accurate reflectarray far fields results can be obtained in a similar analysis procedure as parabolic

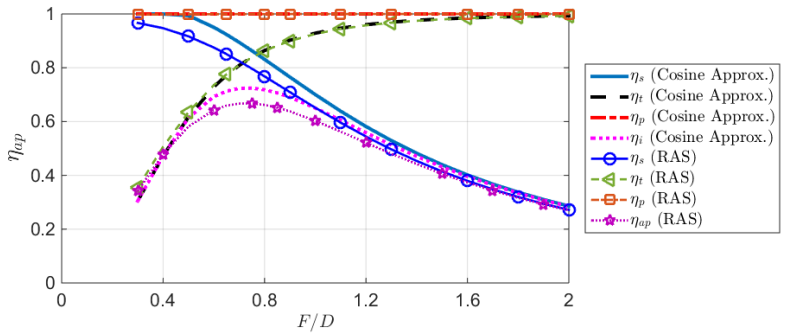

(a)

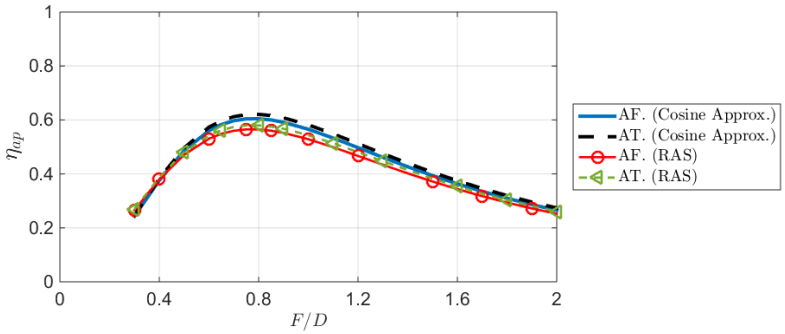

(b)

Figure 5.14: Aperture sub-efficiency components for the conical horn antenna shown in Fig. 5.11. (a) Sub-efficiency components. (b) Array theory (AT) and aperture field integration (AF) efficiencies and the theoretical aperture efficiency.

reflectors [123]. Moreover, this procedure is proposed to be implemented as a plug-in for full-wave solvers for fast reflectarray feed analysis.

5.7.1 Aperture Efficiency Prediction

The proposed antenna radiating model can be easily used to analyze reflectarray feed antennas using the analysis procedures provided in [124, 125]. Typically, cosine power approximation for reflectarray feed antennas is employed to analyze feeds [124, 125] in a similar way as parabolic reflectors [123]. However, this analysis procedure gives accurate results for well-designed feed antennas, where low side lobe levels are observed with negligible back lobe radiation. The results of this procedure become less accurate when bad feeds are used. Therefore, a more accurate approach is proposed

by using the RAS method as a simple tool to characterize reflectarray antenna feeds that works for conventional feeds and opens the door for non-conventional feed designs as presented in Sec. 6.2.

To verify the proposed method, the presented conical horn antenna in Fig. 5.11 is exploited as reflectarray feed antenna. The approximate cosine representation of the given radiation patterns of the conical horn antenna can be employed with values $q_e = 4.5$ and $q_h = 3.5$ as defined in [125]. A comparison between the computed aperture sub-efficiency components (i.e. spillover η_s, field tapering η_t and polarization η_p sub-efficiencies) and the total aperture efficiency $\eta_{ap} = \eta_s\eta_t\eta_p$ for different phase center separation distances F from a rectangular reflectarray with side dimension D is presented in Fig. 5.14 for the center feeding scenario. The RAS method results show more accurate representation of the sub-efficiency components; especially the spillover efficiency, which is not adequately governed by the cosine power approximation patterns. Also, the aperture field integration and array theory methods are employed to verify the proposed RAS models and show the RAS method predicts slightly less aperture efficiency value than cosine approximation patterns. Furthermore, the proposed method gives more accurate results with feeds that cannot be modeled with cosine approximations (i.e. low directivity or shaped beam feeds). It also gives accurate results for bad feeds (i.e. with high side lobe levels), which cannot be modeled with the cosine approximation.

5.7.2 Approximate Reflectarray Performance Via Multiple Reflections

Introducing the multiple reflections concept to the approximate analysis of reflectarrays proposed by the RAS method is done in a similar approach to [109, 110]. Having the radiating and scattering models for a reflectarray feed antenna can be used in conjugate with Physical Optics (PO) representations [111] to obtain more accurate far

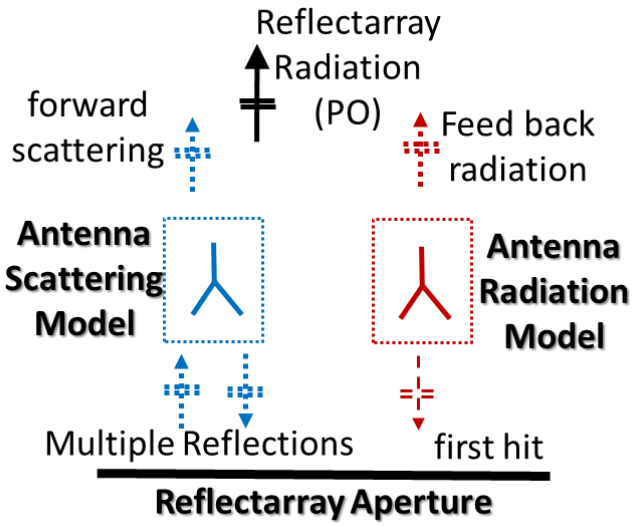

Figure 5.15: An illustration for the multiple reflections concept adapted to reflectarray performance estimation.

fields results than the array theory and aperture field integration methods presented in [124]. As shown in Fig. 5.15, the far fields of a reflectarray can be decomposed into different components in terms of electric field as

$$\mathbf{E}^{total} = \mathbf{E}^{r}_{f} + \sum_{m=1}^{\infty} \mathbf{E}^{PO}_{m} + \sum_{m=1}^{\infty} \mathbf{E}^{s}_{m} \tag{5.15}$$

where $\mathbf{E}^{r}_{f}$ is the back radiation contribution of the feed, $\mathbf{E}^{PO}_{m}$ is the back scattering from the reflectarray aperture computed by the PO due to the m^{th} field hit and $\mathbf{E}^{s}_{m}$ is the forward scattering of the feed antenna due to the m^{th} field hit.

The PO representation of the reflectarray back scattering assumes perfect phase compensation over the reflectarray aperture to the desired beam specifications using the unit cell periodic analysis information [124]. The procedure assumes only magnetic currents over the reflectarray aperture that is approximately computed by the knowledge of the incident field in the m^{th} hit as

$$\mathbf{M} = \left(\overleftrightarrow{\mathbf{\Gamma}} \cdot \mathbf{E}^{i}_{m} \right) \times \hat{\mathbf{n}} \tag{5.16}$$

where $\hat{\mathbf{n}}$ is the normal vector to the reflectarray aperture, $\mathbf{E}_m^i$ is the incident electric field at the m^{th} hit and the reflection coefficient dyad $\overleftrightarrow{\mathbf{\Gamma}}$ includes direct and cross coupling terms as

$$\overleftrightarrow{\mathbf{\Gamma}} = \begin{bmatrix} \Gamma_{xx} & \Gamma_{xy} \\ \Gamma_{yx} & \Gamma_{yy} \end{bmatrix} \tag{5.17}$$

which is obtained from the unit cell period analysis.

5.7.2.1 Solution Procedure

The solution procedure starts by having two RAS models for a reflectarray feed covering both the radiation and scattering modes as previously presented. Then, the solution steps can be enumerated as

1. Compute the first hit fields over the reflectarray aperture due to the radiating antenna, which is also $\mathbf{E}_1^i$ in Eq. (5.16).

2. Compute the PO back scattering by the reflectarray aperture due to the magnetic current in Eq. (5.16), which is $\mathbf{E}_m^{PO}$ in Eq. (5.15).

3. Compute the plane wave complex amplitude contribution (E_m^{pw}) for the RAS scattering model by averaging the near fields radiating electric fields from the PO representation as

$$E_m^{pw} = \frac{1}{S^f} \int_{S^f} \hat{\mathbf{co}} \cdot \mathbf{E}_m^{PO} dS^f \tag{5.18}$$

   where S^f is the feed antenna aperture area and $\hat{\mathbf{co}}$ is a unit vector in the co-polarized direction of the radiating antenna.

4. The feed antenna scattering model's back scattering is used to compute the next hit field distribution over the reflectarray aperture, which is $\mathbf{E}_m^i$ for $m > 1$.

5. step 2 is repeated till the desired accuracy of computations is obtained using the new incident field distribution.

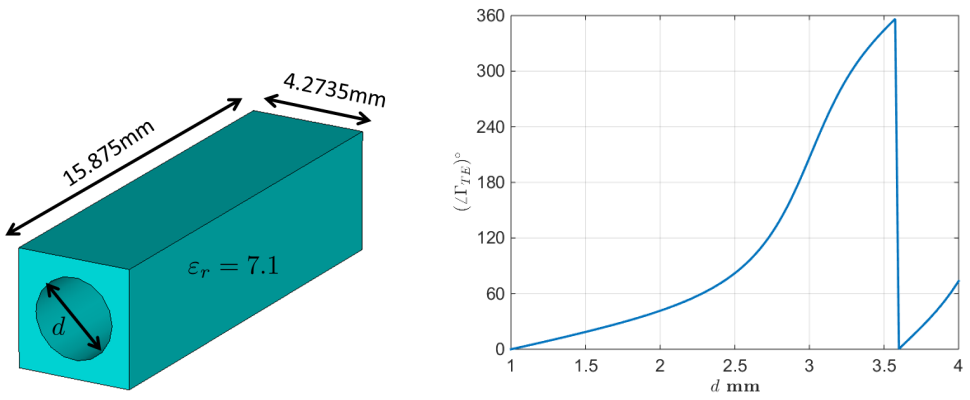

(a) (b)

Figure 5.16: The studied reflectarray unit cell. (a) The studied unit cell structure. (b) The reflection phase versus hole diameter.

6. The far fields are computed using all the contributions presented in Eq. (5.15) and illustrated in Fig. 5.15.

5.7.2.2 Sample Results

To verify the proposed approach, a reflectarray unit cell is designed using perforated Pyrex material with a dielectric constant of 7.1 as reported in [5]. The unit cell is designed at 11.7 GHz, which is the center frequency of the X-Ku satellite communication frequency band (10.7 GHz - 12.7 GHz). The structure details of the reflectarray unit cell are shown in Fig. 5.16 (a) and the phase response as the hole diameter changes is shown in Fig. 5.16 (b). A $12'' \times 12''$ reflectarray aperture is designed to verify the proposed procedure as shown in Fig. 5.17 (a) with $F/D = 0.7885$. The frequency response of the reflectarray in terms of antenna gain is presented in Fig. 5.17 (b) compared to the RAS/PO-MR predicted curve. The wideband response of the RAS/PO-MR procedure is obtained by solving the problem at different frequency points using antenna models that are valid at each frequency. It is worth mentioning that the computed antenna gain for the RAS/PO-MR method is obtained using the

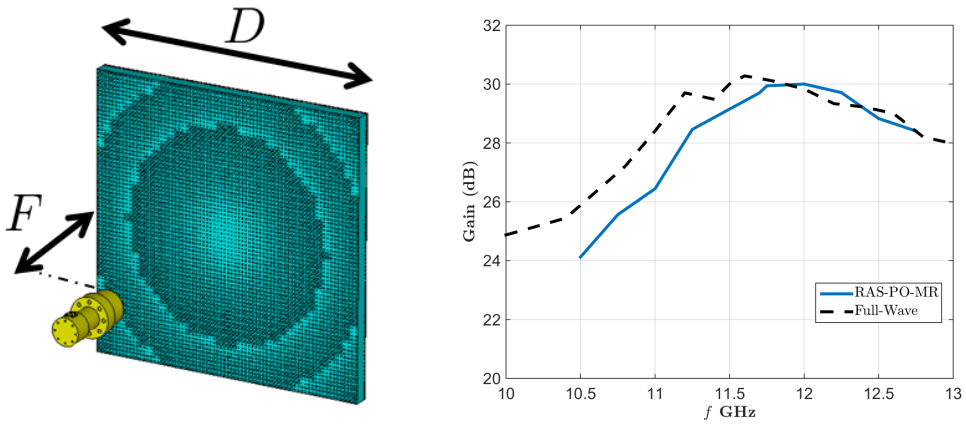

(a) (b)

Figure 5.17: The studied reflectarray layout with $F/D = 0.7885$ and its bandwidth potential test with the proposed method. (a) Reflecarray structure using the proposed unit cell in Fig. 5.16. (b) The predicted gain curve showing the possible bandwidth potential by the proposed method compared to the full-wave analysis.

definition in [48]. Although the frequency responses are not identical, the RAS/PO-MR provides a fair estimate for the reflectarray performance; especially at the upper side of the frequency band. Nevertheless, the main reasons behind the differences between the full-wave computations and the RAS/PO-MR approach can be the inaccurate representation of the scattering from the feed by considering the plane wave incidence and inaccurate phase compensation by the unit cells, even at the design frequency. However, a great advantage of the proposed RAS/PO-MR method is the potential speed, which requires less than 5 minutes on a personal computer to generate the results in Fig. 5.17 (b) compared to more than 2 hours on a GPU enabled computation server.

Another important advantage of the proposed RAS/PO-MR is the ability to provide more accurate prediction of the reflectarray radiation pattern by considering blockage and forward scattering of the feed. At the few seconds processing time, better representation of the radiation pattern is obtained as shown in Fig. 5.18 for the E and H planes. The results show that the proposed RAS/PO-MR method gives accurate representations for the first and second side lobes, which are mainly due

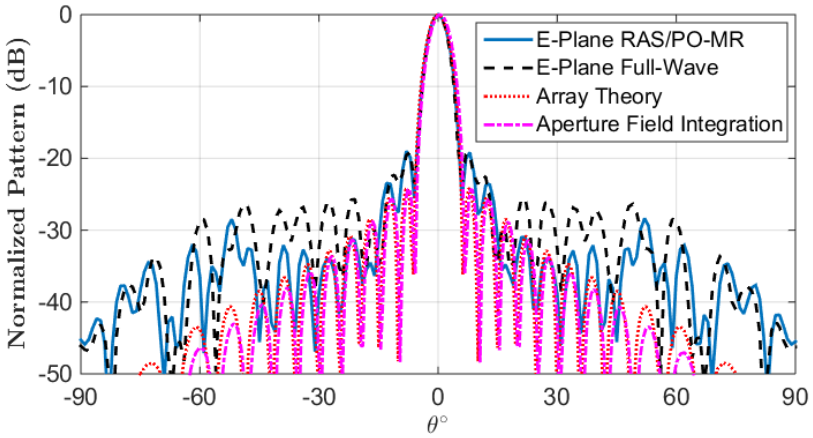

(a)

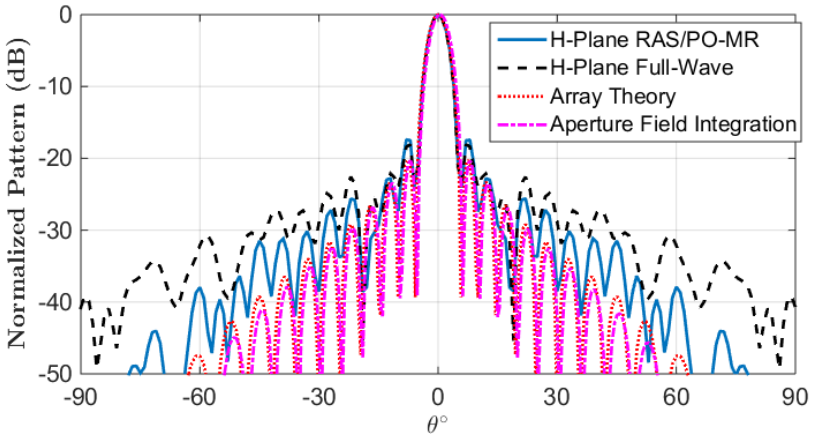

(b)

Figure 5.18: A comparison between the computed radiation pattern and the patterns obtained by different approximate methods. (a) E-plane. (b) H-plane

to the forward scattering of the feed, compared to the traditional array theory or aperture field integration methods.

5.8 Summary

An efficient, simple, fast, and accurate EM solver for arbitrary 3D problems was proposed. The presented technique solved iteratively problems by introducing random

auxiliary sources in pre-determined domain(s) with unknown orientations and amplitudes. Solutions were obtained by directly enforcing the boundary conditions of the original problem on the equivalent problems. The proposed procedure showed a remarkable improvement in the required solution time and memory in comparison to the surface equivalent based MoM technique. The properties of the proposed technique embraced the inherent special characteristics of the CLSM matrices to further accelerate the procedure and decrease the required memory to store necessary information for reuse. The proposed procedure with the random choices of solution sources proved to perform better than the deterministic choices offered by other procedures. The technique exhibited a stable performance by applying the rule of thumb criterion of the required number of sources per iteration. Also, the equations' dependency due to randomness has been investigated to have a qualitative measure of possible sources of numerical noise. In addition, the complexity order of the proposed method was identified to ease classifying the proposed method among other numerical techniques. Moreover, the special treatment required for problems with wedges has been addressed elaborating its advantages over similar approaches. The results have been verified and compared with analytic solutions for canonical problems and a commercially available integral equation solver for arbitrary problems. This method can be used for almost any boundary condition type and combinations of them as well.

The proposed method was also extended to provide simplified models for antennas in their radiating or scattering modes. These models were used to approximately analyze reflectarray antennas using a means of multiple reflections procedure. The results of the proposed method were verified against full-wave analysis and proved fair accuracy given the required time to obtain results from few minutes using the proposed method on a personal computer to a few hours using GPU loaded computational server.

Chapter 6

Optically Transparent Reflectarray Antenna Design Integrated with Solar Cells

6.1 Introduction

The conventional linear relation between the solar cell area and the harvested electric energy [126] motivates antenna engineers to develop solutions to make use of the large offered area. Therefore, the use of reflectarray antnenas [49, 50], when properly integrated with solar cells, provides a promising solution to integrate antennas with solar cells in a compact form. Typically, reflectarray antenna consists of a two dimensional array of reflective elements, which contribute to adjust the phase of an incident electromagnetic wave to produce the desired beam shape [124]. The main advantage of such structures is the ease in fabrication and flexibility in design, which make reflectarray antennas a promising alternative for conventional reflector antennas for some applications [124], despite the bandwidth limitations [127]. Various implementations of the reflectarray antenna concept have been presented featuring variable size printed

resonant reflective structures (i.e. patches [128–130] or dipoles [131, 132]), aperture coupled variable delay lines [133] or others [134–136].

One of the numerous reflectarray designs that inspired us to pursue this work is the perforated dielectric reflectarrays presented in [135, 137, 138]. These designs exploits variable air holes/gaps in dielectric materials to engineer the dielectric constant to achieve certain aperture reflected phase distribution. These designs featured a moderate bandwidth and aperture efficiency. Thus, this approach can be implemented over optically transparent materials to provide minimum blockage for solar cells.

In this chapter, the design procedure of an optically transparent reflectarray antenna integrated with solar cells is presented to operate within the satellite communication band (10.7 GHz - 12.7 GHz). Initially, the synthesis and design of an optimum reflectarray feed antenna are presented with the purpose of enhancing the achievable aperture efficiency while maintaining overall compact antenna sizes. Then, the proposed reflectarray unit cell analysis and design are introduced using a stacked perforated transparent acrylic backed by solar cells. Practical considerations related to the choice of materials and feature sizes are presented to have realizable designs. Moreover, the oblique incidence analysis in rigorously incorporated into the design procedure including the anisotropic surface impedance boundary effects and two port analysis of the stacked dielectric. Furthermore, the designed antenna is fabricated and measured to evaluate both its antenna and solar power harvesting performances.

6.2 Feed Antenna Design

A typical reflector antenna design procedure focuses on the design of the feed antenna as it is the main element to control the aperture efficiency of the reflector antenna [123]. Therefore, careful designing for the reflectarray antenna feed is favorable to achieve high aperture efficiency. Since reflectarray antennas are not necessarily

made out of metallic structures as reflector antennas, various research groups presented several solutions for higher radiation efficiency [139–141]. Consequently, the overall aperture efficiency of the antenna (η_{ap}) can be increased as it is the product of the spillover efficiency (η_s), field tapering efficiency (η_t) and radiation efficiency (η_r) as $\eta_{ap} = \eta_s\eta_t\eta_r$ [124]. As the aperture efficiency limit is set by spillover and field taper sub-efficiency values, improving the feed dependent sub-efficiency values is a key factor to improve the overall limiting aperture efficiency. One way to improve the feed dependent sub-efficiency components is by using directive feed antennas. The implications of exploiting high directivity feeds is mainly mechanical due to the need for placing the feed far from the reflector to operate at the optimum point following any theoretical analysis as presented in [124, 125]. Moreover, it adds more challenges to design good high performance feeds with high directivity and acceptable amplitude tapering, aperture phase and side lobe level, which may complicate the design dramatically. Another important point regarding reflectarray antennas is that the field taper efficiency is affected by both the radiation characteristics of the feed and the relative difference in path loss between different points, which affect magnitude as well as phase distribution over aperture. Therefore, preferred feeds for parabolic reflector antennas are not necessarily the best choice for reflectarrays. Special designs for reflectarray feeds are mandatory to improve the obtained aperture efficiency and so is maintaining a reasonable distance between the feed and reflectarray aperture.

Upon designing feed antennas specifically for reflectarrays, a coupled tapered slot line antenna was designed to provide a radiation pattern with the purpose of accounting for the different path loss on the reflectarray aperture in only one plane in [142]. The provided design only achieved pattern tapering in one plane with no information about the other plane. Also, the design suffers from high side-lobe levels that make it not suitable as reflectarray feed. Alternatively, several designs for primary feed antennas for deep parabolic reflectors have been proposed exhibiting partial-null

beam shapes in [143–146]. These proposed designs inspire adopting the concept of using engineered circular horn antennas backed with coaxial cavity to improve the efficiency limits from reflectarrays.

Here, a synthesis approach to the optimum feeds' radiation patterns to be used with reflectarray antennas based on an inverse problem formulation is presented for both center and offset fed reflectarrays. General theoretical specifications are defined to characterize reflectarray feeds with the purpose of improving the achievable aperture efficiency (η_{ap}) in a more compatible approach with reflectarrays. Furthermore, a realization approach to the defined radiation pattern specifications is proposed based on using coaxial cavity backed conical horns. The computed aperture sub-efficiency values of the proposed designs are compared to conventional conical horns to evaluate the performance enhancements using the introduced synthesis concept.

6.2.1 Inverse Radiation Pattern Synthesis Approach

A general reflectarray antenna feeding scenario can be considered for the offset case, where the antenna feed's phase center is located x_f from a square reflectarray center as shown in Fig. 6.1. The feed antenna radiation pattern can be reconstructed by the knowledge of two orthogonal planes (i.e., Plane-1 and Plane-2). For the planar reflectarray different path loss increases the field tapering of the feed that in turn reduce the aperture efficiency. Considering the previous fact into the synthesis process of reflectarray feed pattern, the magnitude distribution (D^i) of the incident wave over the aperture (S) can be expressed in the form

$$D^i\left(r\right) = \frac{\mathrm{P}\left(\theta_f, \varphi_f\right)}{r}; \quad \text{on } S \tag{6.1}$$

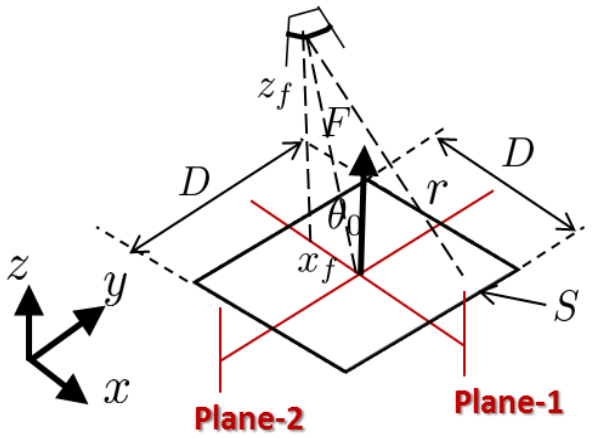

Figure 6.1: Reflectarray and feed layout with the two cut planes for then inverse feed pattern synthesis problem.

where $\mathrm{P}(\theta_f, \varphi_f)$ is the required feed radiation pattern as a function of the broadside feed's local spherical coordinates θ_f and φ_f. Consequently, the required optimum radiation pattern is the one that produces a uniform field distribution over the aperture (i.e., $D^i(r)$ is constant on S), which can be presented through trigonometric relations over the specified planes in the forms

$$\mathrm{P}\left(\theta_f, \varphi_f^{Plane-1}\right) = \frac{r}{F} = \frac{\cos\theta_f \pm \sin\theta_f \sqrt{\sec^2\theta_0 - 1}}{1 - \left(\sin\theta_f \sec\theta_0\right)^2} \tag{6.2}$$

where θ_0 is the inclination angle of the feed location over the z axis in Plane-1 and

$$\mathrm{P}\left(\theta_f, \varphi_f^{Plane-2}\right) = \sec\theta_f \tag{6.3}$$

with a body of revolution symmetry approach as presented in [123] according to the polarization of the feed antenna.

Examples to verify the previously defined pattern specification can be shown for both feeding scenarios of reflectarray. For a center-fed reflectarray layout, the inclination angle of the feed $\theta_0 = 0°$ and the desired F/D ratio of 0.8. The required antenna pattern plane cuts are shown in Fig. 6.2 (a) in comparison to best cosine

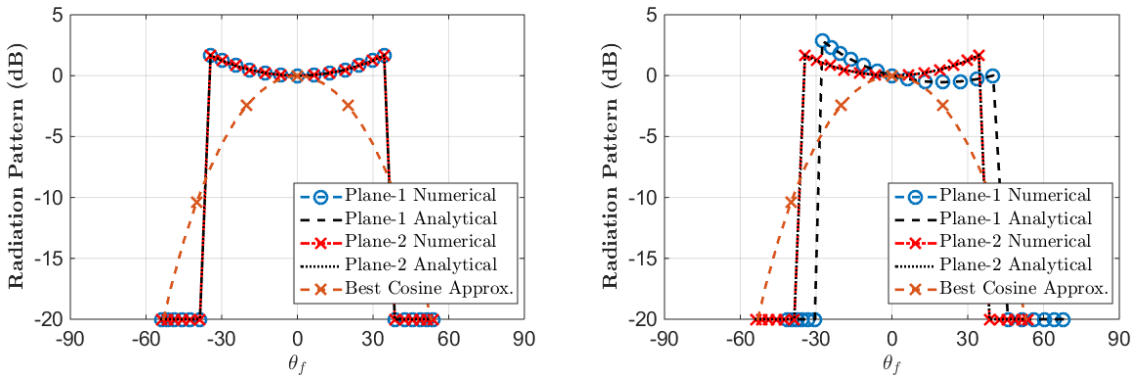

Figure 6.2: Optimum reflectarray pattern for $F/D = 0.8$ in comparison with a cosine approximation pattern that gives best results at the same position. (a) $\theta_0 = 0°$. (b) $\theta_0 = 20°$.

approximation pattern for the same F/D ratio (e.g. $P^c(\theta_f) = \cos^{4.5}\theta_f$). Also, Fig. 6.2 (b) presents the optimum pattern in case of offset-fed reflectarray with $\theta_0 = 20°$ for the same F/D ratio. The presented results show that the derived expressions match the numerically obtained results through a geometric inverse problem. Also, the optimum center feed pattern is required to have a dip in the broadside direction at $\theta_f = 0°$. The increase in the pattern as θ_f increases is required to compensate the difference in r as illustrated in Fig. 6.1 with a rapid decrease in the radiation pattern level outside the subtended angle of the feed and reflectarray. In addition, the offset feeding optimum radiation pattern requires similar specification as the center-fed case for Plane-2. In Plane-1, a tapered pattern in required to compensate the large variations in r along the reflectarray aperture. It is important to mention that the $\pm$ sign in Eq. (6.2) provides the presented tapering around $\theta_f = 0°$ depending on the sign of x_f. Generally, the difference between the provided optimum radiation patterns in Fig. 6.2 and cosine approximation patterns (e.g. radiated from conventional rectangular or circular horn antennas) provides qualitative measures of the predicted aperture efficiency from reflectarrays.

Using the previously defined radiation pattern with a body-of-revolution symmetry, the theoretical aperture sub-efficiency components, according to the definitions in [125], for the center-fed reflectarray case is presented in Fig. 6.3 (a). Furthermore, the results for the offset feeding case are presented in Fig. 6.3 (b). The results show larger values for the maximum achievable aperture efficiency for both cases (e.g., 86.24% and 80.34% for center and offset fed scenarios, respectively) compared to the cosine approximation pattern P^c (e.g., 72.69% and 45.86% for center and offset fed scenarios, respectively). Indeed, the theoretically achieved efficiency values are much higher than the results obtained using full wave analysis because the multiple interactions between the feed and reflectarray are not included. Also, the radiation pattern of individual reflectarray unit cells is not fully incorporated in the defined expressions in [125]. Moreover, the defined variations for the optimum radiation patterns are not possible to be achieved by a finite small feed antenna, but the presented results indicate the potential of using feeds with the specified characteristics to improve the obtained radiation efficiency. These characteristics include amplitude tapering to compensate the difference in path loss and rapid drops away from the specified subtended angle(s).

It is clear that the performance difference between the defined optimum pattern and cosine approximation pattern decreases as the subtended angle decreases by increasing F/D ratio (i.e. having the feed further away from the reflectarray). To clarify this point, an example is shown in Fig. 6.4 of a center feed antenna with F/D is considered 1.2. The optimum radiation patterns is shown in Fig. 6.4 (a) with a suitable cosine pattern with $P^c(\theta_f) = \cos^{12}\theta_f$. The aperture efficiency components results are shown in Fig. 6.4 (b). These results show that the more directive the antenna feed, the higher the aperture efficiency that can be obtained through a non-linear relation. However, realizing a horn feed with a radiation pattern approximated

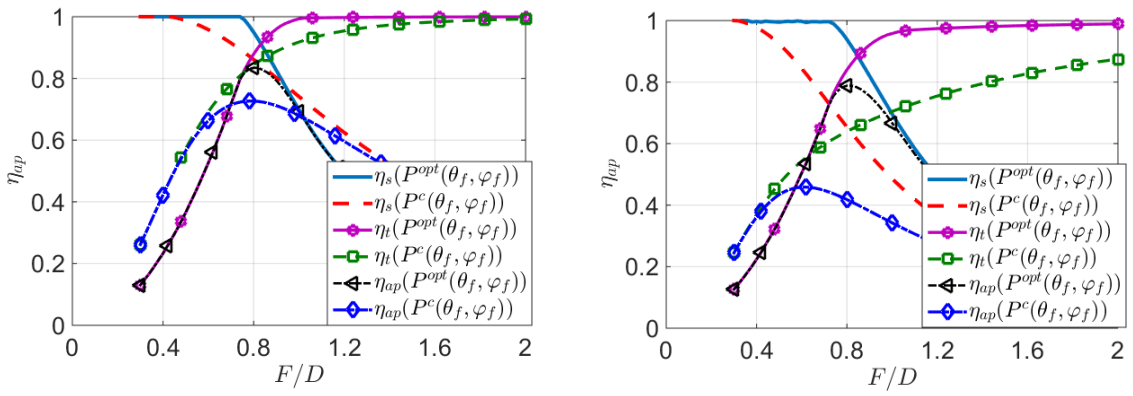

(a) (b)

Figure 6.3: Theoretical aperture efficiency components for the radiation patterns presented in Fig. 6.2 as a function of the relative distance between the feed and the reflectarray F/D. Here, the definition for the aperture efficiency is $\eta_{ap} = \eta_s \eta_t$. (a) $\theta_0 = 0°$. (b) $\theta_0 = 20°$.

with $P^c(\theta_f) = \cos^{12}\theta_f$ requires a large aperture size, which should definitely deteriorate the overall reflectarray performance due to blockage and multiple reflections in the case of center feeding.

6.2.2 Antennas Realization for Center Feeding Layout

Upon realizing an antenna to produce the required radiation pattern, certain design aspects are required to be respected during the design optimization. These design aspects include radiation pattern symmetry, having the required dip along the broadside direction of the feed, operating within a moderate subtended angle (e.g. $\sim 60°$), and having low cross polarization. In addition, the operating frequency is chosen to cover the satellite communication band X-Ku band (10.7 - 12.7 GHz). Consequently, the designed coaxial to circular waveguide transition is presented in Appendix C.3.

The proposed layout of the design can be shown in Fig. 6.5 consisting of a conical horn antenna surrounded by a coaxial cavity of depth D_c and width W_c. Also, the coaxial cavity is extended further from the horn aperture by U_c as presented in the section view in Fig. 6.5 (b). The initial step to the design is to choose the horn

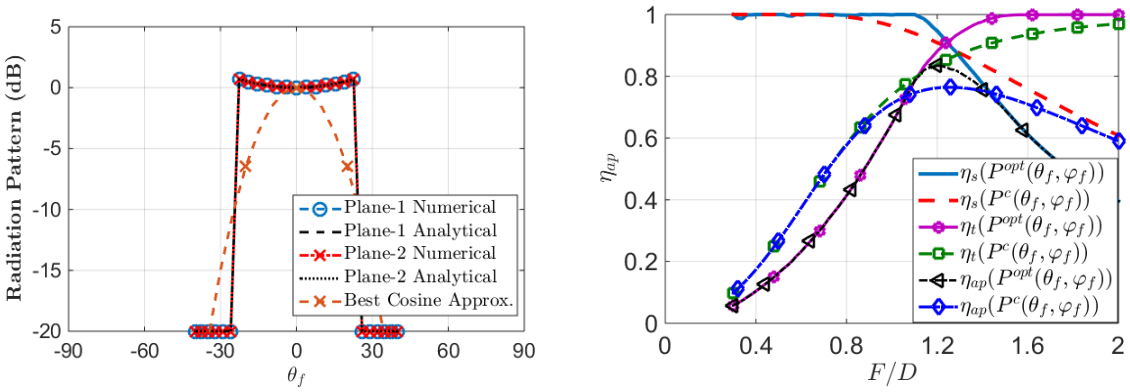

(a) (b)

Figure 6.4: An example for the center feed optimum radiation pattern to be used with reflectarray at $F/D = 1.2$ and a cosine approximation feed pattern for same specifications. (a) Optimum radiation patterns. (b) Aperture efficiency components.

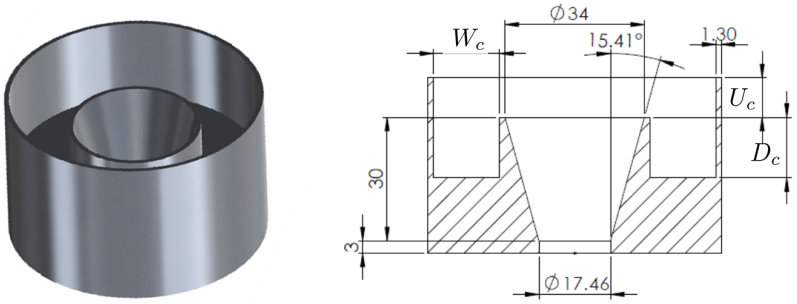

(a) (b)

Figure 6.5: The proposed initial design for a coaxial cavity backed circular horn antenna. (a) Isometric view. (b) Section view with all dimensions in millimeter.

dimensions to have a simulated gain 12.3 dB, which has an optimal subtended angle 64.75° (i.e., $F/D = 0.7885$) using the theoretical analysis presented in [124]. The second step is to engineer the radiation pattern to have the required characteristics by changing the design parameters U_c, D_c and W_c.

Numerical optimization has been performed to optimize the coaxial cavity parameters to compromise between the pattern dip and symmetry within the subtended angles using the design parameters D_c, W_c and U_c at the center frequency $f_0 = 11.7$ GHz. The local optimization ended up with $D_c = 0.573\lambda_0$, $W_c = 0.629\lambda_0$ and $U_c = 0.374\lambda_0$.

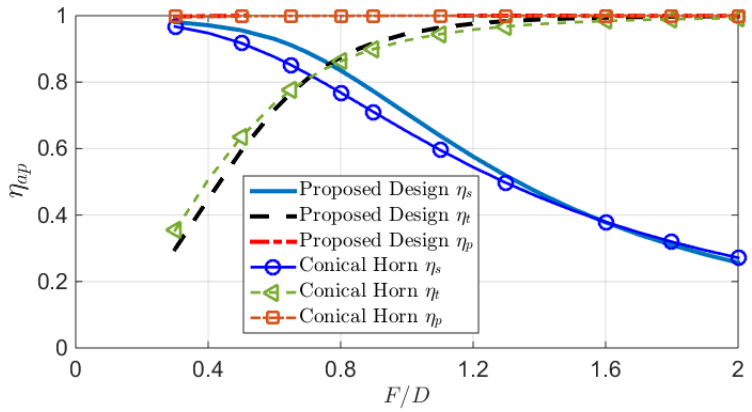

(a)

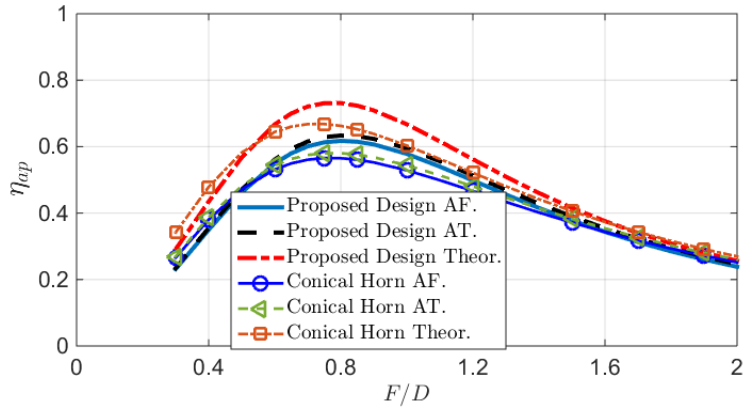

(b)

Figure 6.6: Aperture sub-efficiencies comparison between the proposed design in Fig. 6.5 and a conical horn of the same dimensions. (a) Sub-efficiency components with η_p represents the polarization efficiency defined in [123]. (b) Array theory (AT) and aperture field integration (AF) efficiency evaluation and the theoretical aperture efficiency.

It is important to state the optimized values are significantly different from the values presented for open-ended waveguide feeds [143, 145]. This difference is mainly due to the presence of the horn antenna and its contribution to the tapering and phasing of the fields on the aperture, which consequently affects the required cavity dimensions. The optimized pattern is compared to the horn without cavity pattern and the optimum pattern for the same F/D in Fig. 6.7 using CST [108]. Here, the radiation patterns are presented in the E-plane ($y-z$ plane), H-plane ($x-z$ plane) and cross polarization (X-pol) at the 45° plane using Ludwig III definition of cross

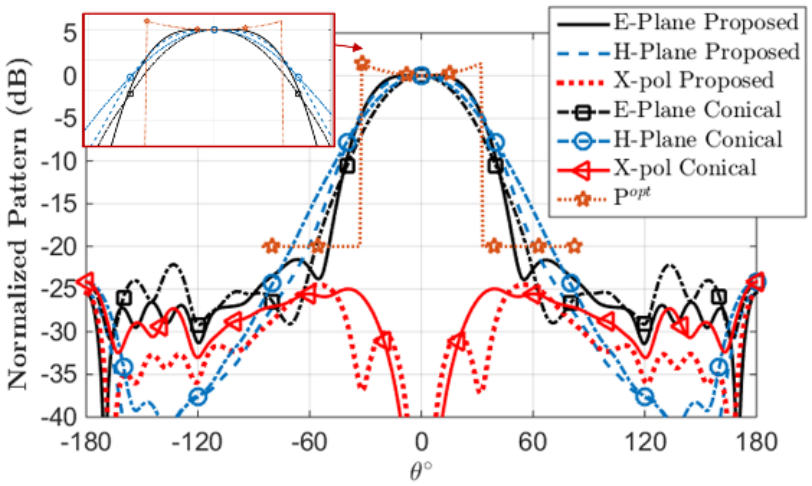

Figure 6.7: Comparison between the optimized coaxial cavity backed horn antenna with the conical horn antenna (without cavity) and the theoretical optimum pattern specified by Eq. (6.2) at $f_0 = 11.7$ GHz.

polarization [122]. The resulting pattern comparison shows the improvement over conventional conical horn antenna in terms of spilled over energy and field tapering within the subtended angle having the optimum pattern as a reference. Fig. 6.6 shows the sub-efficiency components using the definitions in [125] and the array theory and aperture field integration [124]. The results show significant improvement in the aperture sub-efficiencies using all different methods over the conventional conical horn design without coaxial cavity as presented in Fig. 6.6 (b) (around 6% increase). It is worth mentioning that the proposed design concept can be extended to have multiple concentric coaxial cavities as proposed by Koch [143] to reach closer to the optimum design as proposed previously in this work. However, this increases the feed aperture area that may have drawbacks in blockage and interaction with the reflectarray in a destructive way.

The final design of the feed antenna can be further enhanced by introducing a narrow $\lambda_0/4$ choke ring around the coaxial cavity to improve the spillover efficiency by lowering the radiation pattern levels further beyond the reflectarray subtended angle. The design structure details and dimensions are presented in Fig. 6.8. A

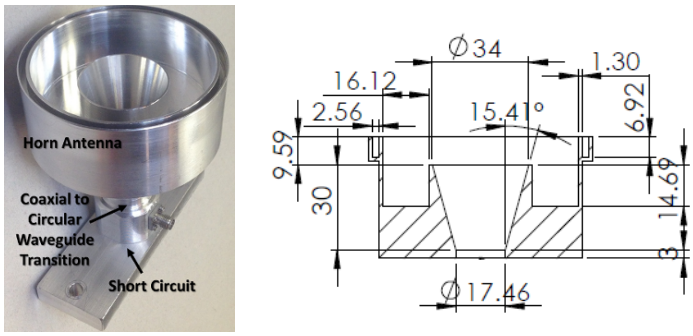

(a) (b)

Figure 6.8: The proposed coaxial surrounding the conical circular horn with choke. (a) Fabricated model. (b) A cross section view to the design details with all dimensions in millimeter.

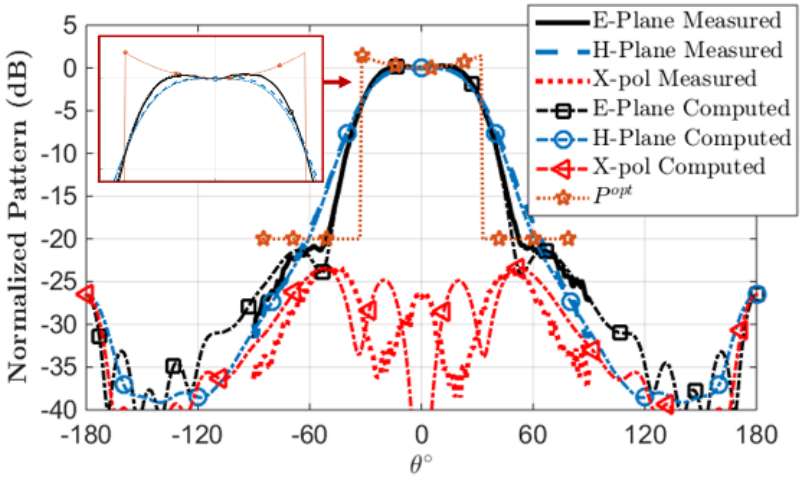

Figure 6.9: A comparison between the measured and computed radiation patterns of the proposed design in Fig. 6.8 at $f_0 = 11.7$ GHz.

comparison between the simulated and measured radiation patterns is presented in Fig. 6.9 as well as the theoretical optimum pattern given by Eq. (6.2) showing very good agreement with simulation. Fig. 6.10 shows the predicted aperture efficiency using different theoretical analysis methods compared to a conical horn of the same flaring dimensions. Superior spillover and tapering efficiencies are achieved. It is important to elaborate that the computed aperture efficiency values are obtained using equivalent infinitesimal dipole models inspired by the work presented in [107, 115], which is beyond the scope of this work. Moreover, the measured and simulated

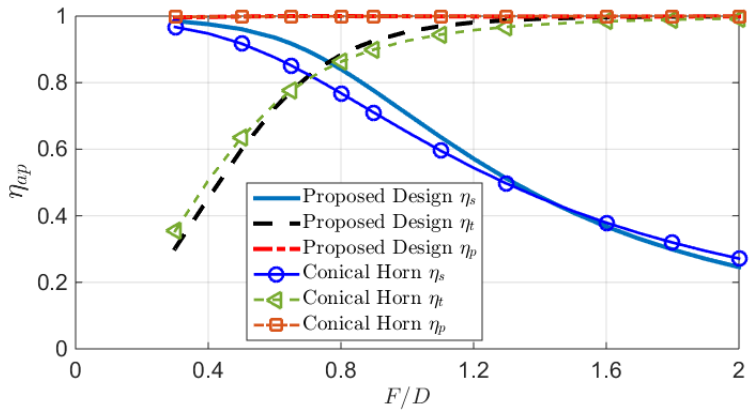

(a)

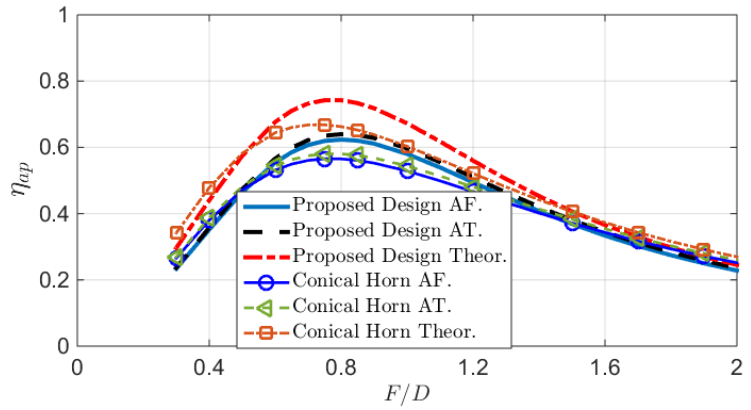

(b)

Figure 6.10: Aperture sub-efficiency components for the present design in Fig. 6.8 and a conical horn. (a) Sub-efficiency components. (b) Array theory (AT) and aperture field integration (AF) efficiencies and the theoretical aperture efficiency.

reflection coefficients are presented in Fig. 6.11 with an acceptable agreement across the operating frequency band. Moreover, the radiation patterns presented in Fig. 6.12 indicate the pattern stability for the entire frequency band. The results of this design indicate around 7% increase over the conical horn antenna feed in the predicted aperture efficiency. In addition to the proposed reflectarray optimized center feed antenna, other antennas are optimized for offset feeding scinarios and presented in Appendix C

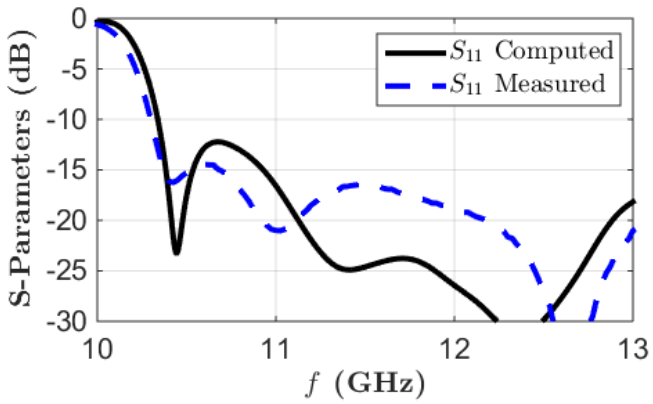

Figure 6.11: A comparison between the measured and computed reflection coefficients of the proposed design in Fig. 6.8.

6.3 Reflectarray Unit Cell Analysis

The main idea behind the proposed design is the choice of the reflectarray material that enables adequate phase correction plus optical transparency to transmit optical energy to solar cells. Thus, clear plastic or glass materials are the perfect candidates for such integration between antennas and solar cells as presented in [147]. Based on the available fabrication facilities, extruded acrylic material is exploited for the proposed design. The measured relative permittivity using the Agilent dielectric probe kit (85070E) for the commercially available material is presented in Fig. 6.13. However, it is important to notice the loss tangent at the design frequency 11.7 GHz is around 0.06, which is very close to the minimum expected value of the device that is prone to measurement errors as indicated in the device data sheet [148]. Alternatively, the presented design exploits a crystalline solar cell that is modeled as anisotropic surface impedance boundary as shown in Fig. 6.14 using the procedure illustrated in Chapter 3.

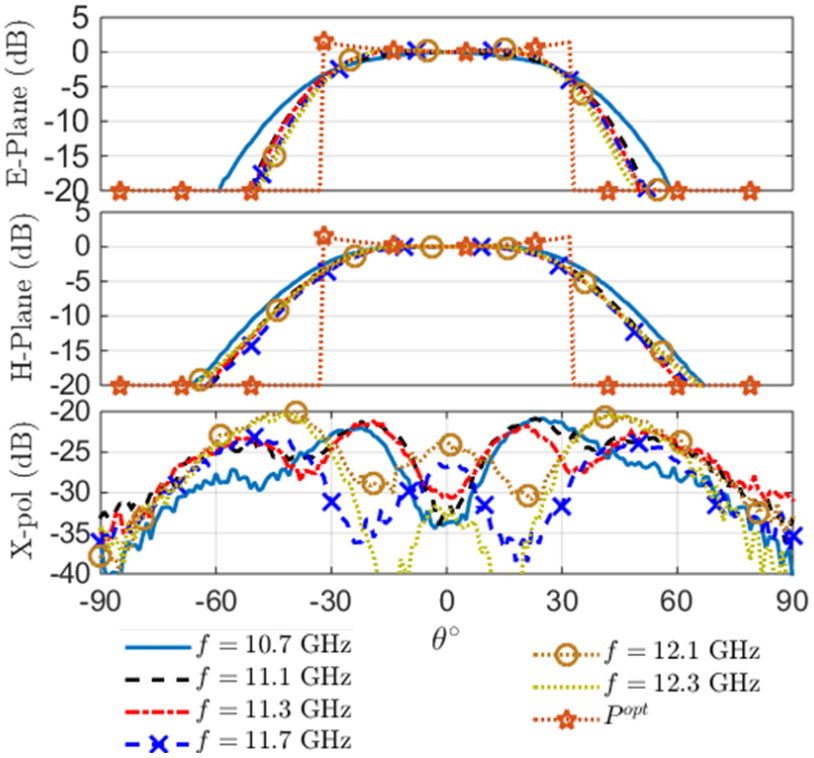

Figure 6.12: A comparison between the measured radiation patterns of the proposed design in Fig. 6.8 at different frequencies.

6.3.1 The Proposed Unit Cell

The proposed design exploits a stacked perforated acrylic unit cell as illustrated in Fig. 6.15 using five layers. The reason for this stacking instead of using one thick sheet is the drilling capability of the employed Universal Laser Systems (M300) laser platform, which has a maximum of 1/4" thick acrylic sheets. In terms of antenna/solar cells integration, different reflection performance is observed using the proposed unit cell for different orientation of the electric field with respect to the coordinate system identified in Fig. 6.15 assuming infinite periodicity [124]. Fig. 6.16 presents the normal incidence reflection results neglecting the losses in the acrylic material, which indicates that having the incident electric field parallel to the conducting metallic lattice of the solar cell (parallel to y) provides lower loss level compared to the other orientation.

The unit cell structure details are chosen to be of width ($W = \lambda_0/6$) at the design

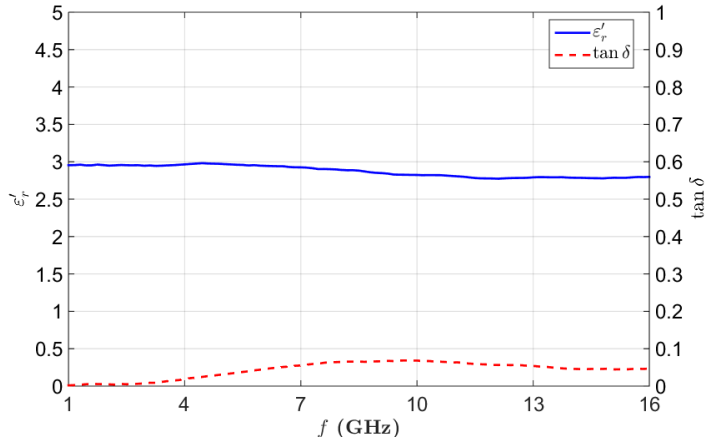

Figure 6.13: The measured dielectric constant results of extruded acrylic using Agilent dielectric probe kit.

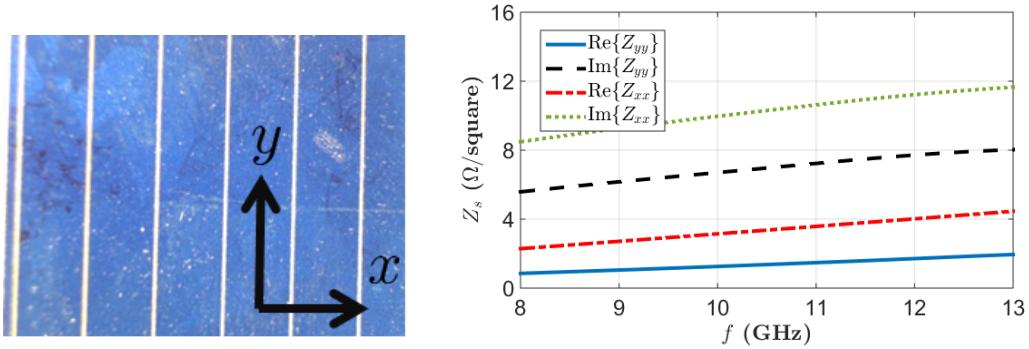

(a) (b)

Figure 6.14: The employed solar cell photo under a 10X microscope with the modeled anisotropic surface impedance in the X-band. (a) Solar cell photo with coordinate system definition. (b) Anisotropic surface impedance.

center frequency 11.7 GHz, where λ_0 is the free-space wavelength. The thickness of the stacked acrylic layers (H) is 1/4", but the measured samples provided 6.05mm due to production tolerance from the supplier. The design also incorporated a typical 0.1mm air gap between layers. This makes the simulated model closer to any fabricated model. Also, the diameter variation of the equally spaced holes is chosen to vary from 1mm to 3.775mm allowing a minimum distance between individual holes of around 0.5mm. Of course, these choices of limitations regarding the hole sizes are the reason of choosing five stacked layers of acrylic. Other choices may lead to using less

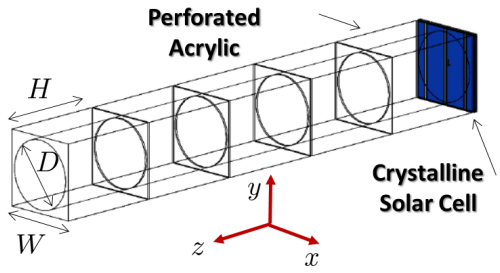

Figure 6.15: The optically transparent reflectarray unit cell integrated with a crystalline solar cell.

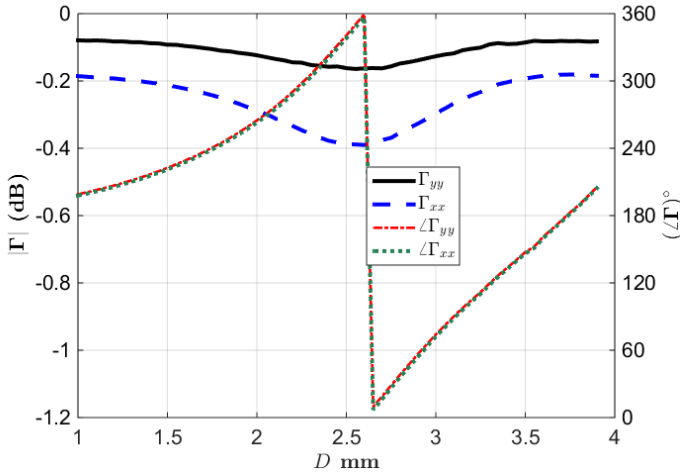

Figure 6.16: Computed normal incidence unit cell response of the proposed reflectarray unit cell in Fig. 6.15 neglecting the acrylic material losses.

number of stacked layers. Also, other choices of materials may lead to much thinner designs, such as borosilicate glass (Pyrex) with measured relative permittivity close to 5. However, for the proposed design, the machining capabilities limits the material choice to acrylic.

6.3.2 Oblique Incidence Analysis

As indicated in [147], oblique incidence analysis is essential for the proposed perforated thick dielectric unit cell as the phase response vary a lot with the angle of incidence. Furthermore, the employed anisotropic surface impedance homogenization of the effect of solar cells in the microwave range requires special treatment in terms

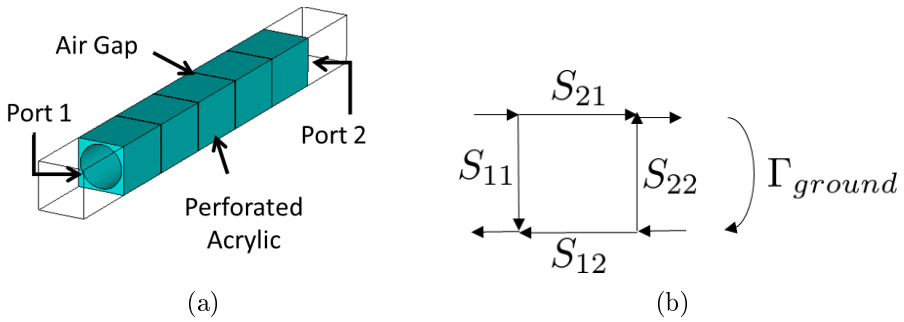

Figure 6.17: Two port analysis model of the proposed reflectarray perforated acrylic unit cell. (a) Two port full wave analysis model. (b) Two port network terminated with arbitrary reflection coefficient.

of rotating local coordinate systems and cross polarization as presented in Appendix D. In general, treating this unit cell analysis problem for arbitrary angle and planes of incidence requires a huge amount of simulations, which is very time consuming. Here, the unit cell analysis is divided into two cascaded sections: the stacked dielectric layers as a two port network and the anisotropic surface impedance termination as shown in Fig. 6.17. The stacked dielectric part is assumed plane of incidence independent (φ_e independent, where φ_e defines the plane of incidence with respect to the defined coordinate system in Fig. 6.18). Also, the surface impedance termination is φ_e dependent as presented in Appendix D, which is analyzed analytically. Consequently, signal flow graph or any other procedure [91] can be used to obtain the overall reflection coefficient of the unit cell as presented in Fig. 6.19. This results shows that the procedure is accurate for a single plane of incidence case ($y-z$ plane) for different angles of incidence (θ_e). Also, other polarization results can be shown to be of the same accuracy, but the results are removed for brevity.

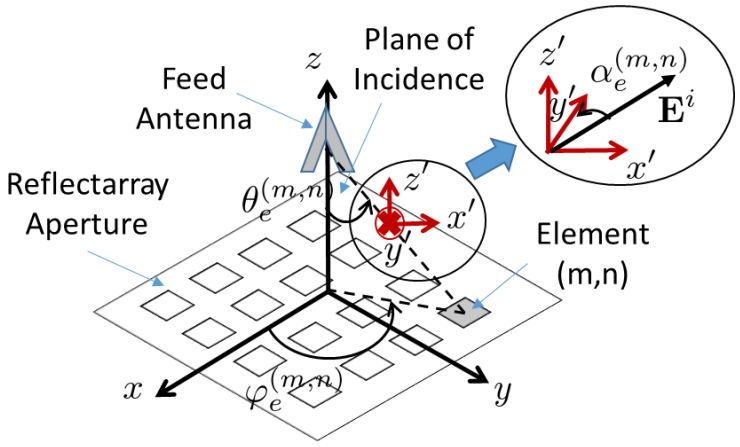

Figure 6.18: An illustration for the plane of incidence associated with the reflectarray unit cell (m,n).

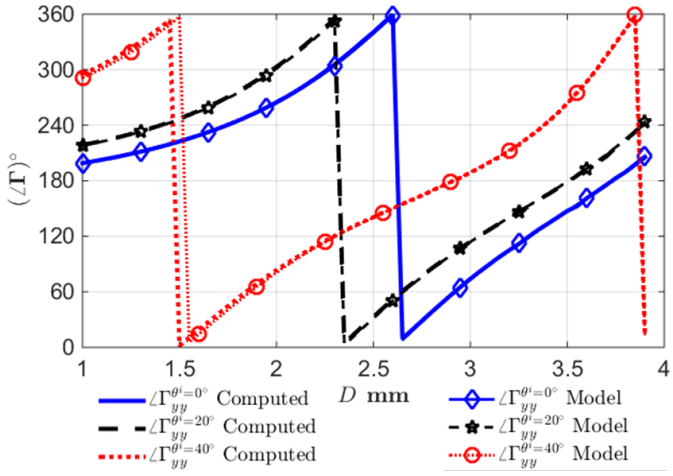

Figure 6.19: The computed and modeled phase response of the reflectarray unit cell shown in Fig. 6.15.

Assuming infinite periodicity perforated stacked acrylic sheets, the two port S-parameters can be described for each polarization separately without any cross coupling. These S-parameters can be expressed as

$$S^{TE(TM)} = \begin{bmatrix} S_{11}^{TE(TM)} & S_{12}^{TE(TM)} \\ S_{21}^{TE(TM)} & S_{22}^{TE(TM)} \end{bmatrix} \tag{6.4}$$

for the transverse electric (magnetic) incidence case. Also, reflection from the solar cells, which is modeled as anisotropic surface impedance can be written, as explained

in details in Appendix D, in the form

$$\Gamma = \begin{bmatrix} \Gamma_{TM}^{TM} & \Gamma_{TE}^{TM} \\ \Gamma_{TM}^{TE} & \Gamma_{TE}^{TE} \end{bmatrix} \tag{6.5}$$

where $\Gamma_{TM(TE)}^{TE(TM)}$ is the transverse electric (magnetic) reflection coefficient due to a transverse magnetic (electric) plane wave incidence (with all the possible combinations) on a specific plane of incidence defined by φ_e as explained in Appendix D. Consequently, the total reflection coefficients at the same plane of incidence can be obtained using signal flow graphs as

$$\begin{aligned} R_{TE}^{TE} &= S_{11}^{TE} + \frac{S_{21}^{TE} S_{12}^{TE}}{1 + S_{22}^{TE} \Gamma_{TE}^{TE}}, \\ R_{TE}^{TM} &= S_{21}^{TE} \Gamma_{TE}^{TM} S_{12}^{TM}, \\ R_{TM}^{TE} &= S_{21}^{TM} \Gamma_{TM}^{TE} S_{12}^{TE}, \\ R_{TM}^{TM} &= S_{11}^{TM} + \frac{S_{21}^{TM} S_{12}^{TM}}{1 + S_{22}^{TM} \Gamma_{TM}^{TM}} \end{aligned} \tag{6.6}$$

where $R_{TM(TE)}^{TE(TM)}$ is the combined transverse electric (magnetic) reflection coefficient of the structure due to a transverse magnetic (electric) plane wave incidence. These findings are to be rotated back to the global coordinate system of the reflectarray to get the co-polar reflection coefficient as

$$\Gamma_{co} = \hat{\mathbf{co}} \cdot \begin{bmatrix} \cos\varphi_e & -\sin\varphi_e \\ \sin\varphi_e & \cos\varphi_e \end{bmatrix} \begin{bmatrix} R_{TM}^{TM} & R_{TE}^{TM} \\ R_{TM}^{TE} & R_{TE}^{TE} \end{bmatrix} \begin{bmatrix} \sin\alpha_e \\ \cos\alpha_e \end{bmatrix} \tag{6.7}$$

where $(\cdot)$ denotes the dot product between two vectors and $\hat{\mathbf{co}}$ is the co-polar unit vector, which is considered $\hat{\mathbf{y}}$ in this design. Also, the angle α_e is the polarization angle to determine the contribution of the transverse electric and magnetic components

in the plane of incidence for each individual reflection case. This angle is always measured from the transverse axis to the plane of incidence ($\hat{\mathbf{y}}'$). This oblique incidence analysis is a general formula that can be used with any reflectarray synthesis using the reflection from unit cell. Only $\Gamma_{TM(TE)}^{TE(TM)}$ values have to be considered as functions of φ_e and θ_e.

It is worth mentioning that the two port analysis of the dielectric unit cell relied on the full-wave analysis of CST [108] because the approximate perforation formula, presented in [149], does not provide accurate representation of the employed 'thick' perforated dielectric slabs. The discrepancies between the full-wave analysis results and the approximate results for the homogenized permittivity dielectric constant increase as the angle of incidence θ_e increases. Nevertheless, it can be shown that this problem appears for thick dielectric slabs, while the approximation formula works fairly for thin dielectric slabs. Therefore, full-wave simulations were used to generate the two port analysis results of the perforated dielectric, as shown in Fig. 6.17(a), for different angles of incidence.

6.4 Reflectarray Design and Measurement Results

The area of the reflectarray aperture is chosen to 11.5" $\times$ 11.5" as the maximum allowed working size of the employed laser platform. The distance between the reflectarray aperture and the feed phase center is chosen to be 9.229" for maximum achievable directivity. Consequently, the reflectarray unit cells are required to achieve the phase shifts shown in Fig. 6.20 through varying hole sizes. Here, the fabricated prototype is presented including its realization challenges. Also, the antenna and solar cells performance are discussed through experiments.

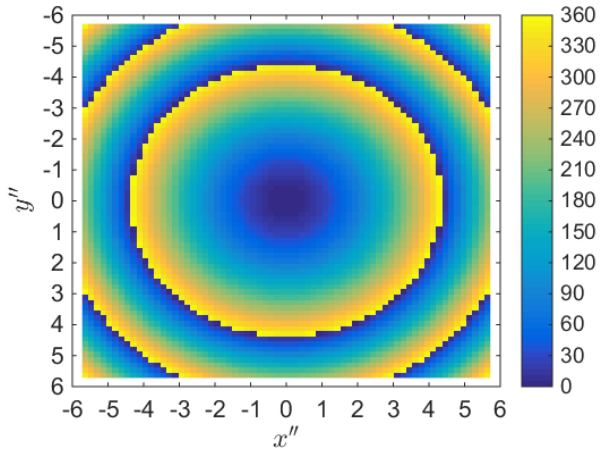

Figure 6.20: The required phase shift by the reflectarray unit cells.

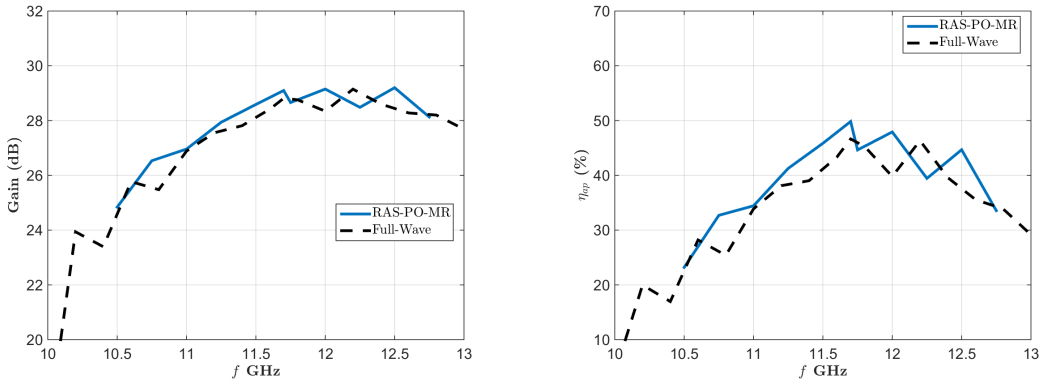

(a) (b)

Figure 6.21: A comparison between the predicted reflectarray antenna performance using the RAS/PO-MR method and full-wave computations using lossless acrylic material. (a) Antenna gain performance. (b) Aperture efficiency.

6.4.1 Approximate Reflectarray Performance

By using the proposed RAS/PO-MR method presented in Chapter 5, a fast prediction to the reflectarray antenna performance can be obtained. Initially, a lossless acrylic case is considered to estimate the best antenna performance neglecting the losses inside the acrylic as the measurements in Fig. 6.13 are not expected to be accurate [148]. A comparison between the predicted performance of the RAS/PO-MR method and the full-wave computations of CST is shown in Fig. 6.21 for both

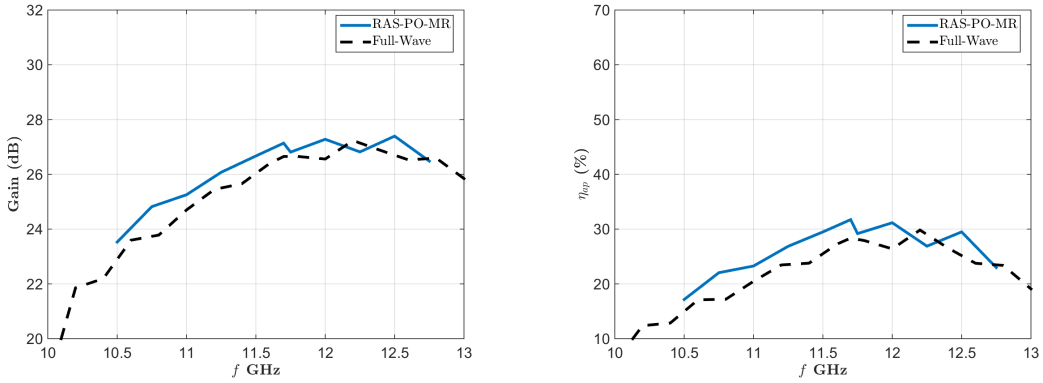

(a) (b)

Figure 6.22: A comparison between the predicted reflectarray antenna performance using the RAS/PO-MR method and full-wave computations using lossy acrylic material. (a) Antenna gain performance. (b) Aperture efficiency.

the expected gain and aperture efficiency. Furthermore, a better estimation of the acrylic material losses is obtained through the antenna measurements as shown in the coming subsection to have the loss tangent $\tan\delta = 0.022$. This value is used to further predict the reflectarray antenna gain and aperture efficiency in comparison to full-wave computations as shown in Fig. 6.22. The comparison between the lossless and lossy acrylic cases show the significant effect of the dielectric material losses over the overall antenna performance. Moreover, the frequency response results illustrate the validity of the proposed unit cell analysis method, which is very close to reality in this particular reflectarray antenna design. In addition, the reflectarray antenna radiation pattern is also predicted through the proposed RAS/PO-MR method as shown in Fig. 6.23 in comparison to the full-wave computations of CST. The presented radiation patterns show accurate prediction for the first side lobe level, which is not possible to be predicted using other approximate methods.

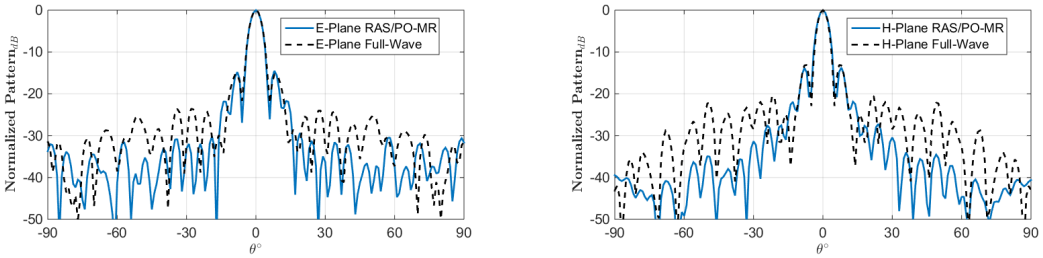

(a) (b)

Figure 6.23: A comparison between the predicted reflectarray radiation pattern using the RAS/PO-MR method and full-wave computations using lossy acrylic material. (a) E-plane. (b) H-plane.

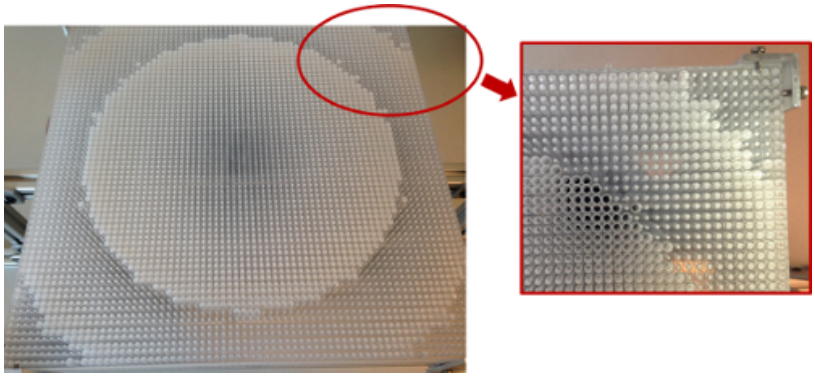

Figure 6.24: The fabricated phase shifting perforated reflectarray aperture.

6.4.2 The Fabricated Prototype

A realized model of the stacked perforated dielectric is shown in Fig. 6.24 mounted on the designed reflectarray measurement setup. The solar cells and acrylic layers are snugly stacked together with four 90° corners, which apply pressure on top of them to minimize air gaps. The fabricated prototype of the proposed reflectarray is shown in Fig. 6.25 exploiting a center feeding conical horn backed by a coaxial cavity with a chock as proposed in [150]. The main advantage of this feed is that it produces a more uniform aperture field over the reflectarray aperture with less spillover as well as maintaining a relatively close distance to the reflectarray aperture than using directive feeds [150].

For mechanical stability, two thin struts (1/8" thick) are used to fix the structure

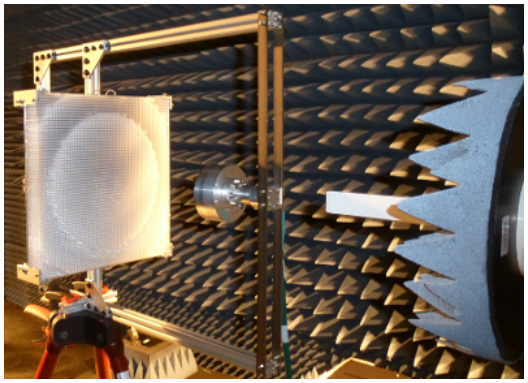

Figure 6.25: The fabricated prototype of the proposed reflectarray facing NSI near field scanner probe.

of the feed antenna from the back. They were chosen to be along the antenna's H-plane, where the electric field interacts with a smaller area of the struts [151], thus less forward scattering is observed due to the struts. To prove the previously mentioned statement, the feed antenna structure is simulated with CST as a scatterer as shown in Fig. 6.26 (a) with a uniform plane wave incidence in the illustrated polarization. The computed Radar Cross Section (RCS) of the structure in the E and H planes are presented in Figs. 6.26 (b) and 6.26 (c), respectively, for different values of the struts length L. The results show that minimal effects are observed in the far fields in the main broadside beam direction. The effects are mainly minor side lobe contributions.

6.4.3 Reflectarray Antenna Performance

A preliminary experiment to measure the performance of the proposed antenna is conducted by measuring the antenna parameters excluding the solar cells from underneath the perforated acrylic sheets. This experiment helps to characterize the effect of the solar cells on the antenna performance noting that the modeled effect of the solar cells is close to conductors in terms of surface impedance. Another important motivation behind this initial experiment is to predict the loss tangent of acrylic. Since the employed dielectric probe measurement results shown in Sec. 6.3 shows close to the minimum limit loss tangent, the accuracy of this measurement is

questionable according to the device data sheet [148]. Fig. 6.27 shows a comparison between the measured and computed reflectarray antenna directivity and gain using different values of the loss tangent for the exact same structure. It is found that the measured results are closer to the computed results with $\tan\delta = 0.022$, which is lower than the values obtained by the dielectric probe test in Fig. 6.13. It is important to notice that the measured directivity is obtained by integrating two radiation pattern cuts and assuming a body of revolution symmetry as indicated in [152].

The reflection coefficient measurement of the reflectarray integrated with solar cells is shown in Fig. 6.28 in comparison with the no solar cells case and full-wave computations with a good agreement. The main reason in the slight discrepancies between measurements and full-wave computations is actually due to the fabrication tolerance in the feed antenna as presented in the same figure. Also, the reflection coefficient measurements show an acceptable matching level (below -10dB) for the entire frequency band of interest. Moreover, a comparison between the computed and measured radiation pattern is presented in Fig. 6.29 for the standard E and H planes. Also, the maximum measured cross polarization level is compared to the computed results in Fig. 6.29 (c) at the 45° plane cut using the Ludwig III definition of cross polarization [122]. It is found to be below -25dB within the antenna 3dB beam width, which is $|\theta| = 2.6°$ (half angle). It is important to notice that the slight difference in the side lobe level in the E-plane shown in Fig. 6.29 (a) is due to a minor difference between the simulated and fabricated models of the feed antenna in the exterior part, which does not affect the radiating part, but affects the forward scattering of the feed.

The antenna performance through the operating frequency band of the satellite communications (10.7 GHz - 12.7GHz) shows good agreement between the computed and measured results in terms of gain as shown in Fig. 6.30. It has to be noted that the measured gain is terminated at 12.4 GHz due to the use of a near field scanner

in only the X-band, which is the available facility to us. Furthermore, the radiation efficiency plot in Fig. 6.31 indicates that most of the losses are due to the acrylic material and the solar cells are only responsible for $\sim$ 0.2dB in the computed mode and $\sim$ 0.5dB in measurements. Also, the aperture efficiency [124] of the antenna is presented in Fig. 6.32 indicating around 25% efficiency at the design frequency. These results show that solar cells do not have a significant loss over the antenna compared to the effect of the employed transparent material. Since we were limited by the available commercial materials and fabrication facilities, other possible transparent materials can be used with lower loss level, which indeed shall improve the overall reflectarray antenna performance.

6.4.4 Solar Harvesting Performance

Following up on the design procedure, the solar cells are required to cover all the area underneath the reflectarray. Thus, four unpackaged solar cells panels (6"×6" each) are connected together in parallel leaving no space in between. The solar cells' edges were trimmed beyond the 11.5"×11.5" reflectarray aperture. The output solar cells' power is measured under direct sun in a sunny day (June 4, 2015) in Montréal, Québec as shown in Fig. 6.33, where the tilting angle plane is fixed towards south. Using a metallic setup that allows changing the angle of the whole antenna as illustrated in Fig. 6.33, the output short circuit current and open circuit voltage are measured consecutively for the covered and uncovered solar cells with results shown in Fig. 6.34. The first observation through this measurement is that the output solar power does not vary much from the solar cells alone case at the curve peak region, where the sun is perfectly normal to the reflectarray/solar cell. However, the output solar power is greatly affected by the cover reflectarray's acrylic at large angles (90°). The drawback about this measurement is that it is not fair to quantitatively compare the difference between the output power in the cases of with and without reflectarray

because both measurements are not done simultaneously (although they were done within 90 minutes) because of the slight differences in the sun angle and the presence of some clouds, which we noticed to affect the results. Nevertheless, this measurement is a qualitative measure of the effect of optically transparent reflectarray antenna on the solar cells' output power, which lines up with the results presented by Lim and Leung in [5]. It is important to mention that the employed solar cells are rated to produce around 0.55 volts and 4 Amperes at their optimum load points for each panel, which is not necessarily the open /short circuit cases.

6.5 Summary

An optically transparent reflectarray integrated with solar cells design procedure has been presented to cover the satellite communications channel (10.7 GHz - 12.7 GHz). Initially, the feed antenna design is presenting through investigating the optimum reflectarray pattern. A conical horn antenna backed by a coaxial cavity and a quarter wave choke rim is designed, fabricated and measured to serve as a center feed for the proposed reflectarray antenna. Also, the reflectarray antenna design exploits stacked perforated acrylic reflectarray unit cell to provide maximum optical transmittance for solar cells. Furthermore, the oblique incidence reflectarray unit cell analysis has been adequately incorporated into the design procedure to provide a more accurate phase shifting representation for the proposed unit cell. A $11.5'' \times 11.5''$ reflectarray prototype backed by the modeled solar cells has been fabricated and measured to prove the proposed concept. The reflectarray antenna provided 26.16 dB at the design frequency with an aperture efficiency of 25% due to the losses in the available commercial acrylic sheets. Of course, the aperture efficiency should improve significantly by using lower loss transparent material(s). Also, the output power from the solar cells has not shown significant change due to the presence of the reflectarray

antenna on top from the uncovered case when the light source is perpendicular to the solar cells/reflectarray aperture surface.

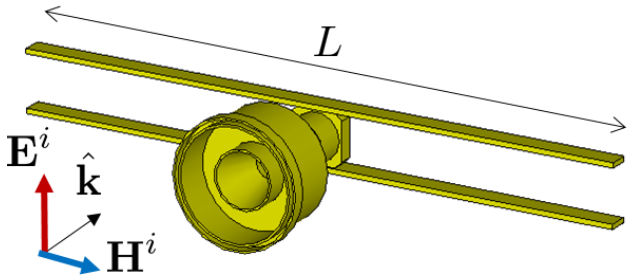

(a)

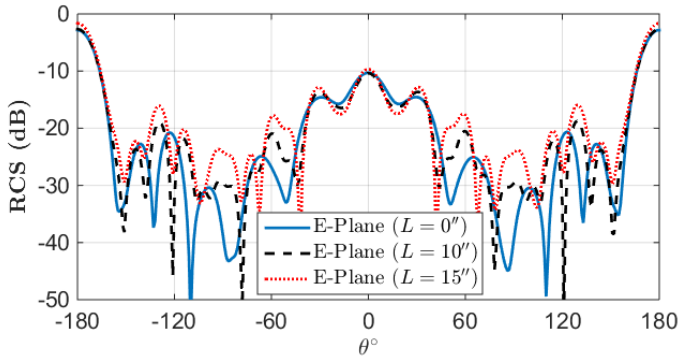

(b)

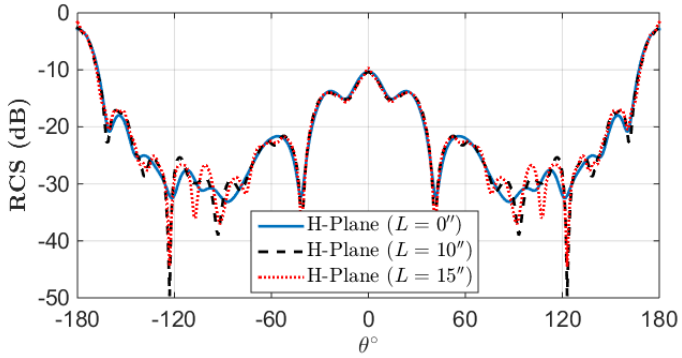

(c)

Figure 6.26: Examining the effect of the struts using plane wave incidence over the feed. (a) Full-wave analysis model indicating the direction and polarization of the incident plane wave. (b) E-plane RCS. (c) H-plane RCS.

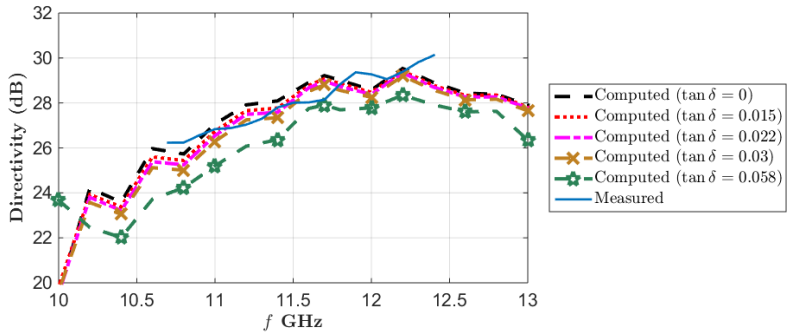

(a)

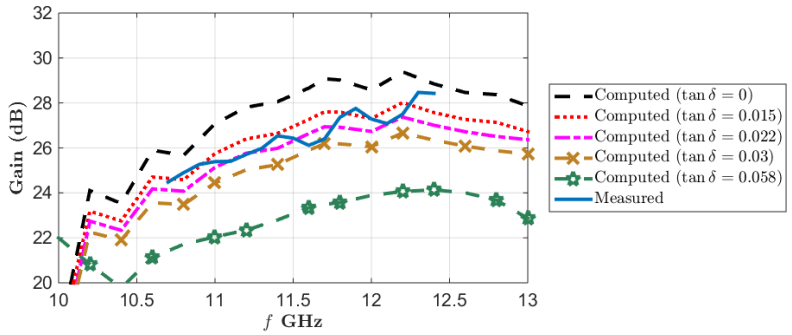

(b)

Figure 6.27: The computed and measured directivity and gain for the proposed perforated acrylic reflectarray removing the solar cells from underneath the acrylic considering different values of the acrylic loss tangent. (a) Direcitivy. (b) Gain.

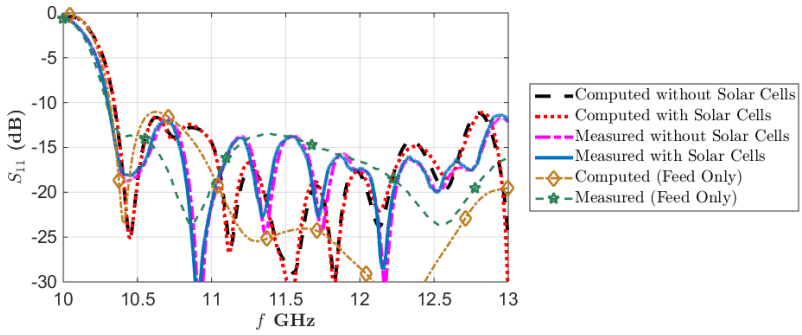

Figure 6.28: The measured and computed reflection coefficient of the whole reflectarray in comparison to the feed only situation.

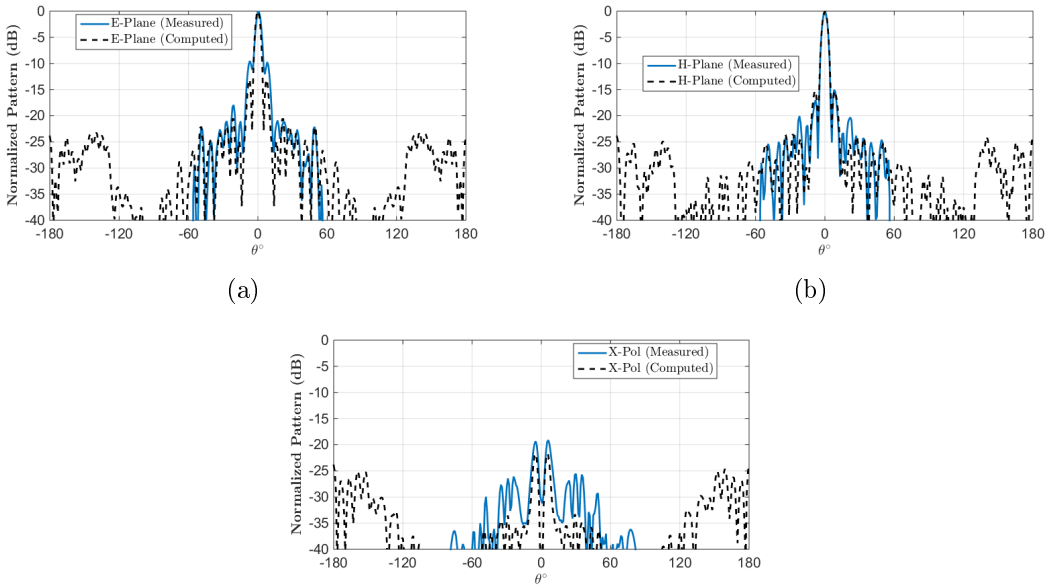

Figure 6.29: The measured and computed normalized radiation pattern of the reflectarray at the design frequency 11.7 GHz. (a) E-plane. (b) H-plane. (c) X-pol.

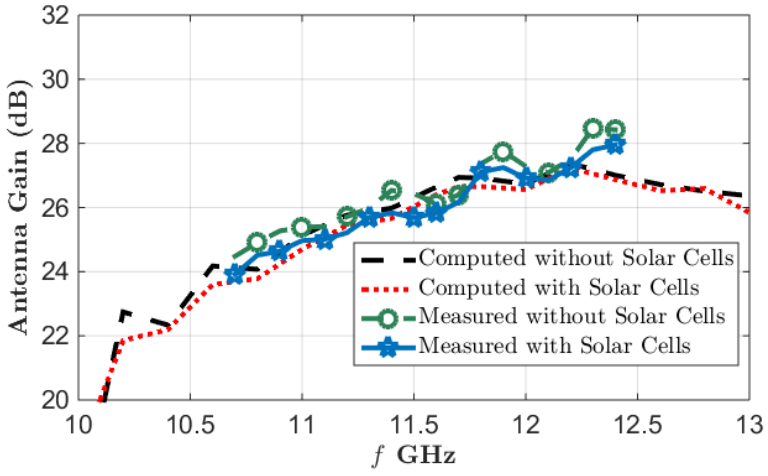

Figure 6.30: A comparison between measured and computed antenna gain.

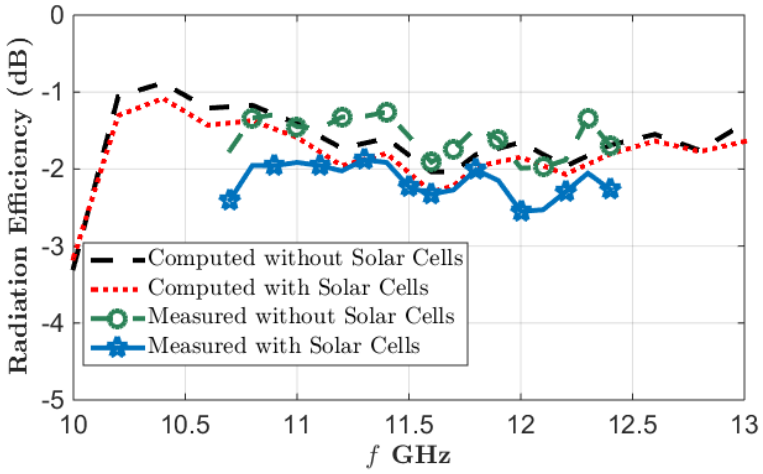

Figure 6.31: A comparison between measured and computed radiation efficiency for the cases with and without solar cells.

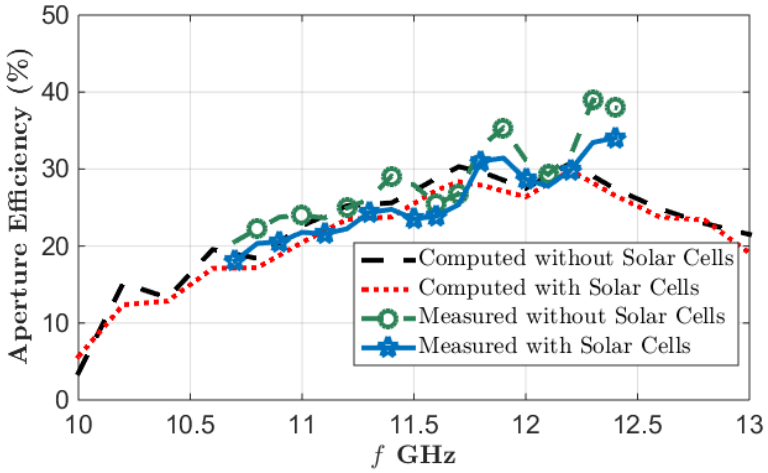

Figure 6.32: A comparison between measured and computed aperture efficiency (η_{ap}).

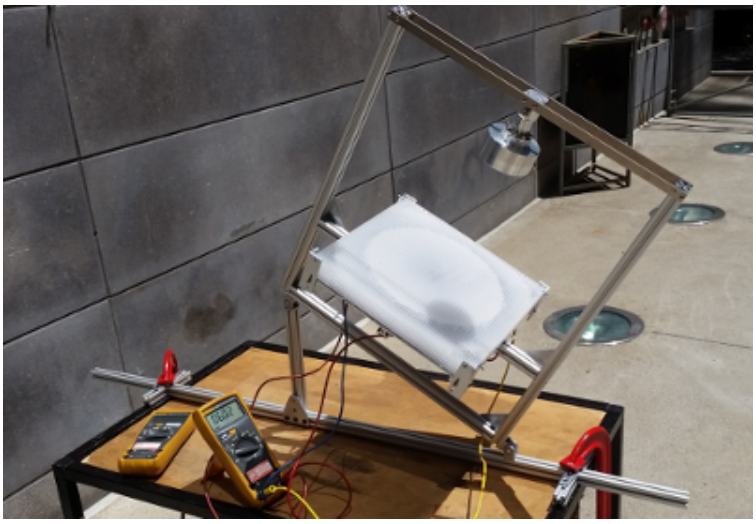

Figure 6.33: The solar power experiment under the sunlight with an angle changing fixture.

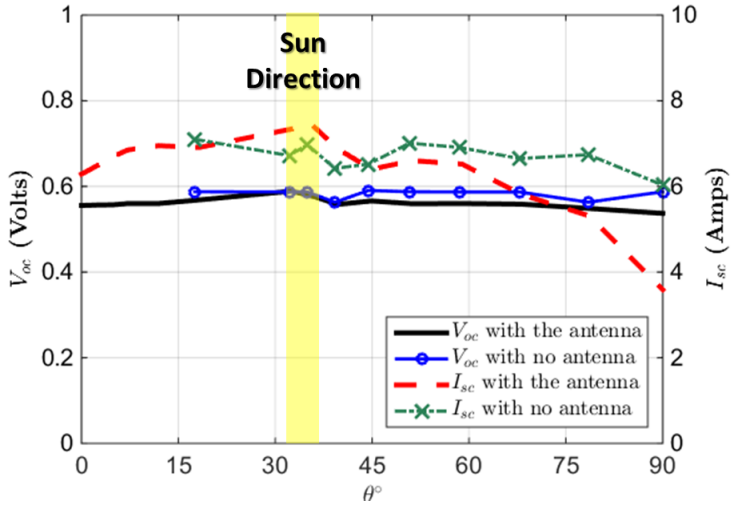

Figure 6.34: The solar power experiment results under the sunlight.

Chapter 7

Conclusions and Future Works

7.1 Conclusions

Modeling solar cells in the microwave range has been presented as anisotropic surface impedance boundaries as inspired from the geometry of the employed solar cells. Two measurement setups have been exploited to characterize the available solar cells based on reflection. The first method used plane wave incidence setup at the Ku frequency band. Measured results could distinguish the anisotropy in the surface impedance. However, the accuracy of the employed setup was not reliable due to the excessive number of sources of error. Thus, a second measurement setup has been proposed using contactless waveguide flanges to measure the required surface impedance in the C and X frequency bands. In addition, the material details of the employed crystalline solar cells have been obtained through an inverse problem following the material permutations available for commercial solar cells. This detailed model developed through the inverse problem could be easily incorporated into full-wave analysis of arbitrary antennas. It was noticed through the model that solar cells behave more likely as a lossy metallic surface.

Furthermore, the radiation efficiency of different antennas in their original environments, including large dielectric substrates and solar cells has been measured using a new design to characterize antennas with solar cells. A novel design of Wheeler caps has been presented implementing the contactless Wheeler cap concept. The proposed design made use of evanescent wave guiding structures to provide the required EM shielding incorporating the antenna's large ground plane environment into the Wheeler cap design. This evanescent wave structure was implemented using cascaded and stacked mushroom-shaped EBG structures for wide band performance. A new EBG unit cell has been presented through this work for compact design for the required shielding flanges. Two different contactless Wheeler caps were designed to cover the frequency band from 1.5 GHz to 40 GHz. In addition, the measured quality factors of the designed Wheeler caps showed relatively high values, which indicated acceptable performance according to the provided error estimation criterion. Nevertheless, an improvement to the quality factor radiation efficiency prediction method has been presented enabling the method to operate in the presence of multiple cavity modes. Several studies have been presented in Appendix A based on numerical and measurement results comparing the proposed improved method to other Wheeler cap post-processing methods. Moreover, verification and test cases using the contactless Wheeler cap designs have been presented to validate the proposed designs and characterize different antennas mounted over solar cells. The presented measurements showed that dielectric resonator antennas can be among the most efficient integration procedures with solar cells because of the minimal interaction with the ground plane materials.

Alternatively, a potentially fast, simple, and efficient electromagnetic numerical analysis technique has been presented solving the scattering and antenna arbitrary problems. The procedure showed a remarkable simplicity in the formulation and flexibility to cover a wide range of boundary conditions and EM problems covering

2D and 3D composite problems. Analytical results for the scattering problem of circular cylinders have been used to verify the proposed technique and prove the concept. Also, arbitrarily shaped scattering problems were used to verify the results and compare performance between the proposed technique and the MoM. In addition, remarkable enhancement in comparison to commercial software packages has been observed in terms of processing time due to the need for less number of unknowns. Furthermore, the procedure has been extended to model antennas by matching their near fields in their radiation and scattering modes for faster post-processing required for reflectarray antenna approximate analysis. Moreover, the approximate analysis results have been improved through implementing the multiple reflections concept, which could fairly predict the reflectarray antenna performance rapidly in comparison to full-wave commercially available software packages.

In addition, incorporating the developed models for the solar cells into the design procedure of reflectarray antennas has been presented through the design process of an optically transparent reflectarray antenna integrated with solar cells. Initially, an inverse problem approach has been conducted to analytically synthesize the required radiation pattern from reflectarray feed antennas of arbitrary feeding positions. Then, a realization of the provided concept has been introduced using a coaxial cavity backed conical horn antenna with a chock rim to improve the achievable aperture efficiency of reflectarray antennas given a specific focal distance. Consequently, the custom made reflectarray feed antenna required incorporating the developed RAS/PO-MR approximate analysis to quickly predict the reflectarray antenna performance. The design of the proposed reflectarray antenna made use of stacked perforated transparent acrylic sheets to cover the satellite communications channel (10.7 GHz - 12.7 GHz). Furthermore, the oblique incidence reflectarray unit cell analysis has been adequately incorporated into the design procedure to provide a more accurate phase shifting representation of the employed reflectarray elements. Moreover, a square

aperture ($11.5'' \times 11.5''$) reflectarray antenna prototype backed by a crystalline solar cells has been fabricated and measured to prove the concept presented. The measured reflectarray antenna gain was reported to be 26.16dB at the design frequency, which corresponded to an aperture efficiency of 25%. This low aperture efficiency value was because of the high loss tangent in the available commercial acrylic sheets. In terms of solar harvesting capability, the solar cell has not shown significant change due to the presence of the reflectarray antenna on top from the uncovered case when the light source is perpendicular to the solar cells/reflectarray aperture surface.

7.2 Major Contributions

The major contributions presented in this thesis can be summarized into several topics. The list below describes the contributions related to each topic with the related publications as listed after the bibliography chapter.

Solar Cells Modeling

1. Characterizing the solar cells behavior in RF as anisotropic surface impedance through measurements [J-S-1].

2. Obtaining the material properties of the crystalline solar cell through an inverse problem [J-S-1].

Antennas Radiation Efficiency Measurement

1. Improving the Q-factor method to be able to use the Wheeler cap method with larger cavities to measure the radiation efficiency of arbitrary antennas [C-4].

2. Introducing the contactless Wheeler cap concept and develop measurements

setups to measure the radiation efficiency of antennas within their original environments [C-3] and [C-2].

3. Measuring the radiation efficiency of different antennas mounted over solar cells with the developed tools.

The Random Auxiliary Sources Method

1. Providing fast and efficient solutions for the EM scattering problems from arbitrary composite 2D and 3D scatterers [J-2] and [J-1].

2. Providing simple models of antennas in their radiating and scattering modes for fast post-processing [C-A-3].

3. Introducing the multiple reflections concept along with the RAS procedure to approximately predict arbitrary reflectarray antennas' performance [C-A-3].

Reflectarray Feed Antennas

1. Introducing a synthesis approach for optimum reflectarray feed antennas radiation patterns for both center and offset feeding scenarios [C-A-2] and [J-S-3].

2. Designing, prototyping and measuring the coaxial cavity backed conical horn antennas to realize the introduced concept [J-S-3].

Reflectarray Antenna Design Integrated with Solar Cells

1. Incorporating the developed models into the design procedure of a novel optically transparent reflectarray antenna design integrated with solar cells [C-A-1] and [J-S-1].

2. Prototyping and measuring the antenna and solar harvesting performance of the developed pencil beam reflectarray antenna [J-S-1].

7.3 Future Work

Since the scope of the topics presented in this thesis is broad, various ideas can be implemented as extensions to the current work. These ideas can be summarized under each topic as

Antennas Integrated with Solar Cells

1. Developing a low shadowing dielectric resonator antenna array making use of the dielectric image line as a linear feeding mechanism.

2. Designing arbitrary shaped beam optically transparent reflectarray antennas using the introduced perforated acrylic unit cell.

3. Scaling the design procedure and parameters to a higher frequency band and investigate the effect of solar cells on RF at higher frequency bands.

Reflectarray Feed Antennas

1. Designing and prototyping reflectarray antennas exploiting the fabricated feed antennas for offset feeding scenarios. This work is mainly to further prove the potential of the concept presented in this topic.

2. Investigating other techniques to shape the radiation pattern from prime reflectarray feed antennas to reach better performance than presented in this work.

The Random Auxiliary Sources Method

1. Including source models into the numerical analysis procedure to enable the RAS method to solve arbitrary antennas directly.

2. Investigate different possibilities to improve the approximate results from the RAS/PO-MR method in terms of gain value, side lobe levels and bandwidth potential.

3. Implementing new boundary conditions to model periodic surfaces in the EBG region.

Contactless Waveguide Setup

1. Measuring the dielectric constant of thin dielectric materials.

Appendices

Appendix A

Details About the Q-Factor Method

A.1 Introduction

In this appendix, rigorous analysis of the exploited expressions in Chapter 4 is conducted to ensure the suitability of expressions for the covered antenna types within this work. The minimum choice of the measured number of frequency points from the employed network analyzer is discussed to accurately fit the measured responses; especially where a significantly large number of cavity modes exist inside the Wheeler cap. Moreover, controlled environment simulations are conducted to evaluate the cavity modes immunity of the proposed method using different antenna types and Wheeler cap sizes. Furthermore, an aluminum prototype of Wheeler cap is built to measure the radiation efficiency of several antennas using the proposed method with the suggested settings.

A.2 Procedure Stability

This section discusses several concerns related to the proposed method regarding validity of expressions, estimation of error and reproduction of results.

A.2.1 Validity of Expressions Off Resonance

An important concern regarding the proposed method is the validity of the expression away from the resonance frequency. The quality factor is only defined at resonance frequencies, thus using the term of frequency dependent quality factor may not be scientifically adequate. However, the proposed method uses a ratio between quality factors, which has a frequency dependence that can be neglected.

Since the quality factor computation formula is invariant with circuit topology as illustrated in [86], manipulation of a series resonance antenna model can be sufficient to represent other resonator circuits. As shown in Fig. A.1, the input impedance can be represented as a function of angular frequency (ω) as

$$Z_{in}(\omega) = R_r(\omega) + R_l(\omega) + j\omega L + \frac{1}{j\omega C}, \tag{A.1}$$

where R_r and R_l represent the radiation and Ohmic loss resistances, respectively. L and C are the inductance and capacitance values of the assumed series resonance model, respectively. By implementing the Wheeler cap method steps to shortening out the radiation resistance in one measurement and computing the quality factor ratios, one reaches the frequency dependent radiation efficiency using another form of Eq. (4.3) as presented in [86], which can be expressed as

$$\eta_r(\omega) \simeq 1 - \frac{R_l(\omega)}{R_r(\omega) + R_l(\omega)} \frac{\left| jL - \frac{1}{j\omega^2 C} + R_r'(\omega) + R_l'(\omega) \right|}{\left| jL - \frac{1}{j\omega^2 C} + R_l'(\omega) \right|}, \tag{A.2}$$

with the prime denotes derivative with respect to the angular frequency ω.

Typically, at resonance the value of R_r' is zero (or very close to zero due to the effect of the coupling network). The changes within the operating band of the antenna is usually small, which may result in neglecting the term $R_r'(\omega)$ with respect to adjacent terms. The same can be applied to wideband antennas, where the whole

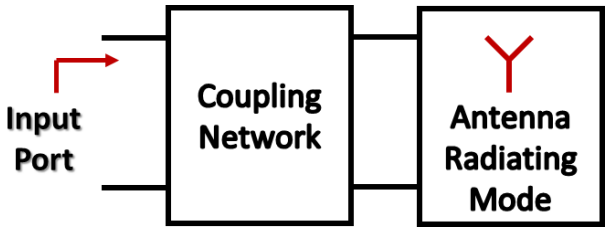

Figure A.1: An illustration for the one port antenna model with the coupling network.

input impedance (or admittance) can be considered almost constant within the operating band. Therefore, it is reasonable to express the frequency dependent radiation efficiency as

$$\eta_r(\omega) \simeq 1 - \frac{R_l(\omega)}{R_r(\omega) + R_l(\omega)}, \tag{A.3}$$

which is a typical expression for the radiation efficiency of a series resonance antenna model. Indeed, the same analysis can be performed for parallel resonance circuits.

The presented analysis concludes that using the quality factors' ratio is valid away from resonance even though individual quality factor values are meaningless. In other words, this method represent just the ratio between the stored energy at any frequency divided by the power losses in the radiation mode to its correspondent in the non radiating mode. This means that the employed procedure actually assumes the stored energy in the radiation mode and non radiating mode are about the same reducing the exploited quality factor ratio to the ratio between the power losses in both modes as presented in [59, 153]. Moreover, using the invariant formula directly from the reflection coefficient can implicitly consider the described advantages without the need for defining circuit models.

A.2.2 Error Estimation

In terms of sources of error in the proposed procedure, it is mainly due to cavity modes. Ideally, in the absence of cavity modes, the most accurate results can be obtained as $\eta_r = 1 - Q_a/Q_w$, where Q_w is the quality factor of the antenna mode

suppressing radiation loss. Alternatively, in the presence of a cavity mode, coupling between the antenna and the cavity mode results in reducing the overall quality factor due to the increase of Ohmic losses, which can be expressed in a similar way as expressed in [154] viz

$$\frac{1}{Q'_w} \simeq \frac{1}{Q_w} + \frac{1}{Q_c}, \tag{A.4}$$

where Q'_w is the overall quality factor of the antenna mode coupled with a cavity mode with unloaded quality factor Q_c. Therefore, the computed radiation efficiency in the presence of a cavity mode (η'_r) can be expressed in terms of the accurate radiation efficiency η_r as

$$\eta'_r = \eta_r - \frac{Q_a}{Q_c}. \tag{A.5}$$

The previous relation predicts that cavity modes' effects always decrease the computed radiation efficiency. Also, the obtained error in the radiation efficiency prediction is a relative quantity which depends on the ratio between the antenna quality factor and the Wheeler cap cavity modes quality factors. This highlights the importance of shielding effectiveness in Wheeler caps to improve the results, besides the importance of using high conductivity materials for the shield. Furthermore, the relative error criterion illustrated in Eq. (A.5) shows that the requirements for the Wheeler cap cavity modes' quality factors vary from antenna type to another. For example, small antennas with narrow bands have high quality factors, thus high quality factors Wheeler caps are recommended to accurately predict radiation efficiency. Alternatively, wide band antennas have low quality factors at their resonances, thus the used Wheeler caps do not necessarily have high quality factors associated with their cavity modes to accurately predict radiation efficiency. Moreover, this criterion indicates that the proposed method is expected to perform better closer to the Wheeler cap cavity resonances although other post-processing techniques may result in unbounded uncertainty in predicting the radiation efficiency [155, 156]. Further

illustrations to the previous statements are presented in Sec. A.3.

Another source of error is related to the dielectric losses inside the antenna body as pointed out in [157]. Besides a possible error due to miscalculations for the antenna quality factor inside the Wheeler cap, some Wheeler cap cavity modes suffer from the same phenomena. This results to have lower values for Q_c in Eq. (A.5), which results to underestimation for the antenna radiation efficiency. A possible solution to the latter problem, as suggested in [157], requires using multiple sized Wheeler caps and/or using a different post-processing procedure to verify sudden changes in the radiation efficiency values. Furthermore, perturbing the coupling mechanism to cavity modes may result in a different error patterns in predicting the radiation efficiency. This perturbation can be performed by using a means of contacltess Wheeler cap, as proposed in [158, 159], that may be discussed in a future publication. Illustration results are presented in Sec. A.3.

A.2.3 Network Analyzer Suggested Settings

To accurately represent the antenna response inside the Wheeler cap by the interpolation routine in Eq. (4.2), a prior knowledge of the number of cavity modes that might be present in the employed frequency band is essential. The modified WeylâĂŹs expression helps to get an asymptotic number of modes in a rectangular cavity with dimensions A, B, and H as a function of frequency (f) [160]. Consequently, the minimum number of points required to accurately represent responses has to include at least M points around each mode across the frequency range between f_l and f_h. Thus, the total number of points P required from the network analyzer is

$$P \sim M\left(f_h - f_l\right) D\left(f_h\right), \tag{A.6}$$

where $D(f_h)$ is the smooth mode density function evaluated at the highest frequency in the band f_h defined in [160] as

$$D(f) = 8\pi ABH\frac{f^2}{c^3} - \frac{A+B+H}{c}. \tag{A.7}$$

where c is the speed of light in the filling medium.

The practical limit of the maximum number of points to be considered is the limit of the network analyzer. Therefore, the first essential task before measuring the antenna radiation efficiency using the proposed technique is to determine the minimum required number of points. This helps to decide either to measure the antenna efficiency in the desired frequency band as a whole or to divide it into smaller sub-bands to preserve the accuracy of measurements. It is worth mentioning here that a minimum number of points associated with each mode (M) are required to be at least three, which is obtained through different trials with the procedures.

Typically, the mentioned criterion to determine the suggested data points works well using discrete frequencies full-wave simulations as offered in HFSS [161]. The main point is to get the required phase span around the resonance frequency of each antenna/cavity mode as suggested in [162]. However, another practical consideration concerning the accuracy of measurements from a vector network analyzer has to be taken into account. A recommended maximum phase shift between adjacent frequency points has not to exceed 12°, which corresponds to a minimum number of data points of 200 per gigahertz of frequency span, per meter of test port cable length as illustrated in [163]. Consequently, the suggested number of frequency points to be used has to satisfy both conditions simultaneously. In addition, increasing the number of points obtained from the network analyzer increases the susceptibility of the fitting equation to measurement noise, which can deteriorate the measurements. In most of the presented measurement results in Sec. A.4, the network analyzer data

points has been maximized making sure that the above criteria are satisfied.

A.2.4 Suitablity of Quality Factor Computations to the Responses

Besides the work presented in [84], which uses the provided expression in Eq. (4.3) to determine the quality factor of antennas (i.e. low quality factors), the suitability of the provided technique requires to be verified for the responses involving coupling to different cavity modes. Consequently, a short 50Ω coaxial probe is used to excite a $100 \times 100 \times 60$ mm^3 cavity made of brass as illustrated in Fig. A.2. The discrete frequency simulation of HFSS [161] provides the reflection coefficient shown in Fig. A.3 (a). By following the recommended settings in Sec. A.2.3, the resulting loaded quality factor values due to the employed expression are compared to the Eigen mode full-wave solver results in Fig. A.3 (b) with good accuracy. Since the exploited coupling mechanism is electric (i.e. short probe), not all of the cavity modes are coupled to the input port. This is shown in the Eigen mode solver solutions that have no match through the expression from Eq. (4.3). The reason behind this is that Eigen mode solver solves without excitation first and then perturbation is applied to get the loaded quality factors. It is worth mentioning that the responses of interest observed through coupling to antennas have less quality factor values, which are easier to capture through Eqs. (4.2) and (4.3).

A.3 Simulation Results

This section provides simulation results in a controlled environment. These simulations enable evaluating the proposed method extensively without any fabrication or measurement tolerance effects. Therefore, different antenna types are exploited in the coming subsections to evaluate the potential of using the proposed method. Also,

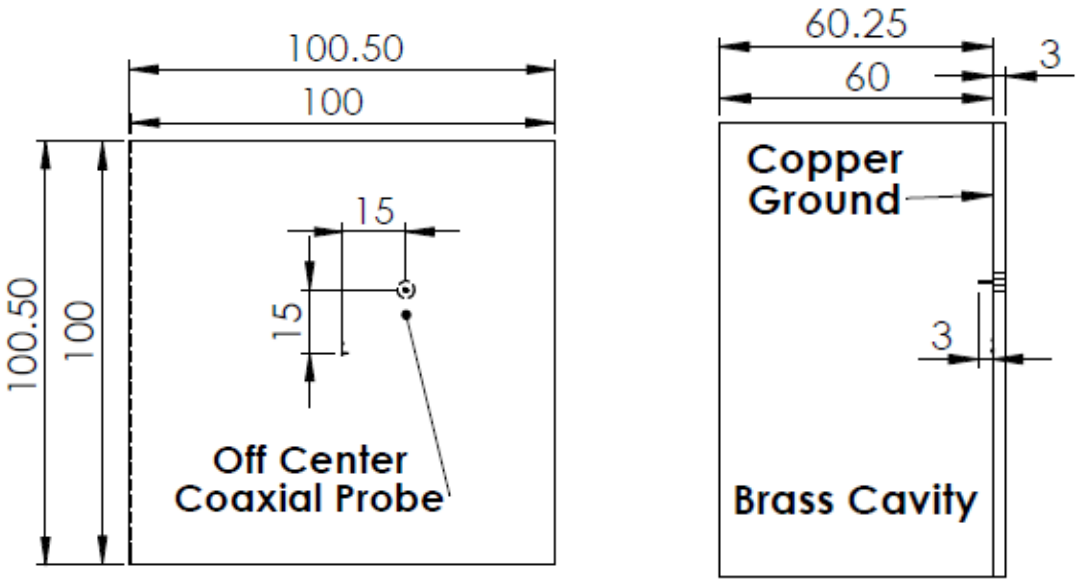

(a) (b)

Figure A.2: Response validation simulation setup details with all dimensions in millimeter. (a) Front view. (b) Side view.

the same antennas' simulation results are used in comparison with related works in Appendix A.5.

A.3.1 Dual Band Antenna

A dual band antenna is presented using an optimized E-Shaped patch antenna as introduced in [164]. The structure of the antenna is shown in Fig. A.4. Accordingly, using different size Wheeler caps to predict the radiation efficiency of the antenna with the proposed method leads to the results in Fig. A.5 (b) for the simulated responses in Fig. A.5 (a). Although using various Wheeler cap sizes results in different cavity modes coupled to the antenna, minimal changes around the full wave analysis results are observed (within 0.5%).

The E-Shaped patch antenna resonates at two frequencies, 1.749 and 2.362 GHz. The corresponding quality factor values computed by Eq. (4.3) are 16.79 and 6.816,

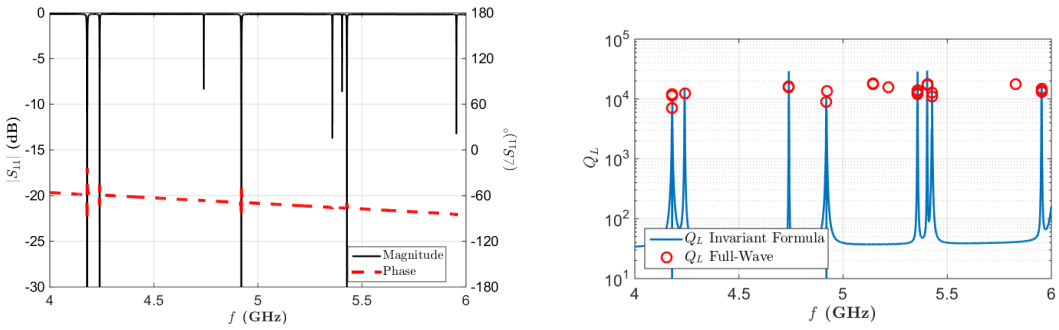

(a) (b)

Figure A.3: Computed reflection coefficients and loaded Q-factor of the cavity illustrated in Fig. A.2. (a) Simulated reflection coefficient. (b) Comparison between the computed quality factor using Eq. (4.4) and the full-wave Eigen-mode solver results with perturbations.

respectively. These slightly low quality factor values justify the slight changes in the predicted radiation efficiency as estimated through Eq. (A.5) considering the high quality factor cavity modes inside the Wheeler cap.

A.3.2 Wide Band Antenna

A U-Shaped dielectric resonator antenna (DRA) is employed featuring 40% percentage bandwidth. Using the antenna configuration illustrated in Fig. A.6, the simulated reflection coefficients for the antenna in free-space and inside different sizes of Wheeler caps are presented in Fig. A.7 (a). The reflection coefficient responses show the dense presence of cavity modes inside the simulation frequency band. The processed radiation efficiency results are presented in Fig. A.7 (b) in comparison to the full-wave analysis results. The results show good immunity to the presence of the majority of cavity modes using the proposed Q-factor method with differences in the order of 1%. However, some discrepancies in the results are shown in the results are related to cavity modes interacting with the dielectric losses of the antenna, which result in underestimating the antenna radiation efficiency as shown in Sec. A.2.2. As shown through using different Wheeler cap sizes, the actual trend of the antenna radiation

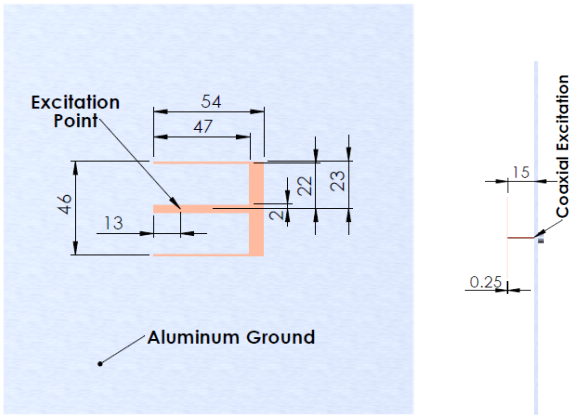

(a) (b)

Figure A.4: The E-Shaped patch antenna structure and dimensions (in millimeter). (a) Front view. (b) Side view.

efficiency can be depicted through the graphs. Furthermore, These results comply with different DRAs, which are known for their high radiation efficiency (close to 100%) [46, 93].

It is important to highlight that the proposed Q-Factor method exhibits minimal changes with the presence of cavity modes due to the low quality factor values of the radiating modes. The antenna has two radiating modes with resonance frequencies 3.833 and 5.06 GHz and quality factor values 2.756 and 2.565, respectively. This ensures minimal effects for the cavity modes on the measurements according to Eq. (A.5) for a Wheeler cap with quality factor values > 10000.

A.3.3 Small Antenna

Here, we consider the EZ small antenna as proposed in [165] and shown in Fig. A.8. The simulated antenna responses in free-space and inside different Wheeler caps are shown in Fig. A.9 (a). Using the proposed Q-Factor method, the predicted radiation efficiency values for the different cavity sizes are presented in Fig. A.9 (b) compared with the full-wave simulation. It is noticed that using different cavity sizes resulted in different radiation efficiency values (within 4%). Also, inaccurate prediction of

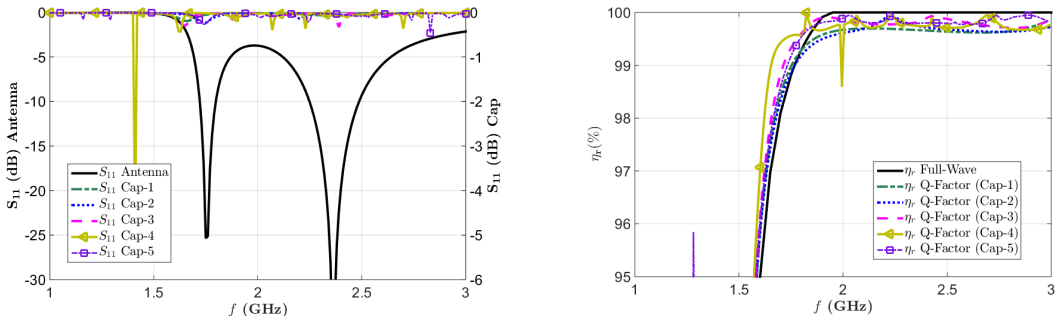

(a) (b)

Figure A.5: Simulated reflection coefficients and computed radiation efficiency for the E-Shaped patch antenna illustrated in Fig. A.4. (a) Simulated reflection coefficients for the antenna in free-space and inside different Wheeler caps. (b) Computed radiation efficiency. Here, Cap-1 has dimensions $110 \times 110 \times 50$ mm^3, Cap-2 $150 \times 150 \times 50$ mm^3, Cap-3 $110 \times 110 \times 100$ mm^3, Cap-4 $150 \times 150 \times 100$ mm^3 and Cap-5 $165 \times 165 \times 82$ mm^3.

(a) (b)

Figure A.6: The U-Shaped DRA structure (dimensions in millimeter). (a) Front view. (b) Side view.

the antenna radiation efficiency is observed (e.g. results for Cap-2 and Cap-5). This happens when the antenna mode is greatly loaded by the Wheeler cap, as presented in the responses in Fig. A.9 (a), due to the closeness of the antenna mode to a cavity mode. These loading situations are mainly related to the cavity modes and not to the Wheeler cap size, as the Wheeler cap recommended dimensions [63] are respected through the different simulations. It is also noticed that although the results for Cap-1, Cap-3 and Cap-4 have a slight frequency shift between the loaded and unloaded resonance frequencies, acceptable results are achieved. These varying results also line up with the findings in [157] regarding systematic overestimating the radiation efficiency of antennas using the Q-Factor method (*or the Complementary Quality*

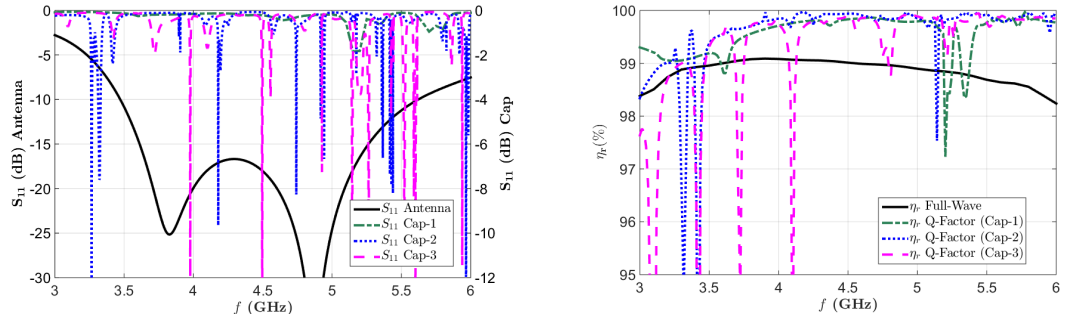

(a) (b)

Figure A.7: Simulated reflection coefficients and computed radiation efficiency for the U-Shaped DRA given in Fig. A.6. (a) Simulated reflection coefficients for the antenna in free-space and inside different Wheeler caps. (b) Computed radiation efficiency. Here, Cap-1 has dimensions $65 \times 65 \times 31$ mm^3, Cap-2 $100 \times 100 \times 60$ mm^3 and Cap-3 $120 \times 120 \times 31$ mm^3.

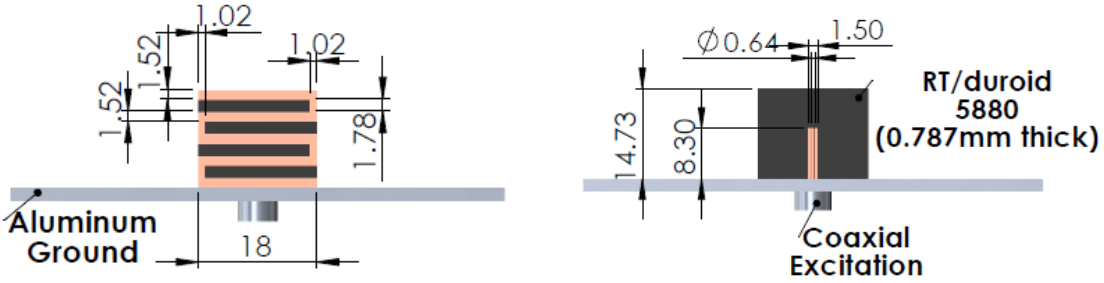

(a) (b)

Figure A.8: The EZ small antenna structure and dimensions (in millimeter). (a) Front view. (b) Back view.

Factor Method as the terminology in [157]). Using different cavity sizes is the way to go to overcome this kind of systematic error [157].

The presented antenna has a resonance frequency of 1.39 GHz with estimated quality factor of 34 according to Eq. (4.3). This gives an insight view about the estimated error using the proposed Q-Factor method for such an antenna type. Of course, the relation in Eq. (4.3) is true for valid responses as seen in Fig. A.9 (b) for Cap-1, Cap-3 and Cap-4.

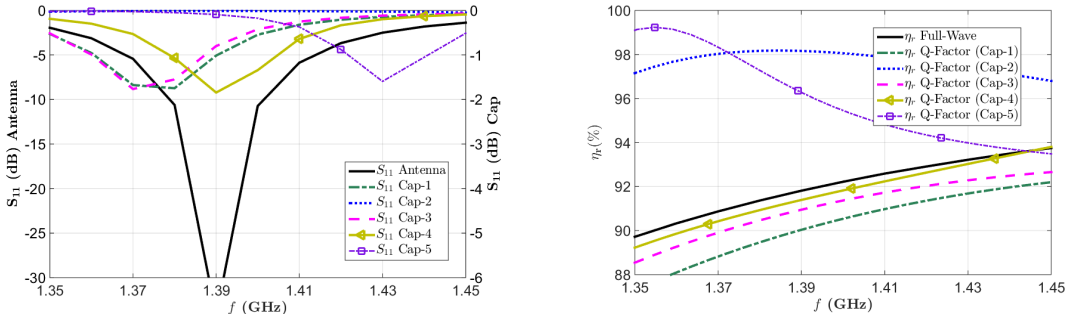

(a) (b)

Figure A.9: Simulated reflection coefficients and computed radiation efficiency for the EZ small antenna illustrated in Fig. A.8. (a) Simulated reflection coefficients for the antenna in free-space and inside different Wheeler caps. (b) Computed radiation efficiency. Here, Cap-1 has dimensions $114\times114\times63$ mm^3, Cap-2 $150\times150\times63$ mm^3, Cap-3 $114\times114\times100$ mm^3, Cap-4 $175\times175\times150$ mm^3 and Cap-5 $200\times200\times175$ mm^3.

A.4 Measurement Results

The employed measurement setup consists of an aluminum ground plane and rectangular Wheeler cap with 32 fixing holes as shown in Fig. A.10. The Wheeler cap inside dimensions are $119\times119\times54$ mm^3. These dimensions were chosen to accommodate the various antennas presented in this work.

The first example is presented for different length monopole antennas. A 6-mm vertical monopole antenna is measured through the Wheeler cap setup giving the measured reflection coefficients presented in Fig. A.11 (a) for the antenna in free-space and inside the Wheeler cap. The adaptive fitting procedure is used to fit the Wheeler cap response within 340 frequency segments for a square error level of 1E-4. It is obvious that the monopole antenna couples to a huge number of cavity modes. The predicted radiation efficiency is shown in Fig. A.11 (b) in comparison to the full-wave analysis of CST [108]. Two percent difference in the radiation efficiency values is observed across the measured frequency band. This discrepancy is different from the results of HFSS, which is referred to the accuracy of calculating the radiation

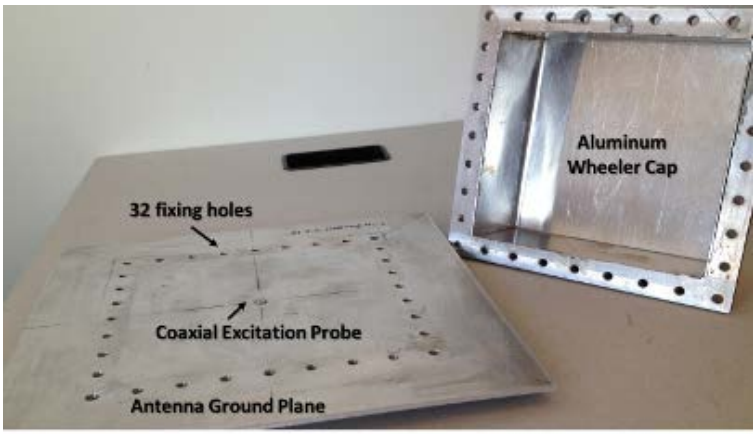

Figure A.10: The Wheeler cap measurement setup for antennas with vertical ground planes.

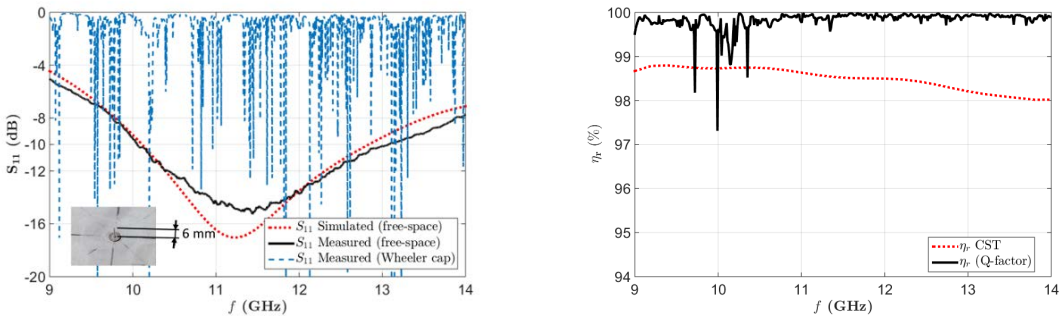

(a) (b)

Figure A.11: The measured and processed results for the 6 mm vertical monopole antenna. (a) Measured reflection coefficients. (b) Predicted radiation efficiency compared with the full-wave prediction.

efficiency in both simulators. However, the results are in the same order more-or-less and fair enough for the Wheeler cap 'approximate' method given the dense presence of cavity modes through the measurements. Moreover, the same setup is used to measure the radiation efficiency of a 11-mm vertical monopole, which resonates at a different frequency. The measured reflection coefficients for the antenna in free-space and inside the Wheeler cap are shown in Fig. A.12 (a). The adaptive procedure required 59 segments to fit the given response to the accuracy of 1E-5. Undesired leakage is observed near the 5.2 and 6.2 GHz frequencies due to the insufficient number of screws to shield the antenna under the cap.That results in inaccurate prediction

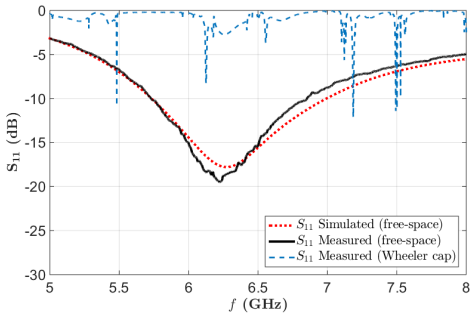

(a)

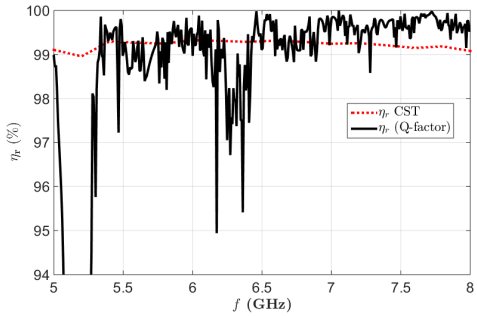

(b)

Figure A.12: The measured and processed results for the 11 mm vertical monopole antenna. (a) Measured reflection coefficients. (b) Predicted radiation efficiency compared with the full-wave prediction.

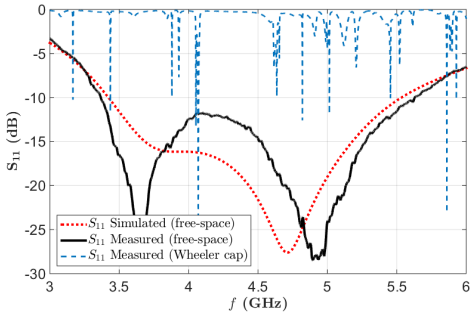

(a)

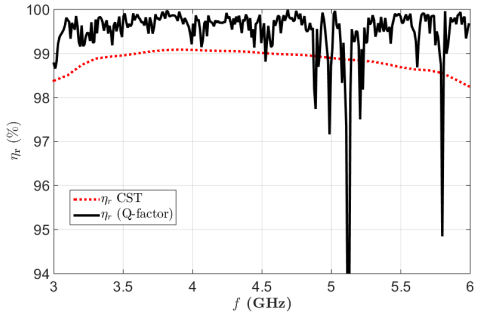

(b)

Figure A.13: The measured and processed results for the U-Shaped DRA shown in Fig. A.6. (a) Measured reflection coefficients. (b) Predicted radiation efficiency compared with the full-wave prediction.

of the radiation efficiency near these frequencies. However, the predicted radiation efficiency, away from the leakage regions, follow the simulated results for the same problem in CST as shown in Fig. A.12 (b).

The second example exploits the U-Shaped DRA, illustrated in Fig. A.6, using the Wheeler cap setup. The measured reflection coefficients for the antenna in free-space and inside the Wheeler cap are shown in Fig. A.13 (a) showing a dense presence of cavity modes. The adaptive fitting procedure required 37 frequency segments to fit the response of the Wheeler cap within a square error tolerance of 1E-5. It is observed that leakage occurs around the frequency 5.2 GHz in a similar way as the previous

(a) (b)

Figure A.14: The structure of the compact wideband stacked circular DRA [166]. (a) Prospective view. (b) Top view.

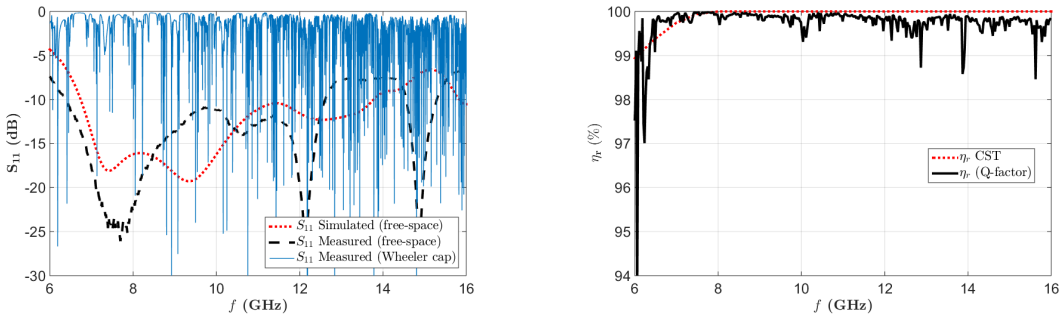

(a) (b)

Figure A.15: The measured and processed results for the compact wideband stacked DRA shown in Fig. A.14. (a) Measured reflection coefficients. (b) Predicted radiation efficiency compared with the full-wave prediction.

example. However, the processed radiation efficiency shows good agreement with the simulated results (within 2%) because of the relative very low antenna quality factor as compared to the cavity modes' quality factors.

The final example is for circular wideband stacked DRA, that is presented in [166]. The structure of the antenna is presented in Fig. A.14 with dimensions: $R_a = 7$ mm and $A = 3.7$ mm to covers the frequency range from 6.7 to 13.7 GHz.. The multilayer structure has the bottom layer with $h_3 = 2.5$ mm and $\varepsilon_r = 6.15$, middle layer with $h_2 = 3.35$ mm and $\varepsilon_r = 2.33$, and the top layer with $h_1 = 2.5$ mm, and $\varepsilon_r = 10.2$. This Wheeler cap is considered very large for this antenna. Thus, one would expect that it will not be possible to predict the radiation efficiency. The measured reflection coefficients of the antenna in free-space and inside the Wheeler cap are shown in Fig.

A.15 (a) showing very dense cavity modes coupled to the antenna. The adaptive fitting procedure required 585 frequency segments to accurately fit the measured Wheeler cap response within the tolerance level of 1E-3. The predicted radiation efficiency is shown in Fig. A.15 (b) in comparison to the full-wave results showing very good agreement and minimal effects due to the presence of cavity modes. It is also noted that leakage around 6.2 GHz affects the predicted radiation efficiency as shown in the previous example.

A.5 Comparison to Related Works

This appendix provides results for the other circuit model independent procedures, namely: IWC [73, 74] and MWC [78], using the same responses obtained in Sec. A.3. Simulation results are used to avoid fabrication and measurement tolerance. This aims to highlight the strength and weakness of these methods in comparison to the proposed method for different antenna types.

A.5.1 The Improved Wheeler Cap Method (IWC)

Using the responses presented in Sec. A.3, the IWC is used to predict the radiation efficiency of different antenna types in the same formulation as [73, 74]. The results of the dual band E-Shaped antenna is presented in Fig. A.16, the wide band DRA is presented in Fig. A.17 and the EZ small antenna is presented in Fig. A.18.

The presented results show that the IWC method is best for narrow band antennas as the case of the small antenna as shown in Fig. A.18 with tolerance ∼2%. In the case of wide band or dual band antennas, the losses in the cavity modes are averaged with the losses inside the antennas, resulting in an underestimation of the radiation efficiency as presented in Figs. A.16 and A.17. The deterioration of the results using the IWC depends on the density of cavity modes within the operating frequency band.

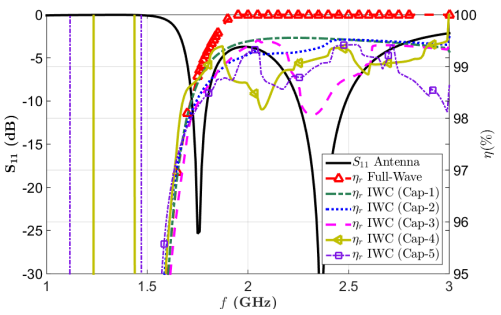

Figure A.16: The radiation efficiency of the E-Shaped patch antenna illustrated in Fig. A.4 computed by the IWC method using the same responses presented in Fig. A.5 (a).

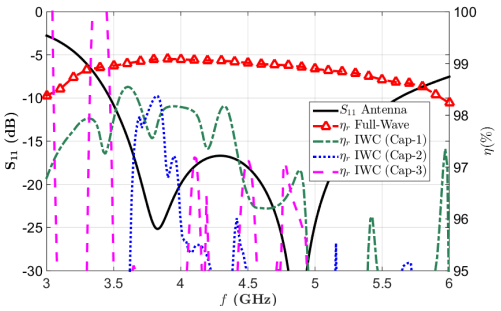

Figure A.17: The radiation efficiency of the U-Shaped DRA illustrated in Fig. A.6 computed by the IWC method using the same responses presented in Fig. A.7 (a).

A.5.2 The Modified Wheeler Cap Method (MWC)

Processing the simulated responses in Sec. A.3 by the MWC procedure [78] resulted in different prediction of the radiation efficiency. The results of the dual band E-Shaped antenna is presented in Fig. A.19, the wide band DRA is presented in Fig. A.20 and the EZ small antenna is presented in Fig. A.21.

The results show that the MWC is not suitable for small antennas as seen in the huge difference in Fig. A.21 as it is originally developed for ultra wide band antennas [76]. Also, the method provided very good results for the dual band E-Shaped patch antenna as presented in Fig. A.19, where cavity modes in all the cases are weakly coupled to the input port as presented in Fig. A.5 (a). As coupling level increases, the accuracy of the method deteriorates in comparison to the proposed Q-factor method as shown in Fig. A.20. It is important to illustrate that the MWC

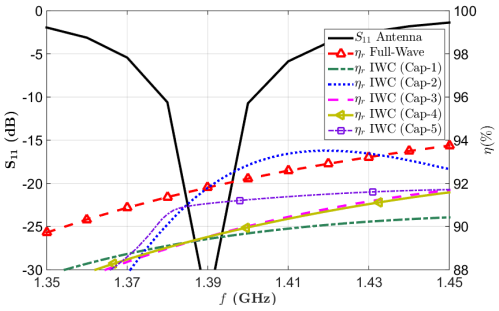

Figure A.18: The radiation efficiency of the EZ small antenna illustrated in Fig. A.8 computed by the IWC method using the same responses presented in Fig. A.9 (a).

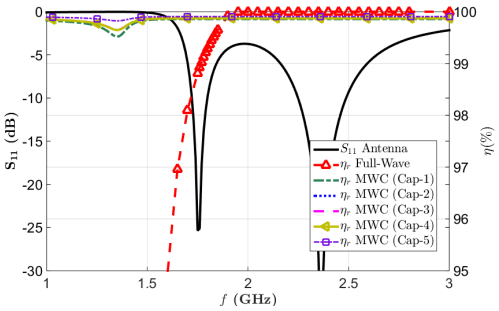

Figure A.19: The radiation efficiency of the E-Shaped patch antenna illustrated in Fig. A.4 computed by the MWC method using the same responses presented in Fig. A.5 (a).

method relies on the envelope of the response containing cavity modes effects as presented in [76, 78]. So, further processing is required to have smooth curves as featured in the IWC.

A.6 Summary

A new study over the Q-Factor radiation efficiency estimation method with Wheeler caps has been conducted. The detailed radiation efficiency prediction procedure has been introduced with rigorous analysis to the validity of the expressions for wideband prediction. Also, the stability measures for the proposed Q-Factor method have been introduced featuring a rigorous determination for the network analyzer minimum number of points to be used for repeatable results. Moreover, simulation results

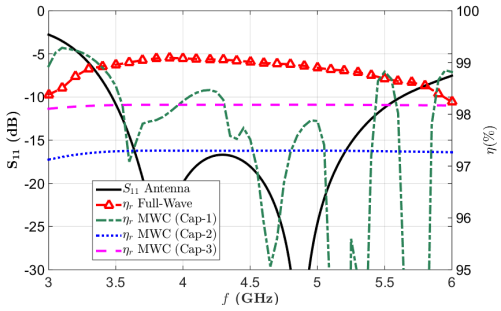

Figure A.20: The radiation efficiency of the U-Shaped DRA illustrated in Fig. A.6 computed by the MWC method using the same responses presented in Fig. A.7 (a).

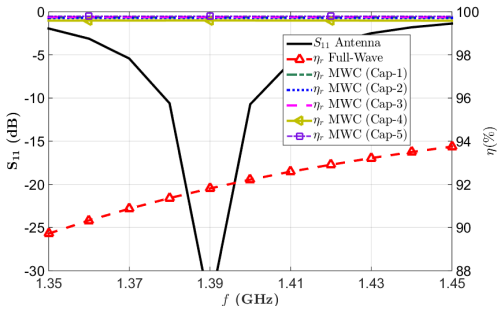

Figure A.21: The radiation efficiency of the EZ small antenna illustrated in Fig. A.8 computed by the MWC method using the same responses presented in Fig. A.9 (a).

have been presented for various scenarios to examine the immunity of the proposed method for effects of Wheeler cap cavity modes in comparison to other circuit model independent radiation efficiency prediction procedures. Measurement results have been presented for various antennas to verify the applicability of the proposed method and verified with full-wave analysis.

Appendix B

EM Scattering Problems Results Generated by the RAS Method

A comparison of the execution time consumed by the proposed technique to the commercially available software CST can be used as a benchmark of the performance. The scattering problem from conducting spheres with different radii can be a good example to elaborate the speed that can be obtained from RAS when compared to the commercially optimized software. Table B.1 shows this comparison with different acceleration procedures of the MoM technique (i.e. direct MoM solver, iterative MoM solver (I-MoM), and MLFMM technique). Also, the results are presented in Fig. B.1 with the complexity lines for the used methods. The results show, for smooth structures, a superiority of the RAS technique to MoM, but MLFMM is more superior for large problems. The crossover between the proposed RAS method and MLFMM can be depicted to be around the case with $2\lambda_0$ radius. Furthermore, it is important to highlight that RAS and CST-Integral Equations Solver use a different number of testing points and consequently different number of unknowns. Table B.2 shows the employed number of testing points/surfaces for both methods and the number of randomly generated sources' positions per iteration for the RAS method. These

results show the potential in the proposed method to solve electromagnetic scattering problems with less number of unknowns and consequently less memory requirements as presented in Sec. 5.5.5. On the other hand, a worst scenario performance of the proposed technique can be quantized by comparing the required time to solve problems with edges (i.e. hexahedrons and cylinders) as shown in Table B.3. The presented results are considered the worst case performance of the RAS technique in terms of execution time, where the structure contains a large number of edges. The smoother the structure is, the better the performance observed by RAS in terms of required number of iterations and execution time. The used hexahedron has dimensions $2\lambda_0 \times 2\lambda_0 \times 1\lambda_0$ and the cylinder has a radius of $1\lambda_0$ and height of $2\lambda_0$. A comparison between the employed testing points by the proposed RAS procedure with the required random and fixed edge correction sources and the MoM surfaces generated by CST-Integral Equations Solver is presented in Table B.4. The presented results show that the RAS procedure requires a much less number of unknowns per-iteration than equivalent commercial MoM codes. Moreover, the presented results show that the worst case performance is slightly comparable to the direct MoM, which means that using the proposed RAS technique can be generally advantageous to MoM and I-MoM. However, it is important to mention that the developed FORTRAN code utilizes only a single core processing. Therefore, to prove the concept, the CST-IE solver is limited to a single core processing with double precision to have a fair comparison with the performance with the developed code. However, it is important to notice that the comparison is made here between a commercially developed software written by professionals and a research based code, which indeed needs a lot of improvements for faster and resource efficient flow.

A more insightful point on the current implementation of the proposed RAS technique can be presented by comparing the execution time of filling and solving the RAS matrices as shown in Table B.5 and Fig. B.2. These results elaborate that

Table B.1: A comparison between the execution time of the proposed technique and CST-Integral Equation solver for conducting spheres with different radii [112] ©2015 IEEE.

Radius (λ_0)	RAS time (s)	MoM time (s)	I-MoM time (s)	MLFMM time (s)
0.5	0.015	2	6	1
1.0	0.17	9	33	4
2.0	8.82	185	194	18
4.0	604.7	41612	1597	89

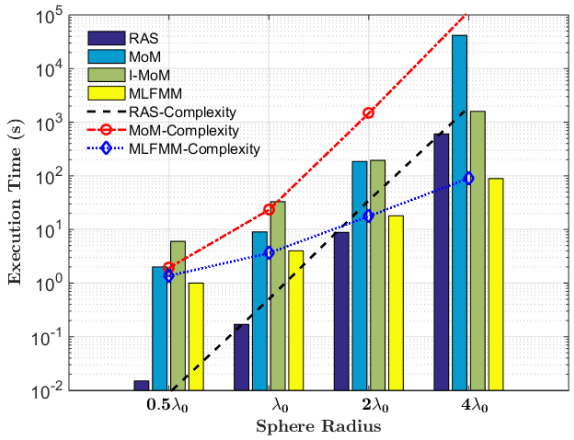

Figure B.1: The execution time of proposed RAS method in comparison with MoM, I-MoM, and MLFMM solving PEC spheres with different radii [112] ©2015 IEEE.

filling time actually takes more time than the matrix solution time for the relatively small structures, where the pre-asymptotic complexity of the procedure is effective. The linear algebra tends to be more dominant for larger objects, as presented for the $5\lambda_0$ radius sphere with SPW $= 5$. Also, since the number of unknowns is constant for each problem as a consequence of evaluating Eq. (5.9), the filling time of high sampling rate per wavelength is much longer than the one with a lower sampling rate.

Using the IFB procedure or domain decomposition technique along with the RAS technique for multi-object scattering problems can improve the solution speed tremendously. Figs. B.3 (a) and B.3 (b) show two different problems involving multiple scatterers with all geometry details and excitation angles shown in the Figures. The scattered electric fields of these problems are compared to CST-IE in Figs. B.4 (a)

Table B.2: A comparison between the required number of testing points and unknowns of the proposed technique and CST-Integral Equation solver for conducting spheres with different radii [112] ©2015 IEEE.

Radius	RAS		MoM
(λ_0)	Testing Points (M)	$N^i_{g,j}$	Surfaces
0.5	86	24	212
1.0	332	92	487
2.0	1299	386	1942
4.0	5068	1448	8324

Table B.3: A worst case comparison between execution times of the proposed technique and CST-Integral Equation solver for a conducting hexahedron and cylinder [112] ©2015 IEEE.

Structure	RAS time (s)		MoM	I-MoM	MLFMM
	$8/\lambda$	$10/\lambda$	time (s)	time (s)	time (s)
Cylinder	16.3	33	98	287	15
Hexahedron	59.18	68.11	61	180	9

and B.4 (b), respectively, with a very good agreement. A comparison between the executed times by the RAS-IFB method and CST-IE are presented in Table B.6. The problem illustrated in B.3 (a) is a moderate size problem involving a dielectric hexahedron with a low dielectric constant (i.e. No edge correction is needed for this problem). This resulted in a faster response of the RAS-IFB method compared to all the other alternatives. On the other hand, the problem presented in B.3 (b) consists of different PEC geometries, each needs a special edge correction procedure through the solution procedure. Moreover, this problem is considered relatively large. The solution performance indicates that the RAS-IFB method is superior to MoM and I-MoM, but the MLFMM technique is faster in this case.

Through the different examples presented in this work, a major key fact can be depicted from the performance results. The presented RAS method, making use of the inherent properties of the method to accelerate solutions, is very much competing the MoM in terms of memory and execution time. However, for large problems the proposed method fails to be faster in comparison with the MLFMM, which indeed

Table B.4: A comparison between the required number of testing points and unknowns of the proposed technique and CST-Integral Equation solver for a conducting hexahedron and cylinder [112] ©2015 IEEE.

Structure	RAS				MoM
	SPW	M	$N^i_{g,j}$	$N^i_{g,j}$ (Fixed)	Surfaces
Cylinder	8	1330	148	102	704
	10	2026	144	102	
Hexahedron	8	2008	223	160	584
	10	2958	211	160	

Table B.5: Execution time distribution between filling and solving the RAS matrices for conducting spheres of different sizes [112] ©2015 IEEE.

Radius (λ_0)	Surface Area (λ_0^2)	RAS ($5/\lambda$) time (s)		RAS ($10/\lambda$) time (s)	
		filling	solving	filling	solving
1.0	4π	0.1	0.04	0.42	0.031
2.0	16π	5.44	3.08	20.63	2.98
3.0	36π	53	50.77	205.6	48.6
4.0	64π	303.6	289.6	1234.4	289.6
5.0	100π	1075.4	1223.95	4289.18	1223.95
6.0	144π	3221.45	3859.54	12620	3756

uses a leveled approximation procedure [167]. The RAS method does not use such approximation, but it operates in a similar procedure as MoM. So, given this current performance of the proposed technique, one can anticipate faster operations if adequate higher order parameters and approximation schemes are used in similarity to MLFMM. These methods can reduce the time required to fill the matrices, which is always larger than the time required to decompose these matrices as presented in Table B.5 for a pre-asymptotic complexity operation. Therefore, using acceleration techniques offered in the fast methods class can, in turn, improve the solution time tremendously. Also, as the size of structure increases and consequently the size of matrices to invert, the asymptotic complexity of the linear algebra performed by the Cholesky decomposition becomes dominant. Therefore, using other acceleration methods is required to speed up the matrix solution becomes essential.

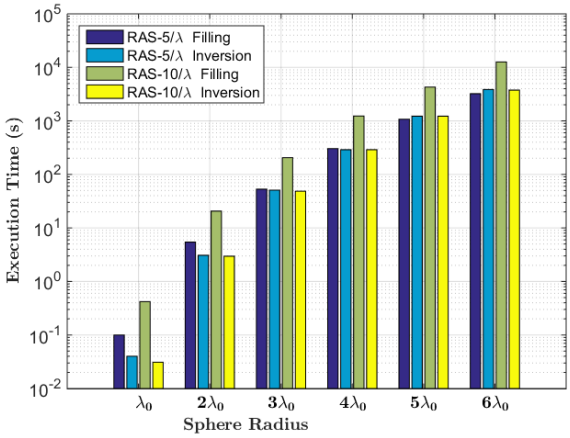

Figure B.2: Filling and inversion time of the RAS method solving PEC spheres with different radii with different surface sampling criteria [112] ©2015 IEEE.

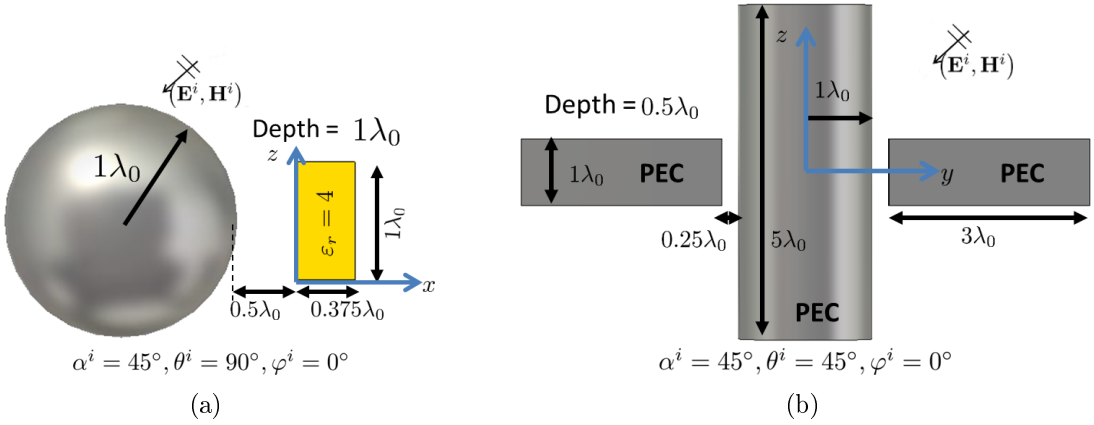

Figure B.3: Different problems involving multi-object scattering problems [112] ©2015 IEEE.

Table B.6: Execution time comparison between RAS-IFB and CST-IE for the problems illustrated in Fig. B.3 [112] ©2015 IEEE.

Problem Figure	RAS-IFB time (s)	MoM time (s)	I-MoM time (s)	MLFMM time (s)
B.3 (a)	129.62	631	968	199
B.3 (b)	307	1541	980	48

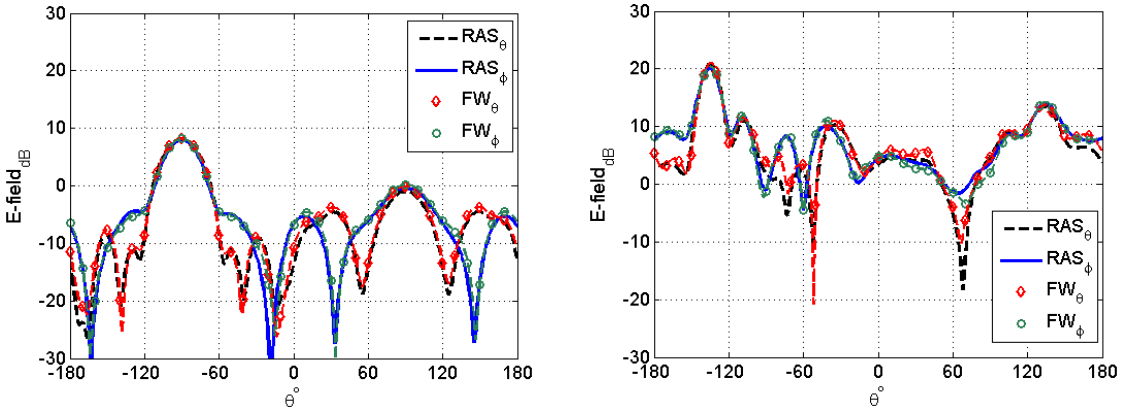

Figure B.4: Scattering far fields of the problems shown in Fig. B.3 with the same order. The IFB method took 3 and 2 iterations for the solution in (a) and (b), respectively [112] ©2015 IEEE.

Appendix C

Reflectarray Optimized Offset Feeding Antennas

As presented in Eq. (6.2) and Fig. 6.2 (b), more suitable antenna feeds for the offset feeding scenario exist by having pattern tapering to compensate for the difference in path losses over the reflectarray aperture. The proposed solution is to taper the horn antenna aperture to disturb the phase aperture. This causes the pattern to be tapered along the physical tapering in the horn. Exploiting the optimized design in Fig. 6.5, tapering is implemented in different situations to evaluate the performance of reflectarrays under offset feeding scenarios in comparison to a conical horn antenna.

C.1 Tapering the Coaxial Cavity

The first proposed solution is to taper the coaxial cavity of the optimized design in Fig. 6.5 with an arbitrarily chosen angle α_t as presented in Fig. C.1 with $\alpha_t = 10°$. The tapering is chosen to maintain the exact optimized dimensions for the non-tapered plane (i.e, the height of the coaxial cavity is increased from one side and decreased from the other side of the tapering). Careful design and adjustment to the fixing holes in the back of the horn antenna part to enable aligning the tapering

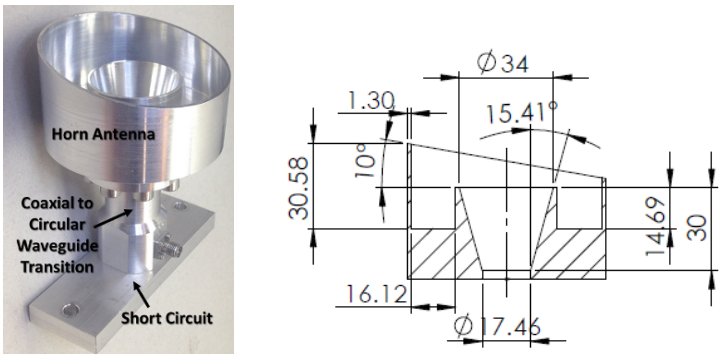

(a) (b)

Figure C.1: The proposed tapered coaxial cavity horn antenna design layout and details. (a) Fabricated model. (b) A section view to the design details along the cavity tapering with all dimensions in millimeter.

with either the E-plane or H-plane of the antenna. The measured and simulated reflection coefficients are presented in Fig. C.2 for the horn tapering aligned with the H-plane. It is worth mentioning that the reflection coefficient in this design is mainly dominated by the effect of the transition described in Appendix C.3, thus different orientations have minimal effects on the return loss. The resultant radiation patterns for both orientations are shown in Fig. C.3. The radiation patterns show that aligning the tapering with the H-plane gives better tapering with a more flat response in the E-plane. Consequently, this configuration gives a more compliant pattern with the characteristics specified in Eqs. (6.2) and (6.3). Also, H-plane tapering results in a lower side lobe level as shown in the difference between Fig. C.3 (a) and Fig. C.3 (b). Moreover, the preferred H-plane tapering design also features a stable radiation pattern across the operating frequency band as presented in Fig. C.4 with the measured results.

In terms of aperture efficiency prediction, antenna feed phase center position sweep is performed along the plane vz to observe the best obtained aperture efficiency at every point as shown in Fig. C.5 (a). A local optimization procedure is performed to obtain the best θ_r, which is the angle of rotation from the broadside antenna z_f

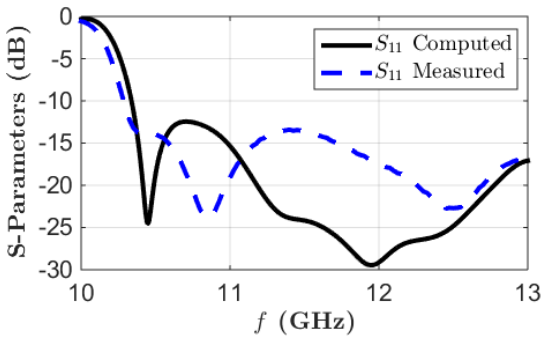

Figure C.2: A comparison between the measured and computed reflection coefficients of the proposed design in Fig. C.1 (H-plane tapering).

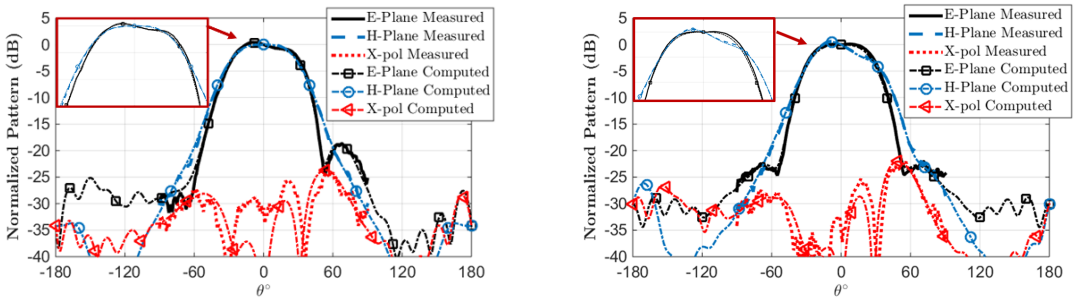

(a) (b)

Figure C.3: A comparison between the measured and simulated radiation patterns of the proposed design in Fig. C.1 at $f_0 = 11.7$ GHz. (a) Cavity tapering along the antenna E-plane. (b) Cavity tapering along the antenna H-plane.

to achieve the best aperture efficiency from a given position. The aperture efficiency results for the proposed antenna solution for both tapering alignments are presented in Figs. C.5 (c) and C.5 (d) for the E-plane and H-plane horn tapering situations. This efficiency results can be compared to the results of the conical horn antenna in Fig. C.5 (b). The presented aperture efficiency results show that the E-tapering situation is shown in Fig. C.5 (c), where the vz plane is aligned with the reflectarray's yz plane. The results show that this design is more suitable as a center feed due to the slight radiation pattern tapering as presented in Fig. C.3 (a). Also, the H-tapering situation gives high aperture efficiency values at offset feeding situations as shown in Fig. C.5 (d) at the left side, where the vz plane is aligned with the xz plane. Generally, this design provides the tapered beam peak at the peak edge of the horn.

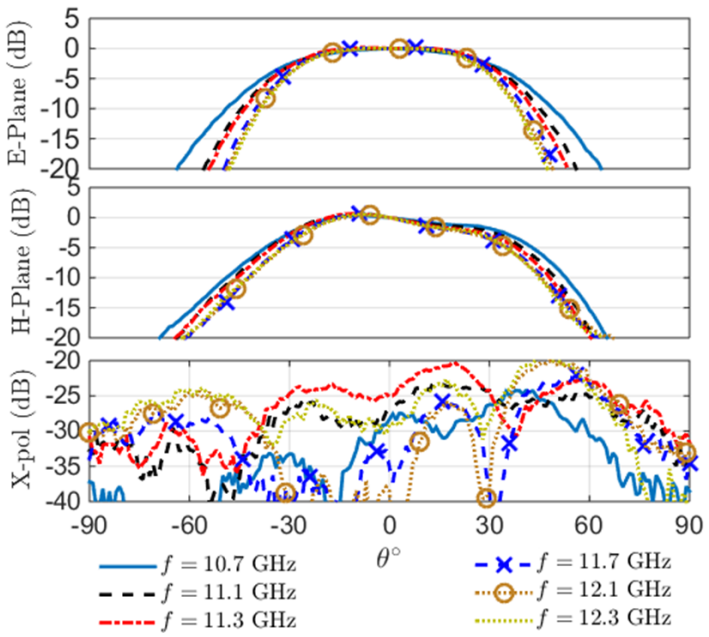

Figure C.4: A comparison between the measured radiation patterns of the proposed design in Fig. C.1 with tapering along the H-plane at different frequency points within the operating frequencies.

The presented results provide evidence of the potential of using the proposed approach to design efficient reflectarray antennas in more compact configurations than other efficient reflectarrays presented in the literature with directive feeds (i.e., require placement further from the reflectarray).

C.2 Another Possible Solution

The other alternative solution is to taper the horn flare while the coaxial cavity remains unchanged as presented in Fig. C.6. The tapering scheme followed the same concept as the previous case of maintaining the non-tapered plane dimensions unchanged. The simulated reflection coefficients for both tapering situations (i.e., aligned with E-plane or H-plane) are shown in Fig. C.7. Also, the simulated radiation patterns are shown in Fig. C.8. The aperture efficiency simulation for different positions over the vz plane are shown in Fig. C.9. The aperture efficiency show

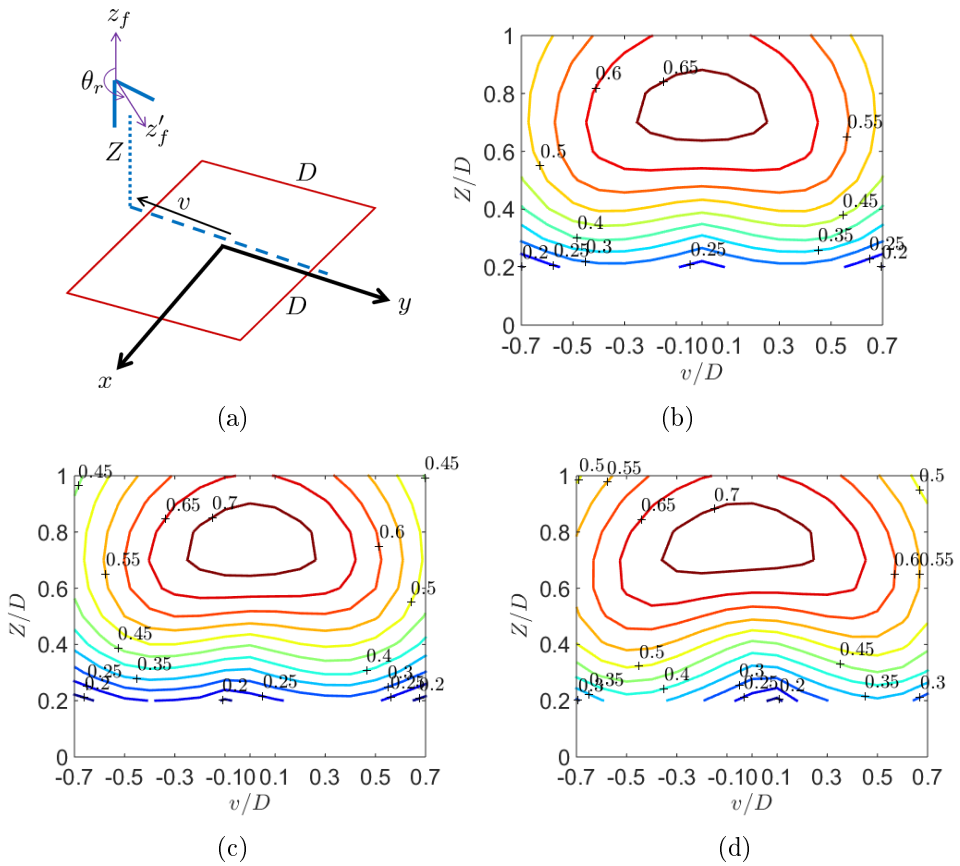

Figure C.5: The best computed aperture efficiency for different antenna feeds. (a) Illustration for the sweep plane. (b) Conical horn feed. (c) Tapered cavity horn antenna (E-plane tapering). (d) Tapered cavity horn antenna (H-plane tapering).

that both tapering orientations give better results for the offset feeding scenarios. However, the simulated pattern for the H-plane tapering is more compliant with the specified characteristics in Eqs. (6.2) and (6.3) with a tapering in one plane and a dip in the broadside direction of the other plane. However, this design is not fabricated as it cannot be manufactured accurately with the manual machining facility available to us.

In all the presented tapered designs, increasing the tapering angle α_t increases the tapering in the radiation pattern. However, this has an implication on the cross polarization and side lobe level. Our experience with these designs showed a maximum of $\alpha_t = 20°$ tapering is allowed for acceptable radiation patterns. However, tapered

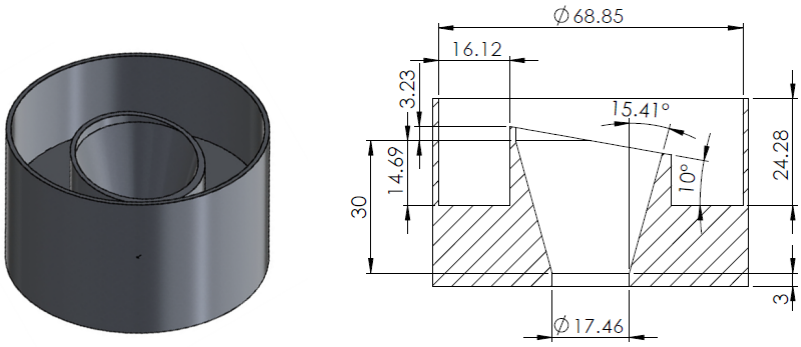

(a) (b)

Figure C.6: The proposed tapered horn antenna with coaxial cavity design layout and details. (a) Prospective view. (b) A cross section view to the design details along the horn tapering with all dimensions in millimeter.

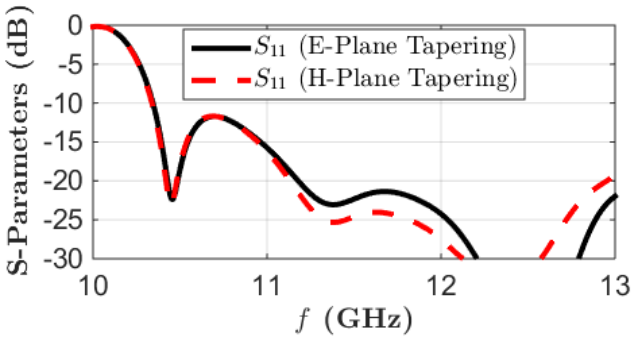

Figure C.7: The computed reflection coefficients of the proposed design in Fig. C.6 for both tapering orientations.

antennas with tapering angles larger than 10° are more difficult to be fabricated manually as we did with the previously presented designs.

C.3 Coaxial to Circular Waveguide Transition Design

A custom design for the coaxial to circular waveguide transition is employed for the proposed designs. Since the operating band falls between the X and Ku bands (i.e., 10.7 - 12.7 GHz), non-standard circular waveguide dimensions are exploited to have a single mode propagation within the operating frequency band as well as ease of

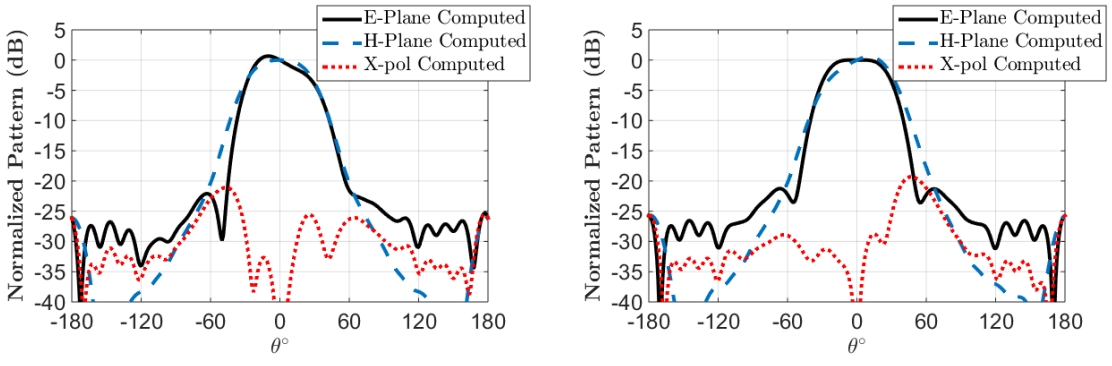

Figure C.8: The simulated radiation patters for the tapered horn design in Fig. C.6. (a) Tapered cavity horn antenna (E-plane tapering). (b) Tapered cavity horn antenna (H-plane tapering).

fabrication. The circular waveguide diameter is chosen to be 17.46 mm to be exactly the same as an available standard drill bit. Consequently, the dominant TE_{11} mode has a cutoff frequency 10.069 GHz and the next mode TM_{01} has a cutoff frequency 13.151 GHz. In addition, a long probe coaxial connector is chosen to maintain better accuracy in assembling the transition. A design goal was set to use the provided connector without trimming. Through numerical optimization by CST, the final design dimensions are shown in Fig. C.10. The optimization goal was to maintain minimal reflection coefficient (less than -15 dB) in a double symmetric transitions configuration (i.e., coaxial to circular waveguide to coaxial again) to be able to compare with measurements as shown in Fig. C.11. The simulation and measured results for the designed transition are presented in Fig. C.12. The presented results show an acceptable performance with minor changes due to machining tolerance and vibrations. Also, the worst measured insertion loss within the operating frequency band was 0.3 dB including the losses in the connectors.

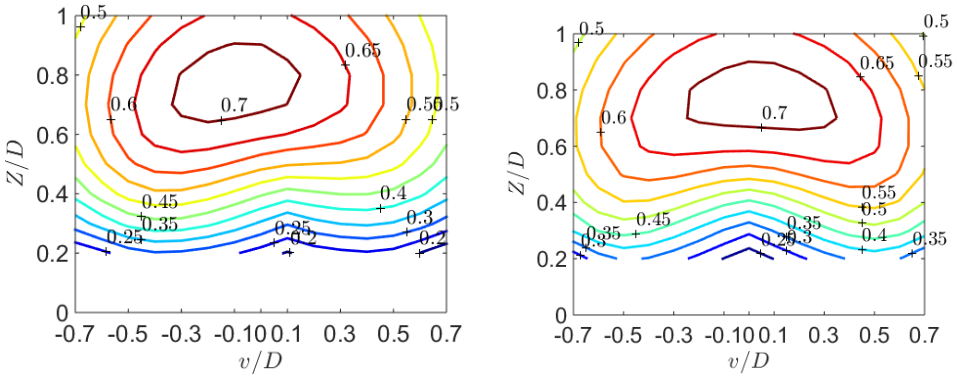

(a) (b)

Figure C.9: The best computed aperture efficiency for different antenna feeds using the layout showed in Fig. C.5 (a). (a) Tapered cavity horn antenna (E-plane tapering). (b) Tapered cavity horn antenna (H-plane tapering).

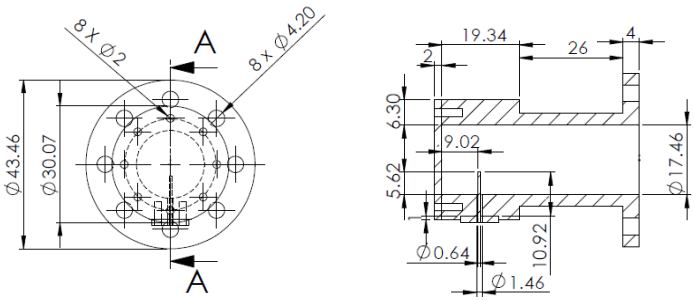

(a) (b)

Figure C.10: The designed coaxial to circular waveguide transition. (a) Front view. (b) Cross section A-A view. All the presented dimensions are in millimeters.

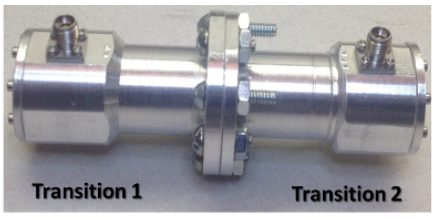

Figure C.11: The double transition measurement setup.

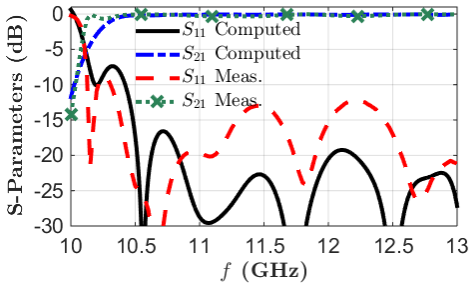

Figure C.12: The double transition computed and measured S-Parameters.

Appendix D

Reflection Analysis of Arbitrary Anisotropic Surface Impedance

The impedance boundary condition defined in [56, 168] sets relations between transverse components of electromagnetic waves interacting with it as

$$\mathbf{E} - (\mathbf{E} \cdot \hat{\mathbf{z}})\,\hat{\mathbf{z}} = \overleftrightarrow{Z_s} \cdot (\hat{\mathbf{z}} \times \mathbf{H})\,, \tag{D.1}$$

where $\mathbf{E}$ and $\mathbf{H}$ are the total electric and magnetic fields, respectively, $\hat{\mathbf{z}}$ is a unit vector normal to surface impedance boundary and $\overleftrightarrow{Z_s}$ is the anisotropic surface impedance tensor.

The measured anisotropic surface impedance values in Sec. 3.3 are defined with respect to the global coordinate system of the solar cells, which is aligned with the reflectarray coordinate system. Thus, the rotation has to be preformed to have the surface impedance aligned with the plane of incidence to use plane wave incidence and reflection analysis for the homogenized dielectric unit cell as illustrated in Fig. D.1. The resultant solar cells anisotropic surface impedance in the primed coordinates can

be expressed as

$$Z_s' = \begin{bmatrix} Z_{y'y'} & Z_{y'x'} \\ Z_{x'y'} & Z_{x'x'} \end{bmatrix} = \begin{bmatrix} Z_{yy}\cos^2\varphi_e + Z_{xx}\sin^2\varphi_e & \cos\varphi_e \sin\varphi_e \left(Z_{xx} - Z_{yy}\right) \\ \cos\varphi_e \sin\varphi_e \left(Z_{xx} - Z_{yy}\right) & Z_{xx}\cos^2\varphi_e + Z_{yy}\sin^2\varphi_e \end{bmatrix}, \tag{D.2}$$

where φ_e is the unit cell's position azimuthal angle in cylindrical coordinates as illustrated in Fig. D.1. It is noted that the off diagonal surface impedance values are equal. Consequently, in the plane of incidence $v - z$, the incident and reflected TE and TM electric field vectors can be defined as

$$\begin{aligned} \mathbf{E}_i^{TM}(\mathbf{r}) &= E_0^{TM}\left(\hat{\mathbf{x}}'\cos\theta_e + \hat{\mathbf{z}}'\sin\theta_e\right) e^{-j\mathbf{k}_i\cdot\mathbf{r}}, \\ \mathbf{E}_i^{TE}(\mathbf{r}) &= E_0^{TE}\hat{\mathbf{y}}' e^{-j\mathbf{k}_i\cdot\mathbf{r}}, \\ \mathbf{E}_r^{TM}(\mathbf{r}) &= E_r^{TM}\left(\hat{\mathbf{x}}'\cos\theta_e - \hat{\mathbf{z}}'\sin\theta_e\right) e^{-j\mathbf{k}_r\cdot\mathbf{r}}, \\ \mathbf{E}_r^{TE}(\mathbf{r}) &= E_r^{TE}\hat{\mathbf{y}}' e^{-j\mathbf{k}_r\cdot\mathbf{r}}, \end{aligned} \tag{D.3}$$

where θ_e is the elevation angle of incidence of the uniform plane wave over the unit cell, $\mathbf{r}$ is an arbitrary point in space in the primed coordinates and the propagation vectors $\mathbf{k}_i$ and $\mathbf{k}_r$ are defined as

$$\begin{aligned} \mathbf{k}_i &= \hat{\mathbf{x}}'\sin\theta_e - \hat{\mathbf{z}}'\cos\theta_e, \\ \mathbf{k}_r &= \hat{\mathbf{x}}'\sin\theta_e + \hat{\mathbf{z}}'\cos\theta_e. \end{aligned} \tag{D.4}$$

Using plane waves relations defined in [111] with the anisotropic boundary condition defined in Eq. (D.1), the reflection coefficients can be evaluated through linear systems of equations for the transverse magnetic (TM) and electric (TE) incidence

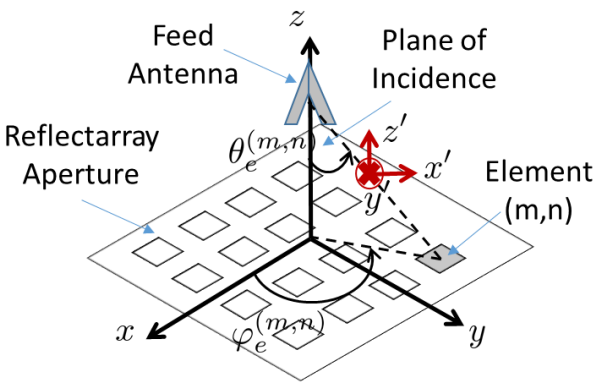

Figure D.1: An illustration for the plane of incidence associated with the reflectarray unit cell (m,n).

cases as

$$\begin{bmatrix} -\frac{Z_{x'y'}}{\eta_0}\cos\theta_e & -\frac{Z_{x'x'}}{\eta_0}-\cos\theta_e \\ -\frac{Z_{y'y'}}{\eta_0}\cos\theta_e-1 & -\frac{Z_{x'y'}}{\eta_0} \end{bmatrix} \begin{bmatrix} \Gamma_{TM}^{TE} \\ \Gamma_{TM}^{TM} \end{bmatrix} = \begin{bmatrix} \cos\theta_e-\frac{Z_{x'x'}}{\eta_0} \\ -\frac{Z_{x'y'}}{\eta_0} \end{bmatrix} \tag{D.5}$$

and

$$\begin{bmatrix} -\frac{Z_{y'y'}}{\eta_0}\cos\theta_e-1 & -\frac{Z_{x'y'}}{\eta_0} \\ -\frac{Z_{x'y'}}{\eta_0}\cos\theta_e & -\frac{Z_{x'x'}}{\eta_0}-\cos\theta_e \end{bmatrix} \begin{bmatrix} \Gamma_{TE}^{TE} \\ \Gamma_{TE}^{TM} \end{bmatrix} = \begin{bmatrix} 1-\frac{Z_{y'y'}}{\eta_0}\cos\theta_e \\ -\frac{Z_{x'y'}}{\eta_0}\cos\theta_e \end{bmatrix}, \tag{D.6}$$

where $\Gamma_{TM}^{TM}=E_r^{TM}/E_0^{TM}$, $\Gamma_{TM}^{TE}=E_r^{TE}/E_0^{TM}$, $\Gamma_{TE}^{TM}=E_r^{TM}/E_0^{TE}$ and $\Gamma_{TE}^{TE}=E_r^{TE}/E_0^{TE}$ are the reflection coefficients for all possible incidence and reflection situations.

Bibliography

[1] E. H. Lim and K.-W. Leung, "Use of the dielectric resonator antenna as a filter element," *Antennas and Propagation, IEEE Transactions on*, vol. 56, no. 1, pp. 5–10, 2008.

[2] L. Hady, D. Kajfez, and A. Kishk, "Dielectric resonator antenna in a polarization filtering cavity for dual function applications," *Microwave Theory and Techniques, IEEE Transactions on*, vol. 56, no. 12, pp. 3079–3085, Dec 2008.

[3] L. Covert and J. Lin, "Simulation and measurement of a heatsink antenna: a dual-function structure," *Antennas and Propagation, IEEE Transactions on*, vol. 54, no. 4, pp. 1342–1349, April 2006.

[4] Y.-P. Zhang, X. Li, and T. Y. Phang, "A study of dual-mode bandpass filter integrated in bga package for single-chip rf transceivers," *Advanced Packaging, IEEE Transactions on*, vol. 29, no. 2, pp. 354–358, 2006.

[5] E. H. Lim and K.-W. Leung, "Transparent dielectric resonator antennas for optical applications," *Antennas and Propagation, IEEE Transactions on*, vol. 58, no. 4, pp. 1054–1059, 2010.

[6] K. Leung, Y. Pan, X. Fang, E. Lim, K.-M. Luk, and H. Chan, "Dual-function radiating glass for antennas and light covers - part i: Omnidirectional glass dielectric resonator antennas," *Antennas and Propagation, IEEE Transactions on*, vol. 61, no. 2, pp. 578–586, Feb 2013.

[7] M. Tanaka, R. Suzuki, Y. Suzuki, and K. Araki, "Microstrip antenna with solar cells for microsatellites," in *Antennas and Propagation Society International Symposium, 1994. AP-S. Digest*, vol. 2, 1994, pp. 786–789 vol.2.

[8] J. Kuendig, M. Goetz, X. Niquille, A. Shah, S. Vaccaro, J. Mosig, L. Gerlach, P. De Maagt, and E. Fernandez, "Thin-film silicon solar cells for space applications: radiation hardness and applications for an integrated solant (solar cell-antenna) module," in *Photovoltaic Specialists Conference, 2000. Conference Record of the Twenty-Eighth IEEE*, 2000, pp. 1079–1082.

[9] N. Henze, M. Weitz, P. Hofmann, C. Bendel, J. Kirchhof, and H. Fruchting, "Investigation of planar antennas with photovoltaic solar cells for mobile communications," in *Personal, Indoor and Mobile Radio Communications, 2004. PIMRC 2004. 15th IEEE International Symposium on*, vol. 1, 2004, pp. 622–626 Vol.1.

[10] S. V. Shynu, M. Ons, P. McEvoy, M. Ammann, S. McCormack, and B. Norton, "Integration of microstrip patch antenna with polycrystalline silicon solar cell," *Antennas and Propagation, IEEE Transactions on*, vol. 57, no. 12, pp. 3969–3972, 2009.

[11] E. H. Lim, K. Leung, C. C. Su, and H. Y. Wong, "Green antenna for solar energy collection," *Antennas and Wireless Propagation Letters, IEEE*, vol. 9, pp. 689–692, 2010.

[12] O. Yurduseven, D. Smith, and N. Pearsall, "Solar cell stacked modified z-double l-slot quad-band pifa," in *7th European Conference on Antennas and Propagation (EuCAP)*, 2013.

[13] A. McEvoy, L. Castañer, and T. Markvart, *Solar Cells: Materials, Manufacture and Operation*, 2nd ed. Elsevier Ltd, 2013.

[14] M. A. Green, K. Emery, Y. Hishikawa, W. Warta, and E. D. Dunlop, "Solar cell efficiency tables (version 39)," *Progress in Photovoltaics: Research and Applications*, vol. 20, no. 1, pp. 12–20, 2012. [Online]. Available: http://dx.doi.org/10.1002/pip.2163

[15] NSERC. NSERC smart net-zero energy building strategic research network. [Online]. Available: http://www.solarbuildings.ca/index.php/en/

[16] S. R. Best, *Antenna Engineering Handbook*, 4th ed. McGraw Hill, 2007, ch. Small Antennas, pp. 6–4 – 6–16.

[17] M. Danesh and J. Long, "An autonomous wireless sensor node incorporating a solar cell antenna for energy harvesting," *Microwave Theory and Techniques, IEEE Transactions on*, vol. 59, no. 12, pp. 3546–3555, 2011.

[18] S. Hwu, B. P. Lu, L. Johnson, J. Fournet, R. Panneton, and G. Arndt, "Scattering properties of solar panels for antenna pattern analysis," in *Antennas and Propagation Society International Symposium, 1994. AP-S. Digest*, vol. 1, June 1994, pp. 266–269 vol.1.

[19] W. An, S. Xu, F. Yang, and J. Gao, "A ka-band reflectarray antenna integrated with solar cells," *Antennas and Propagation, IEEE Transactions on*, vol. PP, no. 99, pp. 1–1, 2014.

[20] J. Oh, K. Lee, T. Hughes, S. Forrest, and K. Sarabandi, "Flexible antenna integrated with an epitaxial lift-off solar cell array for flapping-wing robots," *Antennas and Propagation, IEEE Transactions on*, vol. 62, no. 8, pp. 4356–4361, Aug 2014.

[21] P. Dreyer, M. Morales-Masis, S. Nicolay, C. Ballif, and J. Perruisseau-Carrier, "Copper and transparent-conductor reflectarray elements on thin-film solar cell

panels," *Antennas and Propagation, IEEE Transactions on*, vol. 62, no. 7, pp. 3813–3818, July 2014.

[22] M. Danesh, J. Long, and M. Simeoni, "Small-area solar antenna for low-power uwb transceivers," in *Antennas and Propagation (EuCAP), 2010 Proceedings of the Fourth European Conference on*, 2010, pp. 1–4.

[23] D. M. Pozar, "Reflectanay antenna and solar anay integration for spacecraft applications," University of Massachusetts at Amherst, Final report prepared fbr JPL under Contract No. 960740, March 1997.

[24] W. Stutzman and G. Thiele, *Antenna Theory and Design*, ser. Antenna Theory and Design. Wiley, 2012.

[25] U. Elani, M. Al-Salhi, S. Kamh, and J. Al-Otaibi, "The conductivity modulation of silicon samples under dark and gamma irradiation conditions," *Solar Energy*, vol. 78, no. 1, pp. 23 – 29, 2005. [Online]. Available: http://www.sciencedirect.com/science/article/pii/S0038092X04001410

[26] M.-J. Roo Ons, S. Shynu, M. Ammann, S. McCormack, and B. Norton, "On surface currents in a polycrystalline solar cell acting as ground plane for microstrip patch antennas," in *Antennas and Propagation Society International Symposium, 2008. AP-S 2008. IEEE*, 2008, pp. 1–4.

[27] M. J. R. Ons, "Integration of antennas and solar cells for autonomous communication systems," Ph.D. dissertation, School of Electronic & Communications Engineering, Dublin Institute of Technology, September 2010.

[28] N. Henze, C. Bendel, H. Fruchting, and J. Kirchhof, "Application of photovoltaic solar cells in planar antenna structures," in *Antennas and Propagation, 2003. (ICAP 2003). Twelfth International Conference on (Conf. Publ. No. 491)*, vol. 2, March 2003, pp. 731–734 vol.2.

[29] O. Yurduseven, D. Smith, and M. Elsdon, "Cross-coax fed wideband solar patch antenna," in *Microwave Techniques (COMITE), 2013l Conference on*, 2013, pp. 25–30.

[30] O. Yurduseven, D. Smith, N. Pearsall, and I. Forbes, "Design of a highly efficient wideband suspended solar array antenna," in *Antennas and Propagation Society International Symposium (APSURSI), 2012 IEEE*, 2012, pp. 1–2.

[31] ——, "A triband short-circuited suspended solar patch antenna," in *Antennas, Propagation EM Theory (ISAPE), 2012 10th International Symposium on*, 2012, pp. 294–297.

[32] S. Vaccaro, C. Pereira, J. Mosig, and P. de Maagt, "In-flight experiment for combined planar antennas and solar cells (solant)," *Microwaves, Antennas Propagation, IET*, vol. 3, no. 8, pp. 1279–1287, 2009.

[33] O. Yurduseven and D. Smith, "A solar cell stacked multi-slot quad-band pifa for gsm, wlan and wimax networks," *Microwave and Wireless Components Letters, IEEE*, vol. 23, no. 6, pp. 285–287, 2013.

[34] S. Vaccaro, P. Torres, J. Mosig, A. Shah, J. F. Zurcher, A. Skrivervik, P. De Maagt, and L. Gerlach, "Stainless steel slot antenna with integrated solar cells," *Electronics Letters*, vol. 36, no. 25, pp. 2059–2060, 2000.

[35] S. Vaccaro, J. Mosig, and P. De Maagt, "Linearly and circularly polarized slot antennas integrating solar cells," in *Antennas and Propagation Society International Symposium, 2001. IEEE*, vol. 3, 2001, pp. 478–485 vol.3.

[36] T. Wu, R. Li, and M. Tentzeris, "A mechanically stable, low profile, omnidirectional solar-cell integrated antenna for outdoor wireless sensor nodes," in *Antennas and Propagation Society International Symposium, 2009. APSURSI '09. IEEE*, 2009, pp. 1–4.

[37] S. V. Shynu, M.-J. Roo Ons, M. Ammann, S. McCormack, and B. Norton, "Dual band a-si:h solar-slot antenna for 2.4/5.2ghz wlan applications," in *Antennas and Propagation, 2009. EuCAP 2009. 3rd European Conference on*, 2009, pp. 408–410.

[38] R. Caso, A. D'Alessandro, A. Michel, and P. Nepa, "Integration of slot antennas in commercial photovoltaic panels for stand-alone communication systems," *Antennas and Propagation, IEEE Transactions on*, vol. 61, no. 1, pp. 62–69, 2013.

[39] T. W. Turpin, "Meshed patch antennas integrated on solar cell - a feasibility study and optimization," Master's thesis, Utah State University, Logan, UT, USA, 2009. [Online]. Available: http://digitalcommons.usu.edu/etd/251/

[40] O. Yurduseven, D. Smith, N. Pearsall, I. Forbes, and D. Johnston, "A meshed multiband solar patch array antenna," in *Antennas and Propagation Conference (LAPC), 2012 Loughborough*, 2012, pp. 1–5.

[41] O. Yurduseven, D. Smith, N. Pearsall, and I. Forbes, "A transparent solar patch antenna for 2.4/2.5 ghz wlan-wimax applications," in *Environment Friendly Energies and Applications (EFEA), 2012 2nd International Symposium on*, 2012, pp. 614–617.

[42] T. Yasin and R. Baktur, "Circularly polarized meshed patch antenna for small satellite application," *Antennas and Wireless Propagation Letters, IEEE*, vol. 12, pp. 1057–1060, 2013.

[43] S. Sheikh, "Circularly polarized meshed patch antenna," *Antennas and Wireless Propagation Letters, IEEE*, vol. PP, no. 99, pp. 1–1, 2015.

[44] O. O'Conchubhair, P. McEvoy, and M. Ammann, "Integration of inverted-f antenna with solar cell substitute," in *Antennas and Propagation Conference (LAPC), 2012 Loughborough*, 2012, pp. 1–4.

[45] T. Peter, T. Rahman, S. Cheung, R. Nilavalan, H. Abutarboush, and A. Vilches, "A novel transparent uwb antenna for photovoltaic solar panel integration and rf energy harvesting," *Antennas and Propagation, IEEE Transactions on*, vol. 62, no. 4, pp. 1844–1853, April 2014.

[46] R. Mongia, A. Ittipiboon, and M. Cuhaci, "Measurement of radiation efficiency of dielectric resonator antennas," *Microwave and Guided Wave Letters, IEEE*, vol. 4, no. 3, pp. 80–82, March 1994.

[47] O. O'Conchubhair, P. McEvoy, and M. Ammann, "Integration of antenna array with multicrystalline silicon solar cell," *Antennas and Wireless Propagation Letters, IEEE*, vol. 14, pp. 1231–1234, 2015.

[48] C. A. Balanis, *Antenna Theory: Analysis and Design*, 3rd ed. Wiley, 2012.

[49] D. Berry, R. Malech, and W. Kennedy, "The reflectarray antenna," *Antennas and Propagation, IEEE Transactions on*, vol. 11, no. 6, pp. 645–651, Nov 1963.

[50] J. Montgomery, "Scattering by an infinite periodic array of microstrip elements," *Antennas and Propagation, IEEE Transactions on*, vol. 26, no. 6, pp. 850–854, Nov 1978.

[51] M. Zawadzki and J. Huang, "Integrated rf antenna and solar array for spacecraft application," in *Phased Array Systems and Technology, 2000. Proceedings. 2000 IEEE International Conference on*, 2000, pp. 239–242.

[52] W. An, S. Xu, and F. Yang, "Design of reflectarray element integrated with solar cells," in *Antennas and Propagation Society International Symposium (APSURSI), 2014 IEEE*, July 2014, pp. 801–802.

[53] P. Dreyer, J. Gomez Diaz, and J. Perruisseau-Carrier, "Design of a reflectarray element integrated in a solar cell panel," in *Antennas and Propagation Society International Symposium (APSURSI), 2013 IEEE*, July 2013, pp. 1558–1559.

[54] Z. Wu, Z. Chen, X. Du, J. M. Logan, J. Sippel, M. Nikolou, K. Kamaras, J. R. Reynolds, D. B. Tanner, A. F. Hebard, and A. G. Rinzler, "Transparent, conductive carbon nanotube films," *Science*, vol. 305, no. 5688, pp. 1273–1276, 2004. [Online]. Available: http://www.sciencemag.org/content/305/5688/1273.abstract

[55] H. Mercier and J.-J. Laurin, "A free-space reflectometer for surface impedance measurement of materials in the ku-band," in *Electromagnetic Compatibility, 1995. Symposium Record., 1995 IEEE International Symposium on*, 1995, pp. 62–67.

[56] A. A. K. Kishk and P.-S. Kildal, "Electromagnetic scattering from two dimensional anisotropic impedance objects under oblique plane wave incidence," *Applied Computational Electromagnetics Society Journal*, vol. 10, no. 3, pp. 81–92, 1995.

[57] D. Sievenpiper, L. Zhang, R. F. J. Broas, N. Alexopolous, and E. Yablonovitch, "High-impedance electromagnetic surfaces with a forbidden frequency band," *Microwave Theory and Techniques, IEEE Transactions on*, vol. 47, no. 11, pp. 2059–2074, 1999.

[58] F. Yang and Y. Rahmat-Samii, *Electromagnetic Band Gap Structures in Antenna Engineering.* Cambridge Univeristy Press, 2009, ch. 4, pp. 87–124.

[59] E. Newman, P. Bohley, and C. H. Walter, "Two methods for the measurement of antenna efficiency," *Antennas and Propagation, IEEE Transactions on*, vol. 23, no. 4, pp. 457–461, 1975.

[60] D. M. Pozar and B. Kaufman, "Comparison of three methods for the measurement of printed antenna efficiency," *Antennas and Propagation, IEEE Transactions on*, vol. 36, no. 1, pp. 136–139, 1988.

[61] J. Ashkenazy, E. Levine, and D. Treves, "Radiometric measurement of antenna efficiency," *Electronics Letters*, vol. 21, no. 3, pp. 111–112, 1985.

[62] K. Rosengren, P.-S. Kildal, C. Carlsson, and J. Carlsson, "Characterization of antennas for mobile and wireless terminals in reverberation chambers: Improved accuracy by platform stirring," *Microwave and Optical Technology Letters*, vol. 30, no. 6, pp. 391–397, 2001. [Online]. Available: http://dx.doi.org/10.1002/mop.1324

[63] H. Wheeler, "The radiansphere around a small antenna," *Proceedings of the IRE*, vol. 47, no. 8, pp. 1325–1331, 1959.

[64] T. Maeda, Y. Tsukumo, S. Yasuda, S. Sekine, and S. Obayashi, "Method and apparatus for measuring antenna radiation efficiency," United States of America Patent 5 300 939, April 5, 1994.

[65] H. Kitada, "Radiation efficiency measuring apparatus and radiation efficiency measuring method," United States of America Grant US8 400 366 B2, March 19, 2013.

[66] N. McEwan, R. Abd-Alhameed, and M. Abidin, "A modified radiometric method for measuring antenna radiation efficiency," *Antennas and Propagation, IEEE Transactions on*, vol. 51, no. 8, pp. 2099–2105, 2003.

[67] A. Wolfgang, W. Carlsson, C. Orlenius, and P. S. Kildal, "Improved procedure for measuring efficiency of small antennas in reverberation chambers," in *Antennas and Propagation Society International Symposium, 2003. IEEE*, vol. 4, 2003, pp. 727–730 vol.4.

[68] A. A. H. Azremi, H. Shiraz, and P. Hall, "Small antenna efficiency by the reverberation chamber and the wheeler cap methods," in *Networks, 2005. Jointly held with the 2005 IEEE 7th Malaysia International Conference on Communication., 2005 13th IEEE International Conference on*, vol. 1, 2005, pp. 12–16.

[69] C. Cho, I. Park, and H. Choo, "A modified wheeler cap method for efficiency measurements of probe-fed patch antennas with multiple resonances," *Antennas and Propagation, IEEE Transactions on*, vol. 58, no. 9, pp. 3074–3078, 2010.

[70] C. Cho, H. Choo, N.-W. Kang, and J.-S. Kang, "Advanced wheeler cap method for measuring the antenna efficiency," in *Antennas and Propagation (ISAP), 2012 International Symposium on*, 2012, pp. 995–998.

[71] C. Kakoyiannis, T. Zervos, G. Fikioris, and M. Pissas, "Efficiency measurements of multiband and circularly polarized magneto-dielectric antennas by the equivalent-circuit wheeler cap," in *Antennas and Propagation (EuCAP), 2014 8th European Conference on*, April 2014, pp. 372–376.

[72] R. Johnston and J. McRory, "An improved small antenna radiation-efficiency measurement method," *Antennas and Propagation Magazine, IEEE*, vol. 40, no. 5, pp. 40–48, 1998.

[73] M. Geissler, O. Litschke, D. Heberling, P. Waldow, and I. Wolff, "An improved method for measuring the radiation efficiency of mobile devices," in *Antennas and Propagation Society International Symposium, 2003. IEEE*, vol. 4, June 2003, pp. 743–746 vol.4.

[74] C. Mendes and C. Peixeiro, "Theoretical and experimental validation of a generalized wheeler cap method," in *Antennas and Propagation, 2007. EuCAP 2007. The Second European Conference on*, 2007, pp. 1–6.

[75] C. G. Kakoyiannis, "Post-processing accuracy enhancement of the improved wheeler cap for wideband antenna efficiency measurements," in *Antennas and Propagation (EuCAP), 2014 8th European Conference on*, April 2014.

[76] H. Schantz, "Radiation efficiency of uwb antennas," in *Ultra Wideband Systems and Technologies, 2002. Digest of Papers. 2002 IEEE Conference on*, May 2002, pp. 351–355.

[77] P. Miskovsky, J. Gonzalez-Arbesu, and J. Romeu, "Antenna radiation efficiency measurement in an ultrawide frequency range," *Antennas and Wireless Propagation Letters, IEEE*, vol. 8, pp. 72–75, 2009.

[78] M.-C. Huynh, "Wideband compact antennas for wireless communication applications," Ph.D. dissertation, Virginia Polytechnic Institute and State University, 2004.

[79] D. Nyberg, P.-S. Kildal, and J. Carlsson, "Radiation q and radiation efficiency of wideband small antennas and their relation to bandwidth and cut-off of spherical modes," in *Antennas and Propagation, 2007. EuCAP 2007. The Second European Conference on*, 2007, pp. 1–6.

[80] M.-R. Nezhad-Ahmadi, M. Fakharzadeh, B. Biglarbegian, and S. Safavi-Naeini, "High-efficiency on-chip dielectric resonator antenna for mm-wave transceivers," *Antennas and Propagation, IEEE Transactions on*, vol. 58, no. 10, pp. 3388–3392, Oct 2010.

[81] A. Yaghjian and S. Best, "Impedance, bandwidth, and q of antennas," *Antennas and Propagation, IEEE Transactions on*, vol. 53, no. 4, pp. 1298–1324, April 2005.

[82] C. Kakoyiannis, "Hybrid antenna efficiency measurements in fixed-geometry wheeler caps by wideband q-factor estimation," in *Antennas and Propagation Conference (LAPC), 2013 Loughborough*, Nov 2013, pp. 524–529.

[83] M. Moharram and A. Kishk, "Modified wheeler cap method for measurement of antenna efficiency," in *General Assembly and Scientific Symposium (URSI GASS), 2014 XXXIth URSI*, Aug 2014, pp. 1–4.

[84] D. Kajfez and A. Elsherbeni, "Determination of antenna q from the reflection-coefficient data [antenna designer's notebook]," *Antennas and Propagation Magazine, IEEE*, vol. 55, no. 4, pp. 154–162, 2013.

[85] K. S. Miller, "Complex linear least squares," *SIAM Review*, vol. 15, no. 4, pp. pp. 706–726, 1973. [Online]. Available: http://www.jstor.org/stable/2028727

[86] J. Kajfez, D. and W. Wheless, "Invariant definitions of the unloaded q factor (short paper)," *Microwave Theory and Techniques, IEEE Transactions on*, vol. 34, no. 7, pp. 840–841, 1986.

[87] D. Kajfez, "Correction for measured resonant frequency of unloaded cavity," *Electronics Letters*, vol. 20, no. 2, pp. 81–82, January 1984.

[88] C. Balanis, *Advanced Engineering Electromagnetics*, ser. CourseSmart Series. Wiley, 2012.

[89] S. Palreddy, A. Zaghloul, and Y. Lee, "An octave bandwidth electromagnetic band gap (ebg) structure," in *Antennas and Propagation (EUCAP), 2012 6th European Conference on*, 2012, pp. 3102–3105.

[90] L. Liang, C. H. Liang, L. Chen, and X. Chen, "A novel broadband ebg using cascaded mushroom-like structure," *Microwave and Optical Technology Letters*, vol. 50, no. 8, pp. 2167–2170, 2008. [Online]. Available: http://dx.doi.org/10.1002/mop.23598

[91] D. Pozar, *Microwave Engineering*. Wiley, 2004.

[92] H. Schantz, "Measurement of uwb antenna efficiency," in *Vehicular Technology Conference, 2001. VTC 2001 Spring. IEEE VTS 53rd*, vol. 2, 2001, pp. 1189–1191 vol.2.

[93] K. Ryu and A. Kishk, "Ultrawideband dielectric resonator antenna with broadside patterns mounted on a vertical ground plane edge," *Antennas and Propagation, IEEE Transactions on*, vol. 58, no. 4, pp. 1047–1053, April 2010.

[94] S. Duffy and M. Gouker, "Experimental comparison of the radiation efficiency for conventional and cavity backed microstrip antennas," in *Antennas and Propagation Society International Symposium, 1996. AP-S. Digest*, vol. 1, July 1996, pp. 196–199 vol.1.

[95] H.-J. Seo and A. Kishk, "Wideband linear and dual-polarized antenna based on huygens' source principle," in *General Assembly and Scientific Symposium, 2011 XXXth URSI*, Aug 2011, pp. 1–4.

[96] V. Davids and R. Lehmensiek, "The effects of a triple-junction solar cell on a dielectric resonator antenna," in *Antennas and Propagation (EuCAP), 2014 8th European Conference on*, April 2014, pp. 2928–2931.

[97] C. Hafner, "Beiträge zur Berechnung elektromagnetischer Wellen in zylindrische Strukturen mit Hilfe des 'point-matching'," Ph.D. dissertation, ETH Zurich, 1980.

[98] ——, "On the relationship between the mom and the gmt [em theory]," *Antennas and Propagation Magazine, IEEE*, vol. 32, no. 6, pp. 12 –19, dec. 1990.

[99] A. Ludwig, "A new technique for numerical electromagnetics," *Antennas and Propagation Society Newsletter, IEEE*, vol. 31, no. 1, pp. 40 –41, february 1989.

[100] A. K. Bandyopadhyay, C. Tomassoni, M. Mongiardo, and A. S. Omar, "Generalized multipole technique without redundant multipoles," *International Journal of Numerical Modelling: Electronic Networks, Devices and Fields*, vol. 18, no. 6, pp. 413–427, 2005.

[101] Y. Leviatan and A. Boag, "Analysis of te scattering from dielectric cylinders using a multifilament magnetic current model," *Antennas and Propagation, IEEE Transactions on*, vol. 36, no. 7, pp. 1026 –1031, jul 1988.

[102] D. Kaklamani and H. Anastassiu, "Aspects of the method of auxiliary sources (mas) in computational electromagnetics," *Antennas and Propagation Magazine, IEEE*, vol. 44, no. 3, pp. 48 – 64, jun 2002.

[103] H. Anastassiu, D. Lymperopoulos, and D. Kaklamani, "Accuracy analysis and optimization of the method of auxiliary sources (mas) for scattering by a circular cylinder," *Antennas and Propagation, IEEE Transactions on*, vol. 52, no. 6, pp. 1541 – 1547, june 2004.

[104] I. Heretakis, P. Papakanellos, and C. Capsalis, "A stochastically optimized adaptive procedure for the location of mas auxiliary monopoles: the case of electromagnetic scattering by dielectric cylinders," *Antennas and Propagation, IEEE Transactions on*, vol. 53, no. 3, pp. 938 – 947, march 2005.

[105] T. S. Sijher and A. A. Kishk, "Antenna modeling by infinitesimal dipoles using genetic algorithms," *Progress In Electromagnetics Research*, vol. 52, pp. 225–254, 2005.

[106] X. H. Wu, A. A. Kishk, and A. Glisson, "Antenna modeling by frequncy dependent hertzian dipoles using particle swarm optimization," in *Antennas and Propagation Society International Symposium 2006, IEEE*, july 2006, pp. 3527 – 3530.

[107] S. Mikki and A. A. Kishk, "Theory and applications of infinitesimal dipole models for computational electromagnetics," *Antennas and Propagation, IEEE Transactions on*, vol. 55, no. 5, pp. 1325 –1337, may 2007.

[108] CST STUDIO SUITEâĎć, "CST AG, Germany." [Online]. Available: www.cst.com.

[109] P.-S. Kildal, S. Skyttemyr, and A. Kishk, "G/t maximization of a paraboloidal reflector fed by a dipole-disk antenna with ring by using the multiple-reflection approach and the moment method," *Antennas and Propagation, IEEE Transactions on*, vol. 45, no. 7, pp. 1130–1139, Jul 1997.

[110] O. Iupikov, R. Maaskant, M. Ivashina, A. Young, and P.-S. Kildal, "Fast and accurate analysis of reflector antennas with phased array feeds including multiple reflections between feed and reflector," *Antennas and Propagation, IEEE Transactions on*, vol. 62, no. 7, pp. 3450–3462, July 2014.

[111] C. A. Balanis, *Advanced Engineering Electromagnetics*. Wiley, 1989.

[112] M. Moharram and A. Kishk, "Efficient electromagnetic scattering computation using the random auxiliary sources method for multiple composite 3d arbitrary objects," *Antennas and Propagation, IEEE Transactions on*, vol. 63, no. 8, pp. 1–1, 2015.

[113] M. A. Moharram and A. A. Kishk, "Electromagnetic scattering from 2d conducting objects using equivalent randomly distributed sources," in *The Applied Computational Electromagnetic Society Conference*, March 2013.

[114] ——, "Electromagnetic scattering from 2d dielectric objects using randomly distributed sources," in *Antennas and Propagation (EuCAP), 2013 7th European Conference on*, 2013, pp. 1546–1549.

[115] M. Moharram and A. Kishk, "Electromagnetic scattering from two-dimensional arbitrary objects using random auxiliary sources," *Antennas and Propagation Magazine, IEEE*, vol. 57, no. 1, pp. 204–216, Feb 2015.

[116] M. A. Moharram and A. A. Kishk, "Electromagnetic Domain Decomposition for 2D Multi-Scatterer Problem Using Randomly Distributed Sources," in *International Symposium on Antennas and Propagation, APS, IEEE*, 2013.

[117] R. F. Harrington, *Field Comutations by Moments Method*, D. G. Dudley, Ed. IEEE Press, 1993.

[118] J. Robinson and Y. Rahmat-Samii, "Particle swarm optimization in electromagnetics," *Antennas and Propagation, IEEE Transactions on*, vol. 52, no. 2, pp. 397–407, Feb 2004.

[119] H. Anastassiu, D. Kaklamani, D. Economou, and O. Breinbjerg, "Electromagnetic scattering analysis of coated conductors with edges using the method of auxiliary sources (mas) in conjunction with the standard impedance boundary condition (sibc)," *Antennas and Propagation, IEEE Transactions on*, vol. 50, no. 1, pp. 59–66, 2002.

[120] E. Kreyszig, *Advanced Engineering Mathematics*, 8th ed. New York: John Wiley & Sons Inc., 1999.

[121] W. H. Press, *Numerical Recipes : the art of scientific computing*, 3rd ed. Cambridge University Press, Sep 2007.

[122] A. Ludwig, "The definition of cross polarization," *Antennas and Propagation, IEEE Transactions on*, vol. 21, no. 1, pp. 116–119, Jan 1973.

[123] P. Kildal, *Foundations of Antennas: A Unified Approach.* Studentlitteratur, 2000.

[124] J. Huang and J. Encinar, *Reflectarray Antennas*, ser. IEEE Press Series on Electromagnetic Wave Theory. Wiley, 2007.

[125] A. Yu, F. Yang, A. Z. Elsherbeni, J. Huang, and Y. Rahmat-Samii, "Aperture efficiency analysis of reflectarray antennas," *Microwave and Optical Technology Letters*, vol. 52, no. 2, pp. 364–372, 2010.

[126] L. Fraas and L. Partain, *Solar Cells and Their Applications*, ser. Wiley Series in Microwave and Optical Engineering. Wiley, 2010.

[127] D. Pozar, "Bandwidth of reflectarrays," *Electronics Letters*, vol. 39, no. 21, pp. 1490–1491, Oct 2003.

[128] R. Munson, H. Haddad, and J. Hanlen, "Microstrip reflectarray for satellite communication and radar cross-section enhancement or reduction," Aug. 4 1987, uS Patent 4,684,952. [Online]. Available: http://www.google.ca/patents/US4684952

[129] J. Encinar, "Design of two-layer printed reflectarrays using patches of variable size," *Antennas and Propagation, IEEE Transactions on*, vol. 49, no. 10, pp. 1403–1410, Oct 2001.

[130] M. Chaharmir, J. Shaker, and H. Legay, "Broadband design of a single layer large reflectarray using multi cross loop elements," *Antennas and Propagation, IEEE Transactions on*, vol. 57, no. 10, pp. 3363–3366, Oct 2009.

[131] R. Florencio, R. R. Boix, E. Carrasco, J. A. Encinar, M. Barba, and G. Pérez-Palomino, "Broadband reflectarrays made of cells with three coplanar parallel dipoles," *Microwave and Optical Technology Letters*, vol. 56, no. 3, pp. 748–753, 2014. [Online]. Available: http://dx.doi.org/10.1002/mop.28171

[132] R. Florencio, J. Encinar, R. Boix, V. Losada, and G. Toso, "Reflectarray antennas for dual polarization and broadband telecom satellite applications," *Antennas and Propagation, IEEE Transactions on*, vol. 63, no. 4, pp. 1234–1246, April 2015.

[133] E. Carrasco, M. Barba, and J. Encinar, "Reflectarray element based on aperture-coupled patches with slots and lines of variable length," *Antennas and Propagation, IEEE Transactions on*, vol. 55, no. 3, pp. 820–825, March 2007.

[134] S. Zainud-Deen, Abd-Elhady, A. Mitkees, and A. Kishk, "Design of dielectric resonator reflectarray using full-wave analysis," in *Radio Science Conference, 2009. NRSC 2009. National*, March 2009, pp. 1–9.

[135] M. Abd-Elhady, W. Hong, and Y. Zhang, "A ka-band reflectarray implemented with a single-layer perforated dielectric substrate," *Antennas and Wireless Propagation Letters, IEEE*, vol. 11, pp. 600–603, 2012.

[136] P. Nayeri, M. Liang, R. Sabory-Garcia, M. Tuo, F. Yang, M. Gehm, H. Xin, and A. Elsherbeni, "3d printed dielectric reflectarrays: Low-cost high-gain antennas at sub-millimeter waves," *Antennas and Propagation, IEEE Transactions on*, vol. 62, no. 4, pp. 2000–2008, April 2014.

[137] M. Moeini-Fard and M. Khalaj-Amirhosseini, "Inhomogeneous perforated reflect-array antennas," *Wireless Engineering and Technology*, vol. 2, no. 2, pp. 80–86, 2011.

[138] M. Al-Nuaimi and W. Hong, "Discrete dielectric reflectarray and lens for e-band with different feed," *Antennas and Wireless Propagation Letters, IEEE*, vol. 13, pp. 947–950, 2014.

[139] D.-C. Chang and M.-C. Huang, "Multiple-polarization microstrip reflectarray antenna with high efficiency and low cross-polarization," *Antennas and Propagation, IEEE Transactions on*, vol. 43, no. 8, pp. 829–834, Aug 1995.

[140] C. Han, J. Huang, and K. Chang, "A high efficiency offset-fed x/ka-dual-band reflectarray using thin membranes," *Antennas and Propagation, IEEE Transactions on*, vol. 53, no. 9, pp. 2792–2798, Sept 2005.

[141] A. Vosoogh, K. Keyghobad, A. Khaleghi, and S. Mansouri, "A high-efficiency ku-band reflectarray antenna using single-layer multiresonance elements," *Antennas and Wireless Propagation Letters, IEEE*, vol. 13, pp. 891–894, 2014.

[142] P. Zhang and W. Zhang, "Design of an optimized feed for printed reflectarray antenna," in *Antenna Technology: Small Antennas and Novel Metamaterials, 2008. iWAT 2008. International Workshop on*, March 2008, pp. 259–262.

[143] G. F. Koch, "Coaxial feeds for high aperture efficiency and low spillover of paraboloidal reflector antennas," *IEEE Transactions on Antennas and Propagation*, vol. AP-21, no. 2, pp. 164–169, 1973.

[144] P. Clarricoats and G. Poulton, "High-efficiency microwave reflector antennas; a review," *Proceedings of the IEEE*, vol. 65, no. 10, pp. 1470–1504, Oct 1977.

[145] A. Kishk, "Simple primary focus feeds for deep reflectors," *Microwaves, Antennas and Propagation, IEE Proceedings H*, vol. 136, no. 2, pp. 169–171, Apr 1989.

[146] Z. Pour and L. Shafai, "A ring choke excited compact dual-mode circular waveguide feed for offset reflector antennas," *Antennas and Propagation, IEEE Transactions on*, vol. 60, no. 6, pp. 3011–3015, June 2012.

[147] M. A. Moharram and A. A. Kishk, "Design of optically transparent reflectarray antenna unit cell integrated with solar cells," in *Antennas and Propagation Society International Symposium (APSURSI), 2015 IEEE*, 2015 (accepted).

[148] Keysight. (Agilent), "85070e dielectric probe kit." [Online]. Available: http://www.keysight.com/en/pd-304506-pn-85070E/dielectric-probe-kit

[149] J. B. Muldavin and G. Rebeiz, "Millimeter-wave tapered-slot antennas on synthesized low permittivity substrates," *Antennas and Propagation, IEEE Transactions on*, vol. 47, no. 8, pp. 1276–1280, Aug 1999.

[150] M. A. Moharram and A. A. Kishk, "Optimum feeds for reflectarray antenna: Synthesis and design," *IEEE Transactions on Antennas and Propagation*, 2015 (submitted).

[151] P.-S. Kildal, A. Kishk, and A. Tengs, "Reduction of forward scattering from cylindrical objects using hard surfaces," *Antennas and Propagation, IEEE Transactions on*, vol. 44, no. 11, pp. 1509–1520, Nov 1996.

[152] "IEEE Standard Test Procedures for Antennas," *IEEE Std 149-1979*, April 2008.

[153] G. Smith, "Efficiency of electrically small antennas combined with matching networks," *Antennas and Propagation, IEEE Transactions on*, vol. 25, no. 3, pp. 369–373, May 1977.

[154] D. Kajfez, *Q Factor*. Vector Fields, Oxford, MS, 1994.

[155] N. Ishii, Y. Kobayashi, Y. Katagiri, and M. Miyakawa, "Systematic uncertainty of radiation efficiency based on some formulas for wheeler method," in *Antenna Technology: Small Antennas and Novel Metamaterials, 2008. iWAT 2008. International Workshop on*, March 2008, pp. 290–293.

[156] Y. Tsuboike, N. Ishii, and M. Miyakawa, "Uncertainty evaluation of wheeler and reflection methods for radiation efficiency using monte carlo simulation," in *The 2009 International Symposium on Antennas and Propagation (ISAP 2009)*, 2009.

[157] C. G. Kakoyiannis, "Fast broadband antenna efficiency measurements: The complementary q-factor method revisited," in *European Wireless 2014; 20th European Wireless Conference; Proceedings of*, May 2014, pp. 1–6.

[158] M. Moharram and A. Kishk, "Contactless wheeler cap concept for antenna radiation efficiency measurements," in *General Assembly and Scientific Symposium (URSI GASS), 2014 XXXIth URSI*, Aug 2014, pp. 1–4.

[159] ——, "Prediction of antennas radiation efficiency in resonance regions via contactless wheeler cap measurements," in *Antenna Measurements Applications (CAMA), 2014 IEEE Conference on*, Nov 2014, pp. 1–3.

[160] D. A. Hill, *Electromagnetic Fields in Cavities: Deterministic and Statistical Theories*. New York: Wiley-IEEE Press, 2009, ch. 2, pp. 28–30.

[161] Ansys Corporation. High Frequency Structure Simulator HFSS v.15. 2014. [Online]. Available: http://www.ansys.com/

[162] D. Kajfez, "Incremental frequency rule for computing the q-factor of a shielded teomp dielectic resonator (short papers)," *Microwave Theory and Techniques, IEEE Transactions on*, vol. 32, no. 8, pp. 941–943, 1984.

[163] J. Dunsmore, *Handbook of Microwave Component Measurements: With Advanced VNA Techniques*. Wiley, 2012. [Online]. Available: https://books.google.ca/books?id=GEnBhrvPFQwC

[164] N. Jin and Y. Rahmat-Samii, "Parallel particle swarm optimization and finite-difference time-domain (pso/fdtd) algorithm for multiband and wide-band patch antenna designs," *Antennas and Propagation, IEEE Transactions on*, vol. 53, no. 11, pp. 3459–3468, 2005.

[165] A. Erentok and R. Ziolkowski, "Metamaterial-inspired efficient electrically small antennas," *Antennas and Propagation, IEEE Transactions on*, vol. 56, no. 3, pp. 691–707, 2008.

[166] W. Huang and A. Kishk, "Compact wideband multi-layer cylindrical dielectric resonator antennas," *Microwaves, Antennas Propagation, IET*, vol. 1, no. 5, pp. 998–1005, 2007.

[167] W. Chew, *Fast and Efficient Algorithms in Computational Electromagnetics*, ser. Antennas and Propagation Library. Artech House, 2001.

[168] T. Senior, "Approximate boundary conditions," *Antennas and Propagation, IEEE Transactions on*, vol. 29, no. 5, pp. 826 – 829, sep 1981.

List of Publications

Journal Papers

Under Review

J-S-1 **Moharram, M.A.** and Kishk A. A., *" Optically Transparent Reflectarray Antenna Design Integrated with Solar Cells,"* IEEE Transactions on Antenna and Propagation, *(under review 2015).*

J-S-2 **Moharram, M.A.** and Kishk A. A., *" MIMO Antennas Efficiency Measurement Using Wheeler Caps,"* IEEE Transactions on Antenna and Propagation, *(under review 2015).*

J-S-3 **Moharram, M.A.** and Kishk A. A., *" Optimum Feeds for Reflectarray Antenna: Synthesis and Design,"* IEEE Transactions on Antenna and Propagation, *(under review 2015).*

Published

J-1 **Moharram, M.A.** and Kishk A. A., *"Efficient Electromagnetic Scattering Computation Using the Random Auxiliary Sources Method for Multiple Composite 3D Arbitrary Objects,"* IEEE Transactions on Antenna and Propagation, vol. 63, no. 8, pp.1,1, Aug. 2015, doi: 10.1109/TAP.2015.2438339.

J-2 **Moharram, M.A.** and Kishk A. A., *"Electromagnetic Scattering From 2D Arbitrary Objects Using Random Auxiliary Sources,"* Antennas and Propagation Magazine, IEEE , vol.57, no.1, pp.204-216, Feb. 2015

J-3 **Moharram, M.A.** and Kishk A. A. , *"General decoupling network design between two coupled antennas for MIMO applications,"* Progress In Electromagnetics Research Letters, Vol. 37, pp. 133-142, 2013.

Conference Papers

Accepted for Presentation

C-A-1 **Moharram, M.A.** and Kishk A. A., *"Design of Optically Transparent Reflectarray Antenna Unit Cell Integrated with Solar Cells,"* IEEE International Symposium on Antennas and Propagation Society (APSURSI), July 2015, (*Honorable Mention in the Student Paper Competition*), *(accepted).*

C-A-2 **Moharram, M.A.** and Kishk A. A., *"Optimum Reflectarray Feed Pattern Synthesis,"* IEEE International Symposium on Antennas and Propagation Society (APSURSI), July 2015, *(accepted).*

C-A-3 **Moharram, M.A.** and Kishk A. A., *"The Use of Random Auxiliary Sources for Reflectarray Feed Analysis,"* 2015 USNC-URSI Radio Science Meeting (Joint with AP-S Symposium), July 2015, *(accepted).*

Published

C-1 **Moharram, M.A.** and Kishk A. A., *" The random auxiliary sources method: A simple, fast, and efficient electromagnetic scattering computations approach."* Computational Electromagnetics (ICCEM), 2015 IEEE International Conference on , vol., no., pp.5,7, 2-5 Feb. 2015.

C-2 **Moharram, M.A.** and Kishk A. A., *"Prediction of Antennas Radiation Efficiency in Resonance Regions via Contactless Wheeler Cap Measurements,"* Antenna Measurements & Applications (CAMA), 2014 IEEE Conference on , vol., no., pp.1,3, 16-19 Nov. 2014.

C-3 **Moharram, M.A.** and Kishk A. A., *" Contactless wheeler cap concept for antenna radiation efficiency measurements,"* General Assembly and Scientific Symposium (URSI GASS), 2014 XXXIth URSI , vol., no., pp.1,4, 16-23 Aug. 2014.

C-4 **Moharram, M.A.** and Kishk A. A., *"Modified wheeler cap method for measurement of antenna efficiency,"* General Assembly and Scientific Symposium (URSI GASS), 2014 XXXIth URSI , vol., no., pp.1,4, 16-23 Aug. 2014.

C-5 **Moharram, M.A.** and Kishk A. A., "Efficient frequency domain technique for electromagnetic scattering from arbitrary objects using the Random Auxiliary Sources," in *2013 USNC-URSI Radio Science Meeting (Joint with AP-S Symposium)*, pp.143-143, 7-13 July 2013

C-6 **Moharram, M.A.** and Kishk A. A., "Electromagnetic domain decomposition for 2D multi-scatterer problem using randomly distributed sources," in *IEEE International Symposium on Antennas and Propagation Society (APSURSI)*, pp. 1310-1311, 7-13 July 2013.

C-7 **Moharram, M.A.** and Kishk A. A., "Electromagnetic scattering from 2D dielectric objects using randomly distributed sources," in *2013 7th European Conference on Antennas and Propagation (EuCAP)*, pp. 1546-1549, 8-12 April 2013

C-8 **Moharram, M.A.** and Kishk A. A., "Electromagnetic Scattering from 2D Conducting Objects Using Equivalent Randomly Distributed Sources," in *The*

Applied Computational Electromagnetic Society Conference, March 2013.

C-9 **Moharram, M.A.** and Kishk, A.A.; *"Decoupling Between Two Asymmetric Non-Perfectly Matched Antennas for MIMO Applications,"* IEEE International Symposium on Antennas and Propagation (APSURSI), pp.1-2, 8-14 July 2012.